UNIVERSITY OF SOUTHAMPTON

Faculty of Engineering and Physical Sciences
School of Electronics and Computer Science

Multi-parameter sensing platform for rumen monitoring

by

Zijin Fang

ORCiD: 0000-0001-8656-4920

A thesis for the degree of
Master of Philosophy

June 2023

University of Southampton

Abstract

Faculty of Engineering and Physical Sciences
School of Electronics and Computer Science

Master of Philosophy

Multi-parameter sensing platform for rumen monitoring

by Zijin Fang

Green-house gas (GHG) emissions from livestock contribute to environmental issues including global warming and climate change. There is a need to monitor parameters from animals, particularly ruminants to explore mitigation. These parameters include pH, oxidation-reduction potential (ORP) , dissolved oxygen (DO) and conductivity. Understanding these may help reduce the emission of GHGs and protect cows from diseases.

Electrochemical measurement techniques may provide solutions due to the low cost, small size, ease of integration and good accuracy. A stable reference electrode (RE) is required to provide a reference voltage and in this thesis, quasi-REs (QREs) were developed, which were also considered as Cl^- sensors. Ruthenium Oxide (RuO_x) pH sensors were made, showing good linearity and near-Nernstian response in phosphate-buffered saline (PBS) solution (-56.1mV/pH). Pt ring DO sensors were manufactured to measure dissolved oxygen concentration (DOC) with ±1.7% accuracy but with a limited detection range of 1-8mg/L. Conductivity sensors were developed exhibiting comparable performance (accuracies from ±0.5% to ±2.7%) to a commercial conductivity meter under laboratory test in the range 1.5-23mS/cm. ORP sensors were made from a Pt plate and showed good response with deviation <8mV from calibration solutions.

In vitro studies were carried out with three different rumen contents for the detection of Cl^-, pH, ORP, and conductivity using miniaturized sensor chips. The pH sensors demonstrated good matching with the commercial meter ($\Delta pH < 0.14$). ORP sensors took a few hours to stabilize and showed average ORP values of -0.099V, -0.123V and -0.07V in three rumen contents. QREs degraded rapidly in the rumen environment, giving an initial Cl^- concentration of 0.04-0.054M in rumen fluid. Excellent performance was observed for the conductivity sensor. In all three samples, low deviations were detected regardless of the chip configuration. In sample #1 and sample #3 the error was within 3.7% while in sample #2 larger errors were measured, as a result of the rapid temperature change and proximity effect due to active protozoa. The conductivity sensors were capable of delivering accurate measurements after a week, demonstrating minimal influence from the biofouling effect.

Future work involves the improvement of on-chip RE and DO sensors, optimization of in vitro measurement setup and the development and encapsulation of interface circuitry and sensor chips for in vivo detection.

Contents

List of Figures

List of Tables

Declaration of Authorship

I declare that this thesis and the work presented in it is my own and has been generated by me as the result of my own original research.

I confirm that:

1. This work was done wholly or mainly while in candidature for a research degree at this University;

2. Where any part of this thesis has previously been submitted for a degree or any other qualification at this University or any other institution, this has been clearly stated;

3. Where I have consulted the published work of others, this is always clearly attributed;

4. Where I have quoted from the work of others, the source is always given. With the exception of such quotations, this thesis is entirely my own work;

5. I have acknowledged all main sources of help;

6. Where the thesis is based on work done by myself jointly with others, I have made clear exactly what was done by others and what I have contributed myself;

7. None of this work has been published before submission

Signed:...   Date:.......................................

Acknowledgements

Definations and Abbreviations

Ag/AgCl	Silver/Silver chloride
Ag_2O	Silver oxide
Ag^+	Silver ion
AIROF	Anodic iridium oxide film
Au	Gold
BSA	Bovine serum albumin
C_{dl}	Double-layer capacitance
CA	Chronoamperometry
CE	Counter electrode
CeO_2	Cerium dioxide
CH_4	Methane
Cl^-	Chloride ion
CNT	Carbon nanotube
CO_2	Carbon dioxide
CP	Conducting polymers
Cr	Chromium
CV	Cyclic voltammetry
dCO_2	Dissolved carbon dioxide
DI	Deionized
DJRE	Double junction reference electrode
DOC	Dissolved oxygen concentration

EB   Emeraldine base

EIS   Electrochemical impedance spectroscopy

ES   Emeraldine salt

ETO   Ethylene oxide

FE-RE   Fast-cure epoxy-based RE

FEP   Fluorinated ethylene propylene

H^+ Hydrogen ion

HCl   Hydrochloric acid

Hg/Hg_2Cl_2 Mercury/Mercurous chloride

IHP   Inner Helmholtz Plane

Ir   Iridium

$IrCl_4$ Iridium tetrachloride

IrO_2 Iridium dioxide

IrO_x Iridium oxide

ISE   Ion-selective electrode

K^+ Potassium ion

KCl   Potassium chloride

KOH   Potassium hydroxide

$LiClO_4$ Lithium perchlorate

LiOAc   Lithium acetate

LOD   Limit of detection

$MnCl_2$ Manganese chloride

MO_x Metal oxide

NaCl   Sodium chloride

NaOH   Sodium hydroxide

NH_3 Ammonia

NO_x Nitrogen oxide

OCP	Open circuit potential
OHP	Outer Helmholtz Plane
Op-amp	Operational amplifier
PANi	Polyaniline
PbO_2	Lead dioxide
PDMS	Polydimethylsiloxane
PEG	Polyethylene glycol
PMMA	Polymethyl methacrylate
Pt	Platinum
PVAc	Polyvinyl acetate
PVB	Polyvinyl butyral
PVC	Polyvinyl chloride
$Ru(OH)_3$	Ruthenium (III) hydroxide
RuO_2	Ruthenium (IV) oxide
SARA	Subacute rumen acidosis
SCE	Saturated calomel electrode
SHE	Standard hydrogen electrode
SnO_2	Stannic oxide)
STD	Standard deviation
SWCNT	Single-walled carbon nanotube
Ti	Titanium
TiO_2	Titanium dioxide
UV	Ultraviolet
VAc	Vinyl acetate
VFA	Volatile fatty acid
WE	Working electrode
WO_3	Tungsten trioxide
ZnO	Zinc oxide

Chapter 1

Introduction

1.1 Importance of rumen monitoring

Climate change and global warming are major concerns, with impacts on every perspective of human life. Greenhouse gases (GHG) consisting of CO_2, CH_4 and NO_x are responsible for climate change [1], defined as the 'Greenhouse effect'. The reduction in the emission of GHG is important, and one area of interest is animal husbandry which is responsible for a large proportion of emissions [2]. It was stated in 2013 that 18% of total greenhouse gases were created from animal husbandry, mainly through animal digestion and meat production [3]. Due to the vast emission of GHG from animals (Figure 1.1), it is clear that ruminants account for 3% to 5% of the total GHG. Therefore understanding the rumen metabolic process is important for the alleviation of GHG emissions [4].
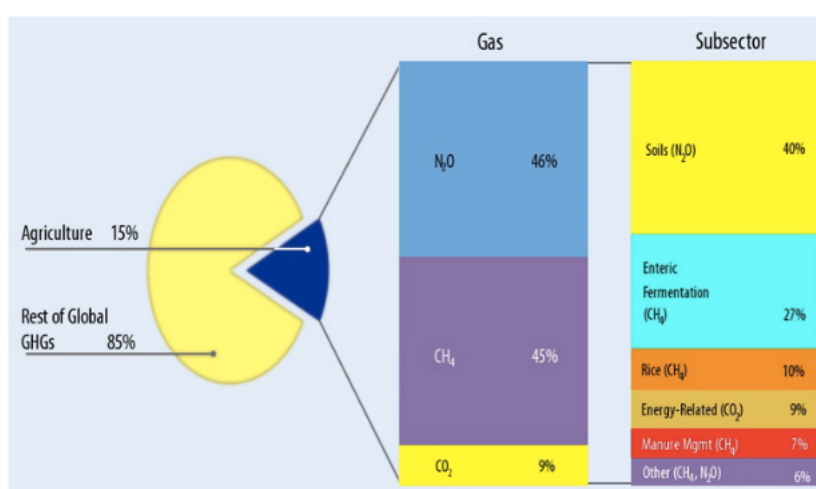
FIGURE 1.1: Contribution of the agriculture sector to GHG emissions [5]. CH_4 contributes 45% of the total GHGs in the agriculture sector.

Rumen monitoring provides one of the best ways to evaluate the health condition of livestock. The use of rumen devices has enhanced oestrus detection, farm management, disease identification and maintenance of feeding patterns. As the global population continues to rise, it has been reported that over 10% of people have no access to adequate food [6]. Given constricted land, the number of ruminants cannot continuously increase, requiring improvements in meat and milk production efficiency. With rumen monitoring, farmers can track and analyse cow rumination to choose the most effective feeding strategy and reduce potential loss due to unrecognized illness. For instance, high-forage diets are prone to higher CH_4 emission due to higher microbial rumen synthesis in comparison with concentrate-rich diets [7].

1.2   Rumen biology

The cattle's rumen is 25-50 gallons in size and is one compartment of the cow's stomach. The cow's stomach, consists of four compartments including the rumen, the reticulum, the omasum and the abomasum, and is an indispensable unit of the cow's digestive tract (Figure 1.2). The rumen weighs 1/7 to 1/10 of the animal's body. As the largest compartment, the rumen is a storage and fermentation place for the feed. It contains microbes, and the rumen fluid is a complex mixture of phospholipids, inorganic ions, gases, amino acids, dicarboxylic acids, fatty acids, volatile fatty acid (VFA), glycerides, carbohydrate and cholesterol esters [8]. Feedstuffs can be converted to VFA, NH_3, CO_2 and CH_4 through fermentation. Although oxygen can be brought into the rumen through feed, it is rapidly replaced by the CO_2 and CH_4, creating an anaerobic environment. The generated waste gases rise to the upper partition of the rumen where it is subsequently expelled through eructation.

The rumen microbiome consists of anaerobic bacteria, protozoa, fungi, methanogenic archaea and phages [6]. A symbiotic relationship is generated between the microbes and the host, supplying energy from the breakdown of plant cell wall carbohydrates. Whilst the exact function of most microbes is still unknown, anaerobic bacteria are the most common group in the rumen biological system, carrying out enzymatic activities. The existence of rumen protozoa is found from birth with subtle changes over the life span for ruminants, linked to fiber degradation and methane output reduction [10]. Rumen fungi, which contribute to 10-20% of rumen microbiome, are another group of microbes showing a strong fiber degradation effect.

1.3   Important parameters within rumen

In order to study the metabolic process, several parameters are to the rumen condition, such as pH, Oxygen reduction potential (ORP), conductivity and Dissolved oxygen
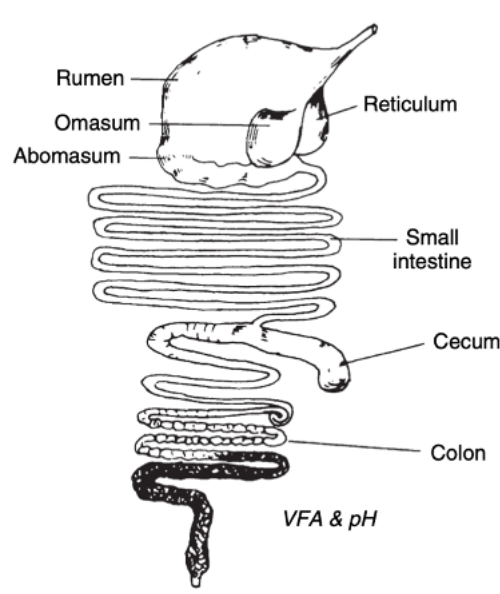
FIGURE 1.2: Composition of a cow's digestive tract [9]. It includes a four-compartment stomach (rumen, reticulum, omasum, and abomasum), small intestine, cecum and colon.

(DO).

Rumen pH is tightly related to the CO_2 concentration within the rumen since the formation of carbonic acid reduces the pH level. The typical rumen pH lies in the range of 5.6-6.7 [11]. The rumen pH is attributed to rumen acid-base regulation when small proportions of VFAs and lactic acid are produced through microbial fermentation of feed. However, the insufficient removal of VFAs could lead to excessive accumulation of VFAs, which also triggers an abnormal pH decrease [12]. Simultaneously, in a more acidic environment, a high concentration of dCO_2 would induce diffusion of rumen CO_2 into the bloodstream, leading to latent nutritional diseases such as subacute rumen acidosis (SARA) which is seen as a repetitive pattern of rumen pH below 5.2-5.6 where the duration of each pattern implies severity [13, 14]. Apart from health monitoring, there is a pressing need for elevating ruminant production to satisfy meat and milk requirements [6]. As a consequence, the quality of meat and milk has to be investigated depending on the feed. It has been reported that a higher feed efficiency could reduce rumen methanogenesis [15]. When varying feed compositions, rumen pH is a good indicator of digestion behaviour and feed intake [16], potentially contributing to higher feed efficiency and effective farm management.

Alongside pH, ORP is another important factor of the rumen environment. It is important to measure the redox potential within rumen fluid because livestock obtain nutrition and energy through electron transfer [17]. ORP serves as an indication of bacterial activity and enzymatic processes inside the rumen [18]. A comprehensive graph elucidating the fermentation process is shown in Figure 1.3 [19]. The rumen microbiota is known to metabolize more than 90% of hexoses, which are derived from the
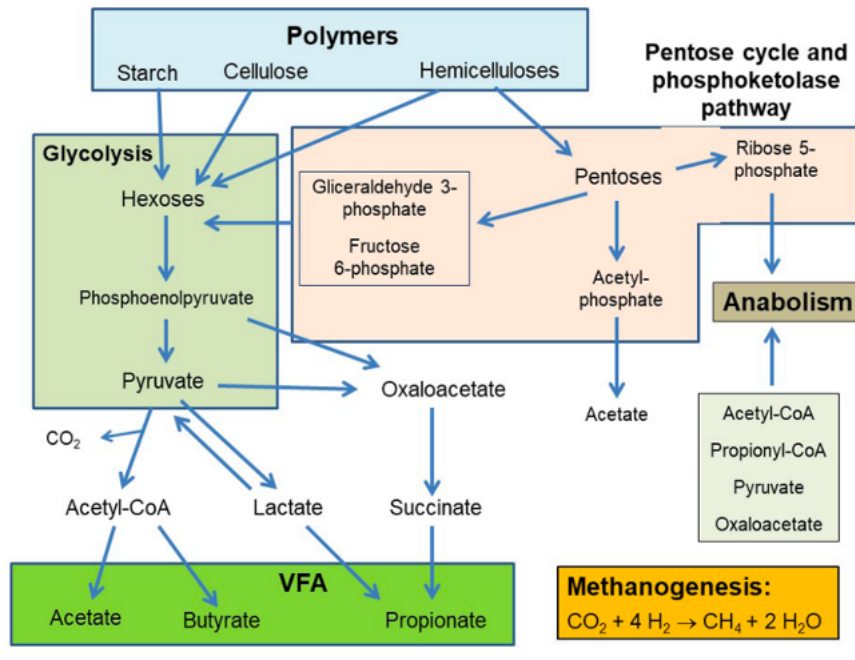
FIGURE 1.3: Fermentation scheme within rumen environment [19].

breakdown of complex carbohydrates like cellulose and starch, into pyruvate through the glycolytic pathway. Pyruvate serves as a pivotal junction for various pathways that result in the formation of the three primary volatile fatty acids (VFAs) - acetate, propionate, and butyrate [19]. Plant structural carbohydrates, such as hemicelluloses, are also abundant and contain high levels of pentoses [20]. Referring to Figure 1.4, generally, a reductive environment is created inside the rumen caused by microbial fermentation and methanogenesis (equation (1.1)), showing a negative ORP, estimated between -100mV to -250mV.

$$CO_2 + 4H_2 \rightarrow CH_4 + 2H_2O \qquad (1.1)$$

This estimation is proved by Huang et al. who reported that an average ORP of -178.1mV against a standard hydrogen electrode (SHE) was calculated from 35 studies, with a strong relation between pH and ORP [21]. An increase in rumen pH leads to an ORP drop in most cases [22]. In addition, rumen ORP is dependent on the feed and the internal microorganism, and positively linked to the concentrate in diet [23].

Conductivity measurements have been widely used in milk production to assess changes in cow activity and for clinical diagnoses [24]. However, the conductivity of rumen fluid is rarely investigated. Conductivity could give a better understanding of the nutritional elements and ion activities during the fermentation process [25, 26], as well as the appetite and health condition of a cow [27].

It is well-known that an anaerobic condition is formed within the rumen, meaning the
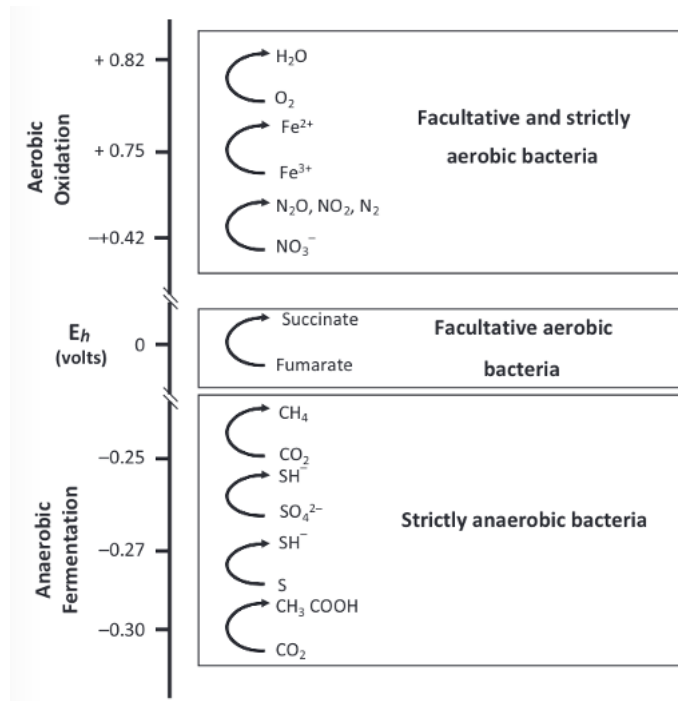
FIGURE 1.4: Redox potential pathway [21]. Typical chemical reactions are demonstrated at the corresponding ORP range.

dissolved oxygen concentration (DOC) is extremely low (below 50 µg/L) [28]. However, it is still imperative to monitor the DO level as oxygen is consumed and displaced to generate CO_2 and CH_4 during the methanogenesis [9]. Further, with a DO sensor it should be possible to distinguish certain states of the cow when a DO spike occurs during eating or drinking.

Therefore, by measuring parameters, such as pH, ORP, conductivity and DO, in the rumen, diseases can be diagnosed faster, the rumen environment can be further understood and the food utilized to feed the livestock can be adjusted to ensure an appropriate diet and a friendly environment [29, 30]. This project aims to develop a continuous measurement platform that enables the measurement of all these factors using microfabricated chips, which is suitable for both ex and in vivo measurements in rumen fluid.

1.4 Challenges in rumen sensing

The idea of developing such a system is novel and challenging as discussed below.

For the past decades, rumen pH measurements have been achieved by sampling such as rumenocentesis, oro-rumen probes (Figure 1.5) or direct sampling through rumen cannula [31, 32, 33]. Only a few attempts have been demonstrated for real-time pH

monitoring showing reasonable measurement accuracy [34, 35]. Continuous pH monitoring is imperative as there can be a large daily variation of up to 1 pH in the rumen [36]. Very limited data is collected for ORP, conductivity and exact DOC in rumen fluid. Large variations from -115mV to -384mV were observed in rumen ORP among the available 35 studies [21].

FIGURE 1.5: Rumen fluid collection via an oro-rumen probe and a suction pump [37].

Existing rumen systems in general only measure 1 or 2 parameters of the environment and utilize commercial sensors [35, 38, 39]. The integration of more than one sensor on a single chip for in vivo measurement is challenging because of the constrained chip size (at least 100mm long for any commercial probe). The system needs to be versatile to incorporate different sensors and interface designs

Lastly, bio-fouling, the accumulation of substances such as microorganisms and protein on the wet surface, is a common issue when measuring in vivo [40, 41, 42]. The measurement device can be easily blocked after insertion and proper packaging and measuring techniques are necessary for accurate data collection.

In conclusion, the aforementioned challenges referring to the integrated system should be considered thoroughly when designing a system. The intention herein, therefore, is to design a system to detect and measure different parameters in the rumen.

1.5   Thesis structure

The structure of the thesis is outlined below:

- Chapter 1 introduces the motivation for the project, background information on the rumen, and the challenges of the project.

- Chapter 2 provides the history and theoretical basis of different sensors that were tested in this project, together with the current state of the area and limitations of the rumen sensor system.

- Chapter 3 summarizes the fundamental theories of electrochemistry, including the electrode-electrolyte interface, equivalent circuit model and typical measurement method for electrochemical sensors.

- Chapter 4 describes the design and laboratory testing of RE, pH, ORP, DO and conductivity sensors, and discusses the feasibility of each sensor for usage in rumen fluid.

- Chapter 5 presents the design of the integrated sensor chip and tests of pH, ORP and conductivity in vitro in rumen fluid samples.

- Chapter 6 covers conclusions and makes suggestions for future development.

1.6   Thesis contribution

This project developed a miniaturized multi-sensor platform to measure pH, ORP and conductivity for rumen monitoring. Although the RE and oxygen sensors were not suitable for in vitro experiments, new applications under less harsh environments could be explored based on laboratory tests.

The main contributions of this project are:

- Miniature dissolved oxygen sensor with fast response (100ms) with detection range 1-8mg/L. A fast response can enable real-time detection and reduce the power consumption of the DO sensor.

- Miniature conductivity sensor with comparable performance to commercial products with long-term stability over several feeding cycles during in vitro test in rumen fluid.

- Miniature pH sensor with comparable performance to commercial products for rumen monitoring during in vitro test in rumen fluid.

- Miniature integrated sensor platform with multiple sensors, potentially applicable for in vivo rumen measurements after further testing and development.

Chapter 2

Literature review

In order to produce a system with multiple sensors, the background of each sensor is discussed, including the measurement technique, working principle, outcome and related work. Contemporary rumen systems are summarized to demonstrate the novelty of this project.

2.1 Reference Electrode (RE)

When an electrochemical sensor is used to detect chemical or ionic species, it is common that the working electrode (WE) in the two-electrode electrochemical system (or WE and counter electrode (CE) in a three-electrode configuration) in direct contact with the sample, operates against a chemical ground, provided by a RE. The RE provides a stable potential over the measurement period independent of the ambient environment. Ion-selective electrodes (ISEs) measure the ion concentration using potentiometry referenced against a RE [43, 44], but temporal measurements with miniaturised RE are still far from satisfactory [43]. Ag/AgCl REs are widely used on account of their environmental compatibility and reliability. Although Hg/Hg_2Cl_2 or calomel electrodes have exceptional potential stability and light inertness, the toxic characteristic of mercury restricts their widespread use in environmental and implantable applications [44]. The SHE provides the reference zero standard potential at standard state (ion concentration of $1mol/dm^3$ and 1atm pressure), but the miniaturization of SHE is arduous due to the requirement of gas chambers and pressure regulators [45].

For a Ag/AgCl RE, potassium chloride (KCl) is used as the electrolyte because of equal ion mobilities of both K^+ and Cl^-. The operating principle is based on the reactions taking place on the surface of the electrode:

$$Ag_{(a)}^+ + e^- \rightleftharpoons Ag_{(s)} \tag{2.1}$$

$$Ag^+_{(a)} + Cl^-_{(aq)} \rightleftharpoons AgCl_{(s)} \tag{2.2}$$

with the electrode potential given by:

$$E = E_0 - 2.303 \frac{RT}{nF} log([Cl^-]) \tag{2.3}$$

where E_0 is the standard electrode potential, n is the number of electrons in the electrochemical reaction, R and F are the molar gas constant and Faraday constant respectively, T is the temperature in K, and [Cl⁻] is the concentration of chloride ions.

This equation shows that the electrode potential is directly proportional to the Cl⁻ concentration (for a fixed temperature) with a slope of -59.16 mV/decade at room temperature (25°C). The development of the RE is illustrated in Figure 2.1 [44], showing how the electrolyte is encapsulated in a glass tube with an electrode constructed from a silver wire covered by silver chloride. In order to establish a constant anion concentration, a saturated KCl solution is used. A porous glass frit is placed at the bottom to enable ion exchange between the test and embedded solution [46]. Double junction REs (DJREs) are favoured commercially instead of single junction RE. By adding an additional compartment containing the KCl solution, the leakage from the inner electrolyte is alleviated, minimizing drift and augmenting long-term stability. However, drawbacks of the liquid system include position dependence, the limited possibility for miniaturization, mechanical fragility, constrained temperature, limited pressure range, and loss of electrolyte motivating improvement towards a solid state REs [43]. Gel-
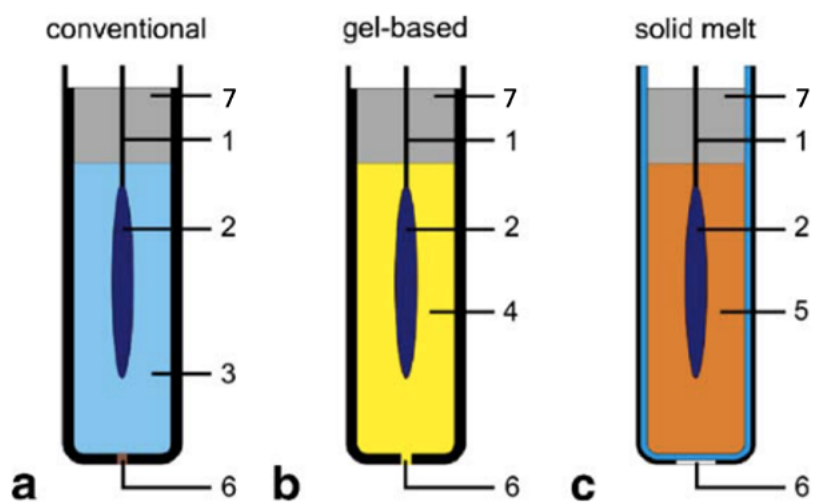
FIGURE 2.1: a-c Basic principles of a RE (e.g. Ag/AgCl reference element) [44]. 1 Metal lead (Ag), 2 hardly soluble metal salt (AgCl), 3 aqueous solution containing the related anion (KCl), 4 hydrogel-trapped KCl solution, 5 solid melt of the metal salt (KCl), 6 junction (diaphragm, porous ceramic or opening), 7 insulating encapsulation material.

based REs have been developed to meet high temperature and pressure requirements (Figure 2.1b). KCl paste is doped in a gel such as agar-agar, gelatin or polyvinyl alcohol

[44]. In this configuration, an enclosed network is formed where the ions can move without obstruction. In this way a comparable performance can be achieved tolerating up to 121°C with a lower KCl concentration compared to liquid-filled REs. The major drawback of gel-based REs is the lack of long-term stability. Gel ageing and irreversible leakage can cause the deterioration in the performance of RE [44]. Several planar REs have been designed using gels [47, 48, 49].

All-solid-state REs have been developed over the past decades (Figure 2.1c). Many technologies have been proposed including thin-film technology [50], ink-jet fabrication [51], heat sealing [52], thick-film technology [53] and 3D printing [54].

An early trial is shown in Figure 2.2. A sealant layer (ESL, 240SB) is deposited on top of a salt matrix which is a mixture of KCl with either a commercial thick film overglaze or a polymer dielectric paste [53]. The novelty lies in the hydration port left during the fabrication where the salt matrix is in direct contact with the test solution. Because the reduced contact area contributes to less salt loss, as well as a more stable surface potential at the electrode. This type of thick-film RE is suitable for mass production with low cost [55]. An investigation of the influence of fabrication parameters was
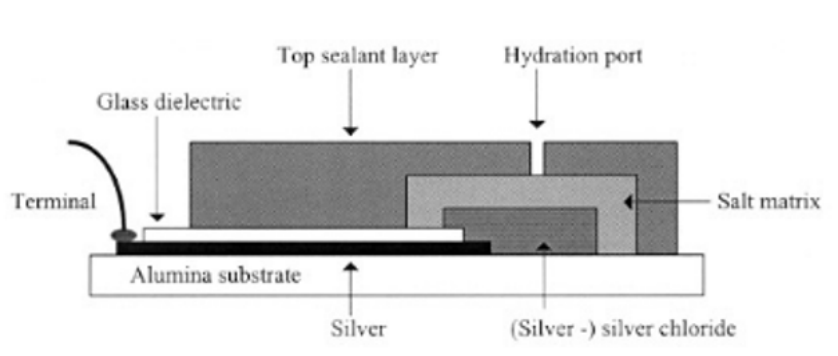
FIGURE 2.2: Planar design of a thick film RE [53]. A sealant layer is deposited onto the salt matrix covering the Ag/AgCl paste, leaving a small hydration port.

conducted by Atkinson et al. [56]. The importance of binder materials and the initial salt concentration was discussed in the investigation. The thickness of the device and the salt matrix contributed to the performance of the RE in terms of hydration time and lifetime. A trade-off between the drift rate and the hydration period was reported. The hydration period is defined as the time taken for a RE to reach a steady output after being immersed in the solution. A thicker salt matrix layer took longer to hydrate but had a lower potential drift.

To mimic the operation of the traditional RE, a double junction design was implemented by building an electrolyte bridge with two successive salt matrix layers [57]; a cross view is provided in Figure 2.3. The Cl⁻ sensitivity was decreased to as low as 2mV/decade while faster hydration was observed with the additional salt matrix.
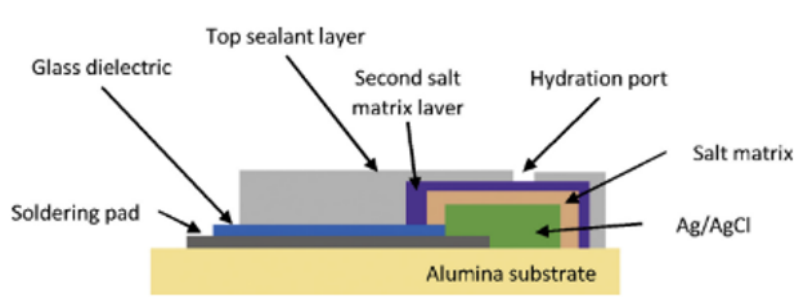
FIGURE 2.3: Cross view of a double junction planar RE [43]. A second salt matrix layer was introduced to mimic the operation of a DJRE.
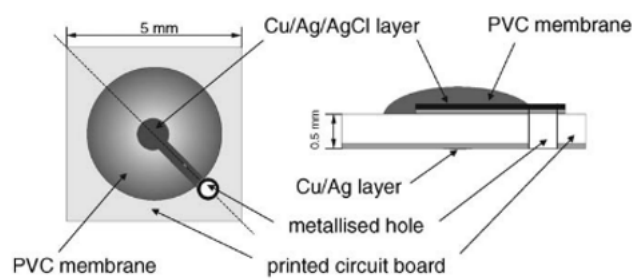
FIGURE 2.4: Top view (left) and schematic cross-section (right) of an all-solid-state reference microelectrode based on a PVC membrane containing ionic liquid [58]. The performance was comparable with a commercial RE except for the lifetime of 2 months.

A RE based on ionic liquids has been proposed [58]. Instead of the KCl electrolyte, an ionic liquid was placed in a polyvinyl chloride (PVC) membrane to supply Cl⁻ (Figure 2.4). The performance was comparable to a commercial RE except for the lifetime. Potential stability within 5mV was demonstrated over a 2-month interval, suitable for the production of an all-solid-state microelectrode.

A solid-state RE with comparable performance to a commercial RE was reported in [59]. Ag wire with electrochemically grown AgCl was employed as the sensing agent. During salt matrix fabrication, KCl was mixed with polyvinyl acetate (PVAc) powder, Vinyl acetate (VAc) monomer and photoinitiator DMPP followed by Ultraviolet (UV) curing. The Ag/AgCl wire was inserted into the composite during curing before the mixture became hard. Another group of RE was created by depositing a second salt matrix based on the same fabrication procedure except that another equitransferent salt, lithium acetate (LiOAc), was utilized as the electrolyte instead of KCl. It was concluded that the Cl⁻ leakage into the sample was highly suppressed through a double junction configuration with even better behavior than a commercial liquid junction RE. A potential stability of 1mV was achieved under pH variation or cation/anion change within the sample. Long-term stability was not tested for the samples containing two salt matrixes. However, one may presume that excellent performance could be achieved for long period judging from the available data.

Polyvinyl butyral (PVB) was investigated as the encapsulation material for a solid-state

RE [60]. The membrane comprised a Ag/AgCl/Cl⁻ system where sodium chloride (NaCl) was the Cl⁻ donator. In order to make metallic Ag, the AgCl colloid within the cocktail was exposed to light to achieve the reduction of AgCl. After adequate conditioning, the Cl⁻ selectivity was reduced to as low as 0.3mV/decade. The lifetime in constant operation was reported to be 20 hours, and it was insensitive to light, pH variation between 4-10 and redox species. In addition, the PVB membrane was used in thin-film and ink-jet printing designs [61, 62] where a lifespan of 3 months was achieved by ink-jet printing.

The Quasi-Reference electrode (QRE) is a special type of RE used for a variety of potentiometric, amperometric and voltammetric sensors [43]. Ideally, any electrode can be regarded as a QRE as long as it possesses a stable potential in the measuring environment under strict conditions, such as no ionic concentration variation. A pure Ag/AgCl QRE, which is also a Cl⁻ sensor, can provide a constant potential when the Cl⁻ concentration is constant in the electrolyte. Meanwhile, Cl⁻ concentration can be determined by the conductivity change measured from the conductivity sensor when Cl⁻ constitutes the majority of anions within the electrolyte. Therefore, conductivity sensor can be used in conjunction with the QRE to monitor Cl⁻ concentration. Ag/AgCl electrodes can be fabricated in two ways. First, a commercial screen-printing or ink-jet printing Ag/AgCl paste can be directly printed onto a substrate to construct a Ag/AgCl layer. Secondly, Ag can be obtained through thermal annealing of Ag_2O [63] or electroplating using Ag^+-containing solution onto a Pt or Au surface. Ag-AgCl conversion can be initiated through anodization in chloride-containing solutions, chemical oxidation and thermal or plasma treatment in chlorine-containing atmospheres [64].

Other than Ag/AgCl electrodes, materials such as conducting polymers (CP) [65] and carbon nanotubes (CNTs) [66] have been used in REs. As discussed in [67], in this case, the potential does not depend on the ion concentration but is governed by redox reactions involving the CP, or is stabilized by the electrical double layer at the interface of high-surface-area solid contacts. CP REs were constructed using a PVC membrane containing KCl, lipophilic salts or ionic liquids [68, 69, 70] while a CNT based RE possessed photocured polymer membrane including KCl as Cl⁻ provider [66]. Overall, good linearity was observed in these configurations with a moderate lifetime of up to 50 days. However, the drawbacks and interference studies are not explicitly presented.

In conclusion, numerous efforts have been made to develop a miniaturized RE. Although Ag/AgCl RE is the popular solution, the long-term stability and Cl⁻ sensitivity are still far from the traditional Ag/AgCl RE. A compromise has to be made in most cases between the sensitivity and the drift in order to accommodate different applications. Consequently, a RE is required for implantable applications with a better overall performance in Cl⁻ sensitivity, long-term stability and lack of interference.

In this work, a miniaturized RE containing a new binder material, namely fast-curing epoxy, is proposed due to its porous structure and good insulation property. For laboratory tests and ex vivo studies, Ag/AgCl QREs were used as the RE for the sensors since the measuring solution composition is known and thus the potential of the Ag/AgCl electrode can be obtained. Moreover, with a commercial RE the Cl⁻ concentration of the solution can be measured accordingly using Ag/AgCl QREs. Two methods can be used to construct a Ag/AgCl QRE, including chemical conversion and screen-printing paste deposition. The performance of two types of QREs can be compared to obtain the most suitable QRE for rumen monitoring.

2.2   pH sensor

pH measurements have been performed for more than a century [71]. The term pH represents the logarithmic concentration of hydrogen ions (H⁺) in a solution where lower pH (<7) defines acidity and higher pH (>7) implies alkalinity according to equation(2.4).

$$pH = -log[H^+] \qquad (2.4)$$

A variety of methods have been used for pH sensing including colorimetric [72], optical [73, 74, 75] and electrochemical [76]. However, the electrochemical method attracts the greatest attention because of the simplicity of miniaturisation, low cost and high accuracy [76].

The most well-known sensor is the glass pH probe, which was invented in 1925 by Kerridge [77]. This type of pH sensor has been commercialised and is the standard in pH monitoring. An example of the sensor is shown in Figure 2.5, it consists of two electrodes, one RE and one pH electrode. The reference electrolyte with a constant pH is in a reference chamber. The inner electrolyte serves as a buffer and equilibrates with the outer measuring solution through the H⁺ selective glass membrane. Due to the difference in H⁺ concentration between the reference and the measuring department, an open circuit potential (OCP) is developed between the two electrodes. Hence, for OCP measurement (detailed in Chapter 3.3.1) of the monovalent ion (H⁺), the Nernst equation (2.5) gives the potential response of the sensor.

$$E = E_0 - 2.303\frac{RT}{F}pH \qquad (2.5)$$

The sensitivity of the glass pH electrode is -59.1mV/pH a room temperature (25°C), which is defined as a Nernstian response. It can be seen that the sensitivity of the pH sensor is influenced by the surrounding temperature.

Although the standard glass pH electrode offers excellent accuracy, sensitivity and detection range, it is bulky and difficult to miniaturize. The mechanical fragility and the
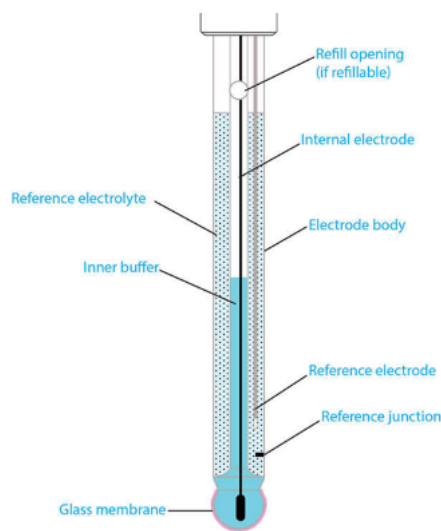
FIGURE 2.5: Structure of a glass pH probe [78]. The probe consists of two electrodes, one RE and one pH electrode. The reference electrolyte has a constant pH. The inner electrolyte serves as a buffer to equilibrate with the outer measuring solution through the H^+ selective glass membrane.

requirement for frequent recalibration are also major drawbacks of the glass pH electrode. Therefore, scientists have developed miniature pH sensors that provide similar performance to commercial pH sensor.

CPs, especially polyaniline (PANi), have been used as pH sensors because of the reversible reaction between emeraldine salt (ES) to emeraldine base (EB) [79]. A wearable potentiometric sensor was developed by Guinovart et al. by screen-printing to monitor wound pH [80]. It consisted of a PVB-based RE with PANi sensing electrode. It had a Nernstian sensitivity of -58mV/pH (for 5 sensors) in the pH range of 4.35 to 8, with a quick response time of 20 seconds. The reproducibility and repeatability of each sensor were good. A better CP-based pH sensor was reported using a PANi nanopillar array structure [81]. A Nernstian sensitivity of -60.3mV/pH versus Ag/AgCl RE was measured with a response time <1s within the range from 2.38 to 11.61. It was flexible and maintained the original sensor performance even after 1000 bending cycles. A drift of 0.64mV/h and 0.49mV/h from 5h to 12h was reported when immersed in pH 5 and 7 buffer solution. Other than PANi, other polymers (pyrrole, PyQH, aniline and oPD) were investigated by Santiago et al. [82]. Wire electrodes were coated with the polymers by electrochemical polymerization. The four polymers had near-Nernstian sensitivities lying between -43.2mV/pH to -50.7mV/pH. Another CP-coated pH sensor was constructed from a combination of 120mg Lithium perchlorate (LiClO$_4$) and 10μl pyrrole dissolved in 5ml acetonitrile [83]. This pH sensor showed a Nernstian response within 1s with a daily potential drift of 250 μV.

Metal oxide (MO$_x$) has been used for pH sensing. Metal oxides including TiO$_2$, SnO$_2$,

CeO_2, WO_3, PbO_2, ZnO, IrO_2 and RuO_2 have been implemented. In particular, Pt-group oxides, e.g. IrO_2, RuO_2, show outstanding performance with regard to accuracy and sensitivity [84]. The sensing mechanism of MO_x based sensors is explained by Mihell and Atkinson [85]. The pH response arises from the ion exchange in the surface layer containing -OH groups. A redox reaction is involved when the sensor enters a solution where the MO_x surface reacts with the H^+ and absorbs electrons to form water and higher or lower valency MO_x. The chemical reactions for RuO_2 and IrO_2 pH electrodes are summarized below:

$$2IrO_2 + 2H^+ + 2e^- \rightleftharpoons Ir_2O_3 + H_2O \tag{2.6}$$

$$2RuO_2 + 2H^+ + 2e^- \rightleftharpoons Ru_2O_3 + H_2O \tag{2.7}$$
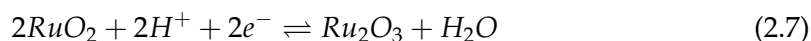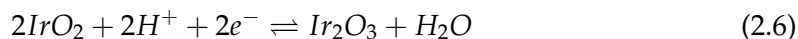
An IrO_x sensor was fabricated by sputtering the IrO_2 film onto stainless steel and tantalum substrates [86]. Good adhesion of the IrO_2 film was achieved for more than 2 months. The sensors exhibited Nernstian response up to 750 hours after immersion into buffer solutions. However, an ageing effect was observed on all sensors due to the decrease of E_0 from 800mV to 580mV. Using a similar fabricating process, Kreider produced a sputtered IrO_x sensor for a nuclear repositories system, giving a slope of -53 to -58mV/pH [87]. A new technique, namely the sol-gel process, for depositing the IrO_x film through heat treatment over 300°C of $IrCl_4$ coating solution was described by Nishio et al. [88]. An IrO_x sensor was made by coating an IrO_2 film onto a polyimide substrate with a thin Cr and Au layer to promote adhesion. A slope of -51mV/pH was obtained when calibrating between pH 1.5-12.1 against an on-chip Ag/AgCl RE. The 'carbonate melt oxidation' method was developed by Wang et al. for a long-term stable pH electrode [89]. The sensors were very stable in strong acid and alkaline solutions and showed the same sensitivity (-58.2mV/pH) even after 2.5 years. Anodic electrode-position of an IrO_2 film was developed by Yamanaka [90], simplifying the fabrication complexity to a large extent by eliminating the high-temperature treatment of the Ir base material. Utilizing this method, Marzouk et al. fabricated an IrO_2 based pH sensor for measurement of extracellular myocardial acidosis during acute ischemia, showing super-Nernstian sensitivity of -63.5mV/pH [91]. A drift of 0.2mV/h was measured with a reduction of 2.5mV/pH in sensitivity after a month. Chung et al. fabricated IrO_2 sensor arrays for pH monitoring of rabbit and human hearts with superior sensitivity (-69.9mV/pH) and linear temperature response [92]. Among all the fabrication methods, the anodic iridium oxide film (AIROF) possesses the highest sensitivity because the surface of AIROF is more porous ensuring higher ionic conduction from the hydroxyl groups [93].

RuO_x is also a good candidate for miniaturized MO_x pH sensors. The RuO_x film is usually deposited by sputtering or screen-printing. Liao et al. developed an array of RuO_2 pH sensors sputtered onto a silicon substrate [94]. A near Nernstian response of -55.64mV/pH was observed between pH levels 1-13 with a drift rate of 0.38mV/h.

The device was used for pH sensing of common beverages, and the RuO_2 sensor had a sensitivity of -58.8mV/pH from pH 2-12 with a response time of 30s [95]. The electrodes were subject to interference from redox agents and interference was reduced by a Nafion membrane. Screen-printing was used to make a pH sensor for water monitoring [96]. RuO_2 resistive paste was deposited onto a substrate to form a pH sensor with Nernstian sensitivity (-57mV/pH), the short response time (<5s) and long lifetime (>6months). Several other pH sensors fabricated using commercial RuO_2 paste showed a stable Nernstian slope of approximately -60mV/pH [97, 98].

A comprehensive comparison between IrO_x and RuO_x pH sensors was reported by Mingels et al. where the IrO_x film was constructed by anodic electrodeposition and the RuO_x film deposited by sputtering [99]. A super-Nernstian response was measured for the IrO_x sensors with a linear slope of -72.5mV/pH. Two types of RuO_x sensors were fabricated with the primary difference being the additional Ti seed layer and annealing step. The sensitivities for the RuO_x sensors were -56.3mV/pH and -55mV/pH. The long-term stability of the sensors was also investigated for 40 days at 37.5°C. It was concluded that a linear drift in either E_0 or sensitivity was observed for IrO_x sensors while the drift characteristics were not obvious ($\Delta pH < 0.2$) for the RuO_x sensors.

Nanomaterials including nanorods and nanotubes have been used to fabricate pH sensors. An intracellular pH sensor was made using ZnO nanorods, giving -50mV/pH sensitivity [100]. RuO_x nanorods were fabricated from $Ru(OH)_3$ an used to sense pH for organs-on-chip studies [101]. Single-walled CNTs (SWCNTs) have been used as pH-sensing materials for OCP measurement. A SWCNTs-based pH sensor, integrated into a microfluidic chip, had Nernstian sensitivity [102] while an inkjet-printed SWCNTs pH sensor had a sensitivity of -48.1mV/pH [103].

In addition to potentiometric pH sensors, there are other types of pH sensors such as conductometric sensors, capacitive sensors, ion-selective field effect transistors and extended-gate field effect transistors [76, 84].

However, due to the simplicity of fabrication and signal processing, potentiometric pH sensors are preferable and used here. In particular, a RuO_x pH sensor is used thanks to its low cost, ease of fabrication, bio-compatible property, high accuracy, good repeatability and long-term stability [99] compared with other miniaturised techniques.

2.3 DO sensor

DO is the amount of free oxygen in the solution. It is vital for environmental monitoring and topics such as water quality, cell metabolism and aquatic life [104]. The DO concentration can be measured using chemical, electrochemical and optical means.

In the Winkler method, iodine is used as an oxidant which is reduced to iodide or tri-iodide ion [105]. Manganese chloride ($MnCl_2$) and potassium hydroxide (KOH) are mixed to precipitate manganese hydroxide, followed by the reaction with DO. The potassium iodide is then oxidized to iodine. With the final thiosulfate titration, the DOC is derived based on the amount of thiosulfate consumed. The endpoint of the titration is indicated by a change in solution colour (starch method) or amperometric method [106]. The chemical reactions are:

$$Mn^{2+} + 2OH^- \rightarrow Mn(OH)_2 \tag{2.8}$$

$$4Mn(OH)_2 + O_2 + 2H_2O \rightarrow 4Mn(OH)_3 \tag{2.9}$$

$$4Mn(OH)_3 + 12H^+ + 4I^- \rightarrow 2I_2 + 4Mn^{2+} + 12H_2O \tag{2.10}$$

$$I_2 + I^- \leftrightarrow I_3^- \tag{2.11}$$
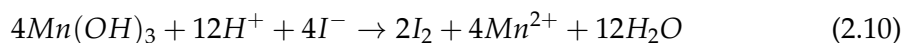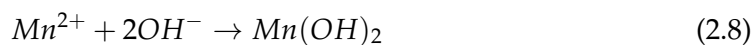
Although Winkler's method has the best accuracy (0.1%) and is the international standard method for DO measurement, it can only be used in neutral or weak acid solutions, even after improvement by Zhang et al. [107]. The gradual addition of thiosulfate solution prevents its use in real-time in situ measurement.

Fluorescent materials are used for optical DO sensing based on the quenching of a reaction with oxygen. In the presence of oxygen, the compound's fluorescence is restrained by keeping any excited electrons in the ground state. Consequently, the measured fluorescence intensity is linearly dependent on the DO concentration according to the Stern-Volmer formula:

$$\frac{I}{I_0} = 1 + K_{SV}C_{O_2} \tag{2.12}$$

where K_{SV} is the Stern-Volmer quenching constant, CO_2 is the oxygen concentration, I and I_0 are the intensities at measured DO concentration and at anaerobic condition.

An optical DO sensor using specific wavelength LEDs was developed for fluorescence detection [108]. It took at least 50s for the sensor to respond to the DO concentration but it was capable of measuring up to 40 mg/L DO. Another optical sensor with Ag nanoparticle doped sensing film was made by Jiang et al. with the K_{SV} increased by doping, giving a higher sensitivity. The operating range was 0-15 mg/L. The optical method in general has a high accuracy as well as a low detection limit. Also, the detection range is much higher than for electrochemical sensors. Regretfully, the stability is not good due to fluorescence quenching and optical sensors can be heavily affected by pH and temperature variation [109].

For electrochemical DO sensing, the Clark-type sensor has been widely used as depicted in Figure 2.6. A three-electrode system contains a WE, CE and RE. An oxygen-permeable membrane encloses the inner electrolyte and enables the diffusion of DO from the sample solution into the inner reservoir. A voltage is applied between WE

and RE for a certain period, and the current produced between WE and CE is proportional to the DO concentration.
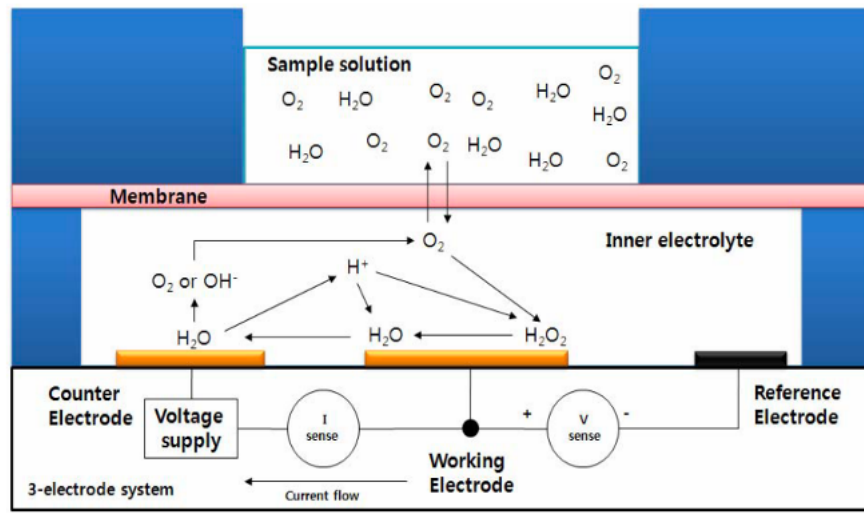
FIGURE 2.6: Configuration of Clark-type sensor [110]. A three-electrode system contains a WE, a CE and a RE. An oxygen-permeable membrane encloses the inner electrolyte and enables the diffusion of DO from the sample solution into the inner reservoir.

Because of oxygen reduction on the WE surface, the chemical reactions on the WE surface are:

$$O_2 + 2H^+ + 2e^- \rightarrow H_2O_2 \qquad (2.13)$$

$$H_2O_2 + 2H^+ + 2e^- \rightarrow 2H_2O \qquad (2.14)$$

The DO is reduced to water through two steps, with the intermediate formation of hydrogen peroxide. A variety of membrane materials have been explored for the Clark sensor, such as Teflon [111], Fluorinated Ethylene Propylene (FEP) [110], Polydimethylsiloxane (PDMS) [112] and low-density polyethylene [113]. The advantage of the Clark sensor is that it can be easily miniaturised by microfabrication [109]. Decent linearities and sensitivities are acquired over a wide range of DO concentrations. A Clark-type DO sensor was fabricated with chlorinated hemoglobin as the WE material and PDMS functionalized with polyethylene glycol (PEG) for the membrane. A sensitivity of 20.7 $(\mu A/cm^2)/(mg/L)$ was measured for a DO concentration of 2-7 mg/L [114]. A DO sensor for measuring the respiratory activity of cells was reported by Hsueh et al. showing a sensitivity of 61.9 nA(L/mg) between 0 to 8.1mg/L with a limit of detection (LOD) at 0.14 mg/L. The CE was eliminated to save space. Sputtered Pt served as the WE, which was covered with silicone adhesive and Ag/AgCl was deposited for the RE [115].

Needle-type sensors [116], microelectrodes [117] and ultra-microelectrode arrays [104] have been developed for electrochemical in vivo DO sensing. One of the advantages of microelectrodes and ultra-microelectrode arrays is that the oxygen-permeable membrane, together with the inner electrolyte, is eliminated. The reason for the elimination

of the membrane is that the oxygen reaching the surface of the WE is rapidly dissipated and replenished during the CA measurement due to the microscale configuration, leading to a direct measurement of the DO concentration. For the same measuring technique the bare WE is in direct contact with the solution, further narrowing the required space and decreasing the response time to a minimum of milliseconds. Van Rossem et al. proposed an ultra-microelectrode array (36 microelectrodes) sensor yielding 0.49 nA($s^{-0.5}$L/mg) in the range of 0.8 to 7.8mg/L [104]. Finnerty et al. used bare Pt microelectrode for peripheral tissue oxygen detection. From calibration, the sensitivity was 0.79 nA/µM when measured versus saturated calomel electrode (SCE). A LOD of as low as 0.07 mg/L was observed.

Therefore, in this project microelectrode DO sensors were used due to their small size, ease of fabrication, low cost and simple integration with other electrochemical sensors. Although DO sensors with bare microelectrodes are influenced by bio-fouling [115], it is still worth trying as anti-fouling membranes can be deposited onto the WE to improve the in vivo performance [118, 119]. The DO sensor is important for rumen monitoring as it can serve as an indicator when the cow is drinking because rumen DOC increases in consumption of water as the DOC in water (8.5 mg/L) is much higher than the anaerobic condition in the rumen.

2.4   ORP sensor

ORP describes the ability of an aqueous system to accept or lose electrons. A reducing environment is created with a negative ORP reading while a positive ORP demonstrates an oxidizing environment. ORP detection is used in the field of water monitoring [120], soil fertility [121] and biological analysis [122]. As expressed by equation(3.11), a simple two-electrode system can be used to measure solution ORP as long as the WE does not participate in any chemical reaction, with a stable RE. A noble metal (Pt or Au) is used as the WE. Calibration of the ORP sensor is based on standard calibration solutions with a given ORP value, such as ZeBell's Solution, Light's Solution and Quinhydrone Solutions with pH buffer 4 or 7. Since a standard hydrogen RE is scarcely used in reality, it is necessary to correct the measured ORP values according to equation(2.15), where E_0 is the voltage between the WE and RE (Ag/AgCl) and C is the potential difference of any RE used vs the SHE.

$$E_h = E_0 + C \tag{2.15}$$

Although commercial ORP probes are available, the probes are bulky in size and not suitable for biological and biochemical applications that require microelectrode. A microelectrode made with platinum wire was used for ORP monitoring in biofilms [123].

The Pt wire was fixed into a glass micropipette leading to exposure of the Pt wire surface. From the results, the ORP varied as expected measuring the changes in microbial processes in two types of biofilms. Steininger et al. presented a study for ORP of chlorinated water using a Pt WE and Ag/AgCl RE [124]. The ORP reached a stable value of +876mV after 20 mins and stabilized over 16 hours with a standard deviation of 2mV. A multi-sensor system was developed utilizing only bare Pt microelectrodes for pH, ORP and conductivity sensing [120]. The platform measured ORP from 150mV to 800mV as well as the pH from 4 to 10 in water. Au micromachined arrays were developed by Lee et al. for in situ ORP sensing [125]. A 200nm thick Au layer was deposited onto the tips of microprobes to make ORP measurements. The sensors showed a fast response time of <1s in different calibration solutions and excellent accuracy with a maximum deviation of 15mV.

This work used a bare Pt microelectrode in the sensing system for ORP detection due to its inert property. The electrode needed to be properly cleaned prior to measurement in order to give good accuracy and rapid response time.

2.5   Conductivity sensor

Electrical conductivity is the ability of a material to conduct electrical current, which is an intrinsic property of the material and is the reciprocal of resistivity. For the measurement of the liquid sample, the solution conductivity is given as:

$$\sigma = \frac{1}{\rho} = \frac{1}{R_S A} = \frac{\kappa}{R_S} \tag{2.16}$$

Where σ is the conductivity, ρ is the resistivity, R_s is the solution resistance and κ is the cell constant defined by the geometry of the sensor and the surrounding liquid.

Typically, two types of electrolyte conductivity sensors are used, namely inductive sensors and electrode sensors. Inductive sensors are constructed from a single or double transformer. The single transformer inductive sensor consists of a single coil and a protective case. The surrounding solution acts as the second coil when an AC excitation voltage is applied to the coil. By measuring the primary current, the solution resistance and in turn the conductivity can be calculated based on the real part of the current with a given cell constant. The double transformer inductive sensors utilize a transformer for signal excitation and another transformer for signal detection. A voltage drop is obtained due to the liquid resistance loop between two transformers. Therefore, an inverse relation is found between the measured current from the receiving transformer and the solution resistance from which the electrical conductivity is acquired [126, 127].

Electrode conductivity sensors are mainly classified as two-electrode and four-electrode sensors. A two-electrode sensor has two conducting electrodes immersed in the solution. Two measurement configurations for two-electrode cells are illustrated in Figure 2.7(a & b). Either an AC current or an AC voltage source can be used to excite the circuit, after which the voltage or the current is measured. With information on the current and voltage, the circuit impedance can be calculated and the solution resistance determined. Hence the electrical conductivity of the solution is measured if the cell constant κ is a constant. For instance, if the two electrodes have the same dimension with an area of 10 cm^2 and are 1 cm apart in the parallel plate configuration, κ is the distance divided by the electrode area giving 0.1 cm^{-1}. Note that the calculation of κ ignores the fringing field outside the electrodes. However, due to the double-layer capacitance (C_{dl}) at both electrode-electrolyte interfaces, the voltage drop across the capacitance can influence the accuracy of the measurement, namely the polarisation effect. Therefore, the measured magnitude will be higher than the actual solution resistance. Although high-frequency excitation can diminish the polarisation effect, stray capacitance from the connection wires and the bulk solution will interfere with the output, leaving a very limited usable frequency range.

The configuration of four-electrode conductivity sensors is shown in Figure 2.7(c). An AC current is injected into the outer two electrodes while the voltage drop between the inner two electrodes is detected. The merit of the four-electrode configuration is that the polarisation effect can be removed since no current flows through the double-layer capacitance of the inner electrodes owing to the high input impedance of the voltage meter. As a result, the ratio of measured V and supplied I can accurately represent the solution resistance R_s.
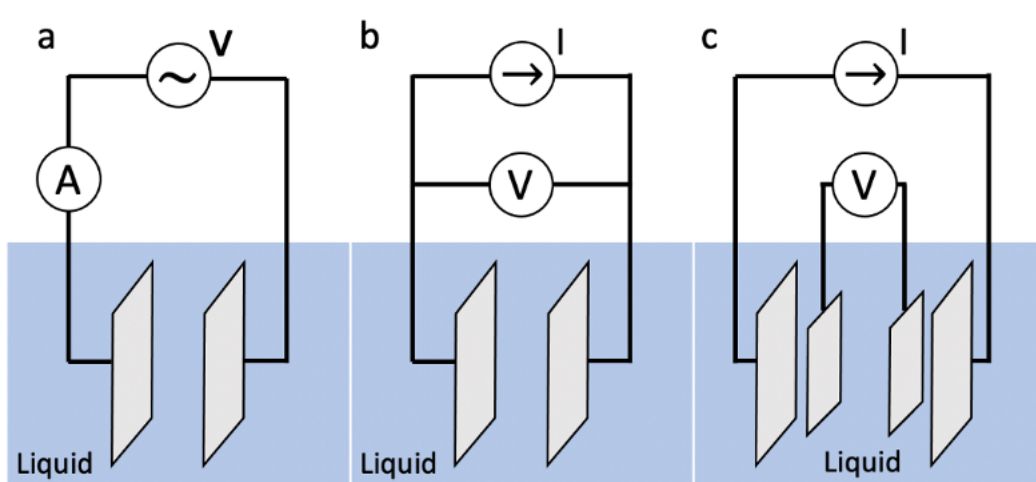
FIGURE 2.7: Electrode conductivity sensor configurations: (a) two-electrode V-I configuration, (b) two-electrode I-V configuration and (c) four-electrode configuration.

Different geometric designs have been used for two-electrode or four-electrode conductivity detection. The simplest design is the parallel plate electrodes. The Jones-type

cell was invented with two electrodes separated by a glass channel and a cell constant ranging from 0.1 cm^{-1} to 60 cm^{-1} [128]. It enabled resistance measurement between 100Ω to 100kΩ. However, due to its large size and mechanical fragility, parallel plate electrodes are rarely employed.

Van der Pauw type conductivity sensors have four electrodes around a cylindrical cell where the AC current is injected from electrode 4 to 1 and the voltage across electrode 2 and 3 is noted [129]. Ideally, for a symmetrical design, the cell constant depends on the height (h) of the cell, calculated as:

$$\kappa = \frac{ln2}{\pi h} \tag{2.17}$$

The symmetrical location of the electrodes is challenging for the Van der Pauw type sensors (Figure 2.8) because of the small width of the thin rods. One way to overcome the issue is to use stainless steel electrodes [130]. The same current is injected through electrode 1, 2 and 1, 4 by sequence, followed by voltage detection across electrode 3, 4 and 3, 2. The two voltage outputs were not the same unless a symmetrical configuration was developed. The conductivity measurements were conducted between 0.01 mS/cm and 2 mS/cm, showing a maximum error of 1% and excellent repeatability.
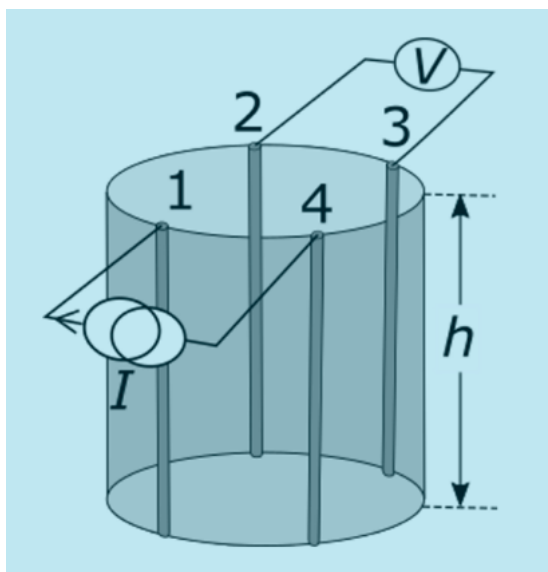
FIGURE 2.8: Schematic of Van der Pauw type conductivity sensor [131]. The AC current is injected from electrode 4 to 1 and the voltage across electrode 2 and 3 is measured.

Planar conductivity sensors are commonly used for electrolyte conductivity measurement. These sensors are easily scaled down with microfabrication onto different substrates such as borosilicate glass [132] and Pyrex [133]. A pair of Ag/AgCl disc electrodes was used for conductivity detection of a saline solution between saline concentration 0.5g/L to 5g/L [134]. A system with two and four interdigitated electrodes was developed by Brom-Verheijden et al. for conductivity sensing in KCl solution

[135]. Compared with the commercial sensor possessing the same cell constant, the two-electrode sensors had a good match over 10-500 μS/cm while the four-electrode sensors extended the range to 3-12000 μS/cm using an excitation frequency of 100-10kHz. Rustomji et al. developed a calibrated thin-film planar four-electrode sensor with a standard lithium battery electrolyte and acetonitrile-based electrolyte, giving an error of 6% over the range 0.1-100 mS/cm [132]. Among the planar electrode sensors, Pt is mostly used as the electrode material due to its chemical inertness and long-term stability. It is difficult to directly calculate the cell constant of the sensors for a planar configuration due to the non-uniform field distribution [131].

To conclude, electrode conductivity sensors are preferred over inductive sensors due to their ease of miniaturisation as long as a durable material (Pt) is selected. In general, four-electrode conductivity sensors have a larger measurement range and better accuracy, especially for solutions with high ionic strength. Therefore, for rumen measurement where the typical conductivity is in the mS/cm range, a miniature planar four-electrode conductivity sensor was used.

2.6 Existing rumen monitoring systems

The development of rumen probes can be traced back to 1955 when Lamphila set up an experiment to measure the pH and VFA concentration in an Ayrshire cow [136]. Both in vitro and in vivo experiments were conducted while a long lead (2.5m) was connected to a pH meter to make in vivo measurements. A large acidity difference, 1.1pH was revealed between the upper side of rumen and the lower side of rumen. Meanwhile, pH values from in vitro measurements were much higher (0.15-0.65pH) than in vivo results. Since then, numerous attempts had been made using oral probes or direct measurements via the rumen fistula [137]. As for rumen ORP, the earliest record was attributed by Broberg in 1957 where the ORP of rumen fluid was measured in vitro, giving a value of -385 to -430mV [21]. Various diet compositions have been examined in sheep, goats, alpacas and dairy cows to investigate their influence on rumen ORP [21]. Measurement of pH and ORP have attracted attention for the past two decades due to the need to diagnose SARA and rumen metabolism studies. However, techniques need improving due to low accuracy, and lengthy and bulky procedures.

To address the issue, new rumen monitoring systems have been investigated. A device was made by Marden to measure pH and ORP in dairy cattle [39]. A manual suction-strainer device was used to pump rumen fluid out from a cannulated animal, followed by in vitro measurement using a commercial glass pH electrode, a platinum ORP sensor and a temperature sensor. An obvious pH drop was recorded after feeding with a maximum variation of 0.54pH within 8 hours of experiments. ORP was -173.5 to -216.8mV within 8 hours. A slow decrease of ORP was observed after the meal, which

was explained by oxygen uptake by microorganisms. The rumen partial pressure was also calculated based on ORP and pH, justifying the anaerobic rumen environment. A similar sensor system was used by Julien to compare measurement results from the in vitro and in vivo methods, suggesting insufficient accuracy of in vitro experiments.

Rumen boluses have been introduced due to their noninvasive property, as well as the capability of continuous in vivo monitoring of pH, temperature and ORP. Initially, boluses were placed exclusively in fistulated cows as cable connections were needed to a data logger [138]. Recent advances in wireless communication technology enable wireless communication to a rumen monitoring system. A battery-powered bullet shape bolus was created by Sato et al. with a glass pH electrode encapsulated by stainless steel and polypropylene [139]. A mean variation of 0.2pH was measured over 2 months in Holstein dairy cows. By feeding acidosis-inducing diets, this wireless system paved the way for the accurate assessment of SARA. In 2006, a wireless measurement system (LRCpH) was developed to collect continuous rumen pH data, shown in Figure 2.9 [34]. In the design, a pH electrode from Sensorex was protected from the rumen epithelium by a shroud with holes to encourage rumen liquid contact. The bottom weights helped the capsule sit in the desired position within rumen. It was shown that accuracies of 0.13, 0.18, and 0.1 pH were acquired after immersion in the rumen for 24h, 48h and 72h respectively. Further, this system was adopted by Qin et al. to examine the effect of forage types on the fermentation parameters of lactating cows [35]. The in vivo experiments were implemented for 14 weeks while simultaneously measuring rumen pH, temperature and ORP.

FIGURE 2.9: Design of LRCpH wireless rumen measurement system [29]. A pH electrode from Sensorex was protected from the rumen epithelium by a shroud with holes to encourage rumen liquid contact. The bottom weights helped the capsule sit in the desired position within rumen.

In order to differentiate rumen pH based on diets, wireless rumen sensors comprising pH and temperature were utilized in dairy goats [140]. High- and low-forage-to-concentrate ratios were used as dietary treatments. It was found that the mean daily rumen pH was 0.31pH higher for goats fed with a high-forage diet and the rumen pH nadir was at 2-4 hours after feeding. A novel MOSFET pH sensor system was invented by Zhang et al. for monitoring wagyu [141]. A microfabricated RE and pH electrode meant that the overall package dimension was reduced to 22mm in diameter and 75mm in length. All components were sealed in a bio-friendly gel, with a lifetime of several days and an accuracy of 0.1pH. Table 2.1 summarizes typical rumen sensor systems in terms of the assembled sensors, methods and performance.

Rumen system	Sensors	Measurement method	Data collection method	Accuracy	Lifetime and dimension
J.P.Marden et.al [39]	Commercial glass pH electrode; Platinum electrode ORP sensor; Thermal temperature sensor	In vitro in rumen fluid sample of dairy cattle	Cable connection	N/A	N/A
K.Dieho et.al [36]	Commercial pH sensor (Sensorex)	In vitro in rumen fluid sample of Holstein Friesian dairy cows	Cable connection	N/A	N/A
C.Julien et.al [142]	Commercial glass pH electrode; Platinum electrode ORP sensor	In vitro and in vivo in fistulated dairy cows	Cable connection	N/A	N/A
M.Richter et.al [143]	Commercial glass pH electrode; Platinum electrode ORP sensor	In vivo in three dry Holstein cows	Wireless	N/A	Lifetime: 4 days; Package dimension: N/A

L.Zhang et.al [141]	MOSFET pH sensor	In vivo in a cannulated cow	Wireless	±0.1pH	Lifetime: Several days; Package dimension: Ø22x75 mm
S.Sato et.al [139]	Commercial glass pH sensor	In vivo in four Holstein dairy cows	Wireless	±0.2pH	Lifetime: 2 month; Package dimension: Ø30x145 mm
C.Qin et.al [35]	Commercial pH sensor (Sensorex); Platinum temperature sensor; ORP sensor	In vivo in eight rumen-cannulated Holstein cows	Wireless	0.13pH, 0.18pH, 0.10pH after 24, 48, and 72h in rumen [34]	Lifetime: 14 weeks; Dimension: 150mm in length
A.Castro-Costa et.al [140]	pH sensor; Temperature sensor	In vivo in eight dry goats	Wireless	±0.05pH; ±0.08°C	Package dimension: Ø27x145 mm

TABLE 2.1: Summary of existing rumen systems.

In addition to rumen systems reported in publications, commercial wireless rumen bolus have emerged from a variety of manufacturers, addressing the challenge of the short life cycles, as summarised in Table 2.2 [37]. These boluses typically measure pH and temperature via commercial pH probes and platinum temperature sensors.

Manufacturer	Name	Sensor type	Data collection method	Lifetime and Dimension
eCow Devon Ltd.	eBolus	pH; Temperature	Wi-Fi handset	Lifetime: 5 months Package dimension: Ø27x135 mm

smaXtec Animal Care GmBH	SmaXtec	pH; Temperature; Activity	Wireless	Lifetime: 5 months; Package dimension: Ø35x132 mm
UlikeKorea Co. Inc.	LiveCare Bio Capsule	pH; Temperature	LoRaWAN	Lifetime: 5-6 years; Package dimension: Ø25x100 mm
Moow	Moow Rumen Bolus	pH; Temperature	Wireless	Lifetime: 3 years Max; Package dimension: N/A

TABLE 2.2: Summary of commercial wireless rumen bolus. Reproduced from [37].

It is evident that apart from the work reported by Zhang et al. [141], almost all contemporary rumen systems rely on commercial pH probes, which are large and bulky, expensive for daily usage and slow in response. A functioning miniaturised pH sensor would be of great novelty for in vivo or even in vitro measurements in rumen fluid. Also, although several trials have been made to measure rumen ORP and pH concurrently in the same package, separate sensors are used for pH and ORP detection. Integrated sensors can further reduce the size and complexity during data collection and signal processing. So far, very limited platforms have been reported for conductivity measurement in vitro and in vivo albeit intriguing applications for rumen fermentation study [25].

Therefore, an integrated sensor platform suitable for rumen monitoring of pH, DO, conductivity and ORP is considered highly novel and valuable for animal husbandry.

2.7 Biofouling

For all in situ and in (ex) vivo sensors, biofouling is a common issue. It is defined as the accumulation of microorganisms such as bacteria, plants and small animals on submerged surfaces [144]. The biofilm is formed in a 3-stage process including attachment, colonisation and growth. Some molecules (i.e. fatty acids, lipids, proteins) are absorbed to the surfaces spontaneously after immersion of electrodes. Attachment is subject to the surface properties and the rate of microbial transport to the surface while

the latter two stages are affected by the transport of nutrients [145]. Conditioning films, therefore, block the performance of the sensor surface. The sensor characteristics can be influenced by biofouling in a variety of ways. Diffusion of the analyte to the electrode is inhibited by the film and hence the sensor will not be as sensitive as in a saline solution. The local pH and analyte concentration can differ from the bulk solution due to the hydrophobic domain, leading to errors. Moreover, the electrode-electrolyte structure can be altered based on the change of C_{dl} due to the absorption of molecules [146].

As for electrochemical sensors, biofouling has a great impact on the performance of DO sensors. For a micro-needle implantable DO sensor in intramuscular tissue and vascular blood, the current decreased dramatically when measuring ex vivo along with a reduction in the sensor sensitivities. in vivo measurement in intramuscular tissue was impaired even with an applied Nafion anti-fouling membrane [116]. Adopting the same Nafion membrane, Marland et al. developed a DO sensor for real-time measurement of tumour hypoxia. In a solution containing bovine serum albumin (BSA), the sensors exhibited lower output current and a shorter lifetime (24h) [119]. Greater variability of the measured steady-state current was recorded in subsequent in vivo validation. The group then tested a different oxygen-permeable membrane (poly(2-hydroxyethyl methacrylate) hydrogel) for monitoring intestinal tissue which suffered similar biofouling effects after implantation [118].

An implantable ORP sensor was reported by Baltsavias et al. for gut microbiome monitoring [147]. The sensor measured redox activities successfully for 12 days after fecal exposure. A long stabilization time of 22 hours was reported for the ORP sensor to recover to 30mV of the reference value, partially due to biofouling. Ag/AgCl REs can be affected by biofouling through increased impedance and electrode polarization, leading to a change in the output potential from the initial value [148]. Four-electrode conductivity sensors are less prone to biofouling than two-electrode sensors. However, signal outputs are still influenced by the proximity effect contributed by the electrode fouling [149].

2.8   Conclusion

This chapter summarizes the current status of different sensors with regard to basic theory, technique, fabrication and performance. The first part of the project focuses on the development of pH, DO, conductivity sensors and RE (Cl⁻ sensor), evaluated within calibration solutions. The sensors were integrated into microfabricated chips for substantial size reduction. The sensor response was monitored in vitro in order to test the performance for rumen monitoring.

Chapter 3

Measurement methodology

In order to perform electrochemical measurements with electrodes, it is important to understand the basic theory of the electrode-electrolyte interface and the general measurement techniques.

3.1 Electrode-electrolyte interface

When an electrolyte encounters an electrode the potential on the electrode leads to ion imbalance in the medium. As a result, an equilibrium is created when the exchange current balances and electrolyte bulk is maintained to be neutral. A detailed characterization of the behaviour is demonstrated in Figure 3.1. An inner Helmholtz Plane (IHP) is formed where ions are directly absorbed onto the surface. Attracted by the electric field, more ions move towards the interface, creating the outer Helmholtz Plane (OHP). IHP and OHP constitute the Stern layer which consists of tightly bound counterions. Additionally, a diffusion layer exists outside the Stern layer where the ions are affected by the electric field but not specifically bound. Consequently, the structure acts as a capacitor containing two layers, denoted as the electrical double layer. The C_{dl} is given in equation (3.1) and relates the change in the electrostatic potential to the distance y from the surface.

$$\partial^2 \phi(y) = -\frac{q}{\varepsilon_0 \varepsilon_r} \sum_i z_i n_{i0} e^{-\phi(y)\frac{q z_i}{kT}} \tag{3.1}$$

where ϕ is the potential, q is the electron charge, ε_0 is the permittivity of free space, ε_r is the relative permittivity of the electrolyte, z_i is the valence of the ions, n_{i0} is the number density of ions where the potential is zero (bulk solution), k is the Boltzmann constant, and T is the absolute temperature.
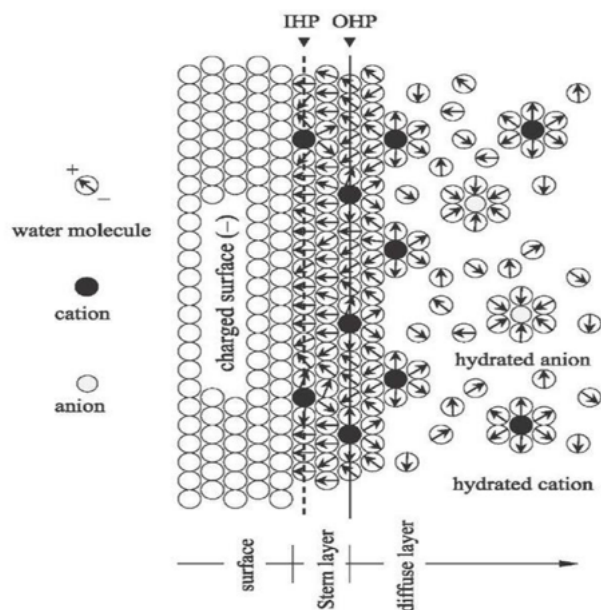
FIGURE 3.1: Ion behaviour at the electrode-electrolyte interface [150]. IHP and OHP constitute the Stern layer which consists of tightly bound counterions. A diffusion layer is constructed outside the Stern layer where the ions are affected by the electric field but not specifically bound.

Equation (3.1) can be simplified as:

$$\partial^2 \phi(y) = \kappa^2 \phi(y) \tag{3.2}$$

where for a symmetric electrolyte:

$$\kappa = \sqrt{\left(\frac{2z^2 q^2 n_0}{\varepsilon_0 \varepsilon_r kT}\right)} \tag{3.3}$$

The Debye length is defined as:

$$\lambda = \kappa^{-1} = \sqrt{\left(\frac{\varepsilon_0 \varepsilon_r kT}{2z^2 q^2 n_0}\right)} \tag{3.4}$$

when the potential at the distance of Debye length decayed to $1/e$ of the surface value.

However, the solution is only for a point charge. For an electrode surface, the Gouy-Chapman equation is:

$$\frac{\partial^2 \psi}{\partial y^2} = \kappa^2 \sinh(\psi) \tag{3.5}$$

with a dimensionless potential:

$$\psi = \frac{q}{kT} \phi \tag{3.6}$$

Solving the equation by combining Gauss's law yields the Grahame equation:

$$\sigma_0 = -\varepsilon_0 \varepsilon_r \phi_d \left(\frac{\sinh(\frac{\psi_d}{2})}{\frac{\psi_d}{2}} \right) / \lambda \qquad (3.7)$$

Where σ_0 is the surface charge density, ϕ_d and ψ_d are the dimensional and dimensionless diffusion layer potential respectively.

Equation (3.7) can be simplified when the applied diffusion layer potential is small and the effective double layer capacitance per unit area $C_{dl}{'}$ can be estimated from equation (3.8).

$$\sigma_0 = -\frac{\varepsilon_0 \varepsilon_r \phi_d}{\lambda} \Rightarrow C_{dl}{'} = \frac{\sigma_0}{\phi_d} = -\frac{\varepsilon_0 \varepsilon_r}{\lambda} \qquad (3.8)$$

One thing to be noted is that this estimate is made by only taking the diffusion layer into account. The capacitance of the Stern layer can be considered as an extra fixed capacitor on the electrode surface. In the case of low ionic strength, the capacitance of the diffuse layer dominates and the Stern layer capacitance can be ignored.

3.2   Randles model

In order to better investigate the electrode-electrolyte interface, an equivalent circuit model for small AC excitation of Faradaic sensors was developed by Randles, shown in Figure 3.2. Faradaic sensors have oxidation or reduction reactions at the electrode causing the flow of current. This model is widely used for electrochemical impedance spectroscopy (EIS) (detailed in Chapter 3.3.4). In Figure 3.2, Rs is the bulk solution resistance which is relatively small depending on the ionic strength of the electrolyte. Faradaic impedance containing charge transfer resistance (R_{ct}) and Warburg impedance (Z_W) is included in parallel to the C_{dl}.
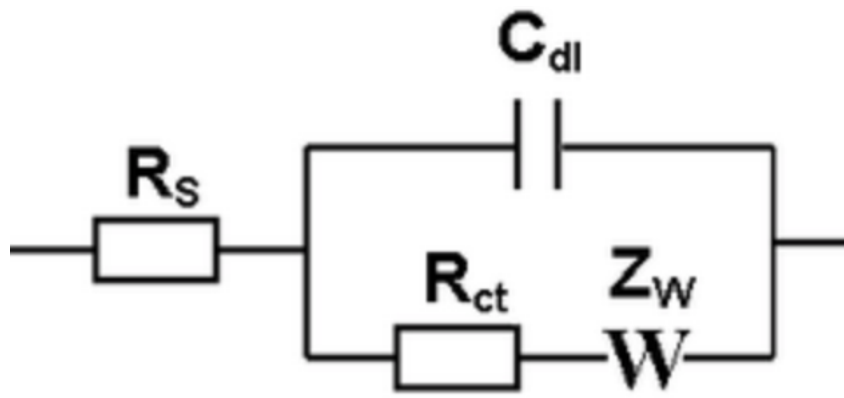
FIGURE 3.2: Randles circuit model for small AC excitation. The bulk solution resistance is connected in series with C_{dl} which is in parallel to the faradaic impedance containing R_{ct} and Z_W.

When the reaction occurs at the electrode-electrolyte interface, electrons are transferred between the electrode and the electrolyte. Hence other than the C_{dl}, a leakage current is produced because of the electron transfer, indicated by an impedance at the interface. Specifically, for small AC excitations R_{ct} is a resistor representing the net current based on the direct charge transfer from the electrode to the electrolyte [131]. Z_W models the diffusion-controlled mass transfer at the interface depending on the frequency:

$$Z_W = \frac{A_W}{\sqrt{\omega}} + \frac{A_W}{j\sqrt{\omega}} = \frac{\sqrt{2}A_W}{(j\omega)^{1/2}} \tag{3.9}$$

with:

$$A_W = \frac{RT}{\sqrt{2}n^2F^2A}\left(\frac{1}{D_O^{1/2}C_O^*} + \frac{1}{D_R^{1/2}C_R^*}\right) \tag{3.10}$$

where A_W is the Warburg coefficient, ω is the angular frequency of the excitation wave, j is the imaginary component, R is the gas constant, A is the surface area of the electrode, n is the number of electrons involved, D_O is the diffusion coefficient of the oxidant, D_R is the diffusion coefficient of the reductant, C_O^* is the oxidant concentration in bulk solution and C_R^* is the reductant concentration in bulk solution.

Z_W is an element with a constant phase of $-45°$ and is strongly dependent on the diffusion coefficients of the oxidant and reductant. A negligible Z_W is achieved for large diffusion coefficients while it tends to reach infinity for very small diffusion coefficients [149].

3.3 Measurement techniques

Different electrochemical measurement techniques are used for different kinds of electrochemical sensors. Below, typical measurement techniques are described to provide information regarding the design of sensors.

3.3.1 OCP measurement

For OCP measurement two electrodes, generally, a WE and a RE, are placed in electrical contact with an electrolyte. A potentiostat is connected to these two electrodes so that the intrinsic potential developed between the electrodes can be measured. This principle usually works for ion-selective sensors when the chemical reaction between the oxidant and reductant couple is not affected by other solvated ions in the solution. Under such circumstances, the measured potential E is given by the Nernst equation:

$$E = E_0 + \frac{RT}{nF}\ln\left(\frac{C_O}{C_R}\right) \tag{3.11}$$

where E_0 is the standard cell potential, C_O is the concentration of the oxidant and C_R is the concentration of the reductant. Therefore, the output OCP is proportional to the logarithm of the targeted ion concentration when keeping the other variable constant.

3.3.2 CA measurement

Chronoamperometry (CA) is an electrochemical measurement technique using three electrodes: the RE, CE and WE. In the presence of a REDOX species, when a single or stepped voltage, is applied between the RE and WE for a certain period, a current is generated which can be measured between the WE and CE due. By monitoring the characteristic of the output current against time, information relating to the analytes from the reaction can be distinguished. The measurement time can range from microseconds to hours depending on the application.

For a planar WE, the current produced in CA shows a transient period before the steady state, this current is given by the Cottrell equation [151]:

$$i = \frac{nFAC\sqrt{D}}{\sqrt{\pi t}} \tag{3.12}$$

Where i is the current, C is the concentration of the analyte, t is the time and A is the area of the WE.

This shows that the current is proportional to the concentration of the analyte if the diffusion profile is controlled at a given measurement time point. It increases versus the reciprocal of the square root of time and eventually reaches a steady state current. The amplitude of the steady state current for a micro-disc electrode I is given as:

$$I = 4nFDrC \tag{3.13}$$

where r is the radius of the electrode.

3.3.3 CV measurement

Cyclic voltammetry (CV) measures the current between a WE and CE by sweeping the applied voltage between the WE and RE in a three-electrode system. The potential is swept from one voltage towards a second voltage and then swept back to the original voltage with a pre-set scan rate and the number of cycles. It is a fundamental method for studying the characteristic of the chemical reaction including the reversibility and electron transfer kinetics [152], and for the determination of the diffusion coefficient and reduction potential of an analyte. With a redox reaction occurring at the WE, a

peak current (i_p) appears in the V-I plot given by the Randles-Sevcik equation:

$$i_p = 0.4463nFAC(\frac{nFvD}{RT})^{1/2} \tag{3.14}$$

where v is the scan rate.

For a reversible reaction (e.g. $[Fe(CN)_6]^{3-/4-}$), the CV shape is symmetrical and reversible against the middle voltage point, which depends on the RE and the reacting ions, with opposite peak currents.

For DO sensing, typical CVs from -0.6V to 0.9V are shown in Figure 3.3 representing the reactions on the Pt WE against a Pt CE and Ag/AgCl RE in PBS solution. At positive potentials, the platinum oxide is formed but quickly reduces in the backward sweep after entering the oxide reduction region. Typically, DO reduction on the Pt surface occurs at a threshold of 0.25V [153], the output current tends to be more negative along with a lower potential after the threshold. However, a valley is typically found to represent the saturation point of oxygen reduction. Afterwards, the current reverts towards the positive direction until hydrogen is absorbed on the surface at a more negative potential (e.g., at -0.6V) [154].
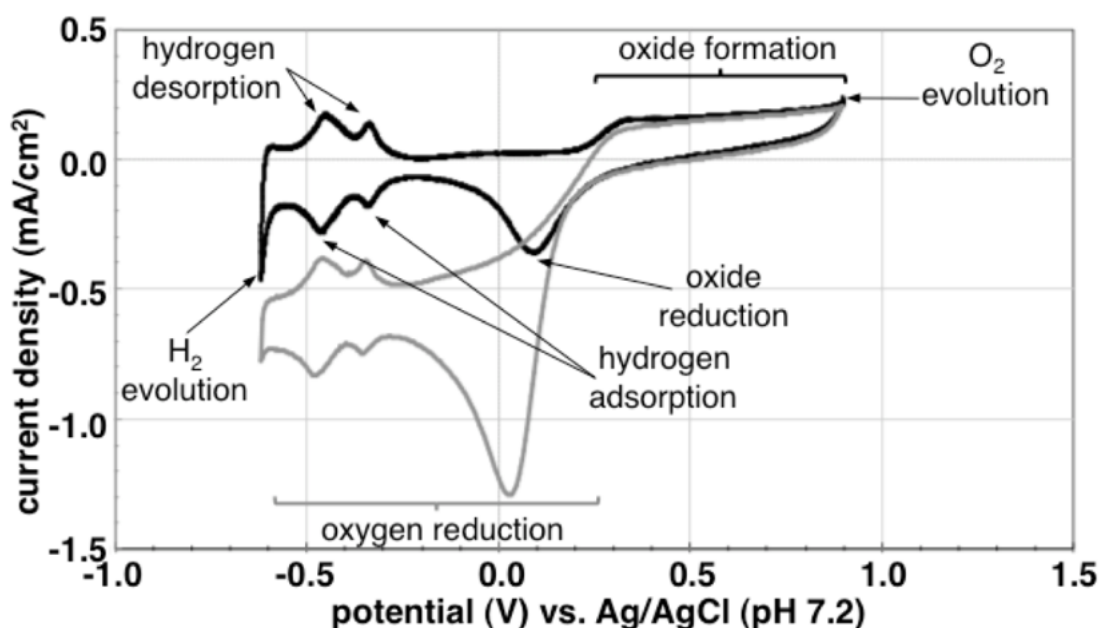
FIGURE 3.3: CVs (scan rate: 100 mV/s) of Pt in PBS (pH 7.2) under anaerobic condition (black line) and O_2 saturated condition (grey line) [153].

Chapter 4

Sensor fabrication and calibration

This chapter summarizes and discusses the progress, performance and limitations of the fabricated REs, pH sensors, DO sensors, conductivity sensors and ORP sensors.

4.1   Chip overview

Four types of chips, namely chips A, B, C and D, have been used to measure the four parameters (DO, pH, ORP and conductivity). The chips were designed and fabricated by Dr. Roel Mingels and Katie Chamberlain. The configurations of chips A, B, C and D are depicted in Figure 4.1. A, B, and C chips are double-sided while D chips are single-sided. A complete fabrication process can be found in [154]. Briefly, for all Pt electrodes, 200nm of Pt was sputtered onto borosilicate substrates with a thin Ti adhesion layer for all chips. The electrodes were patterned by ion milling. The RuO_x layer was then sputtered onto the Pt electrodes after a lift-off process. An insulation layer, (SU8) was deposited onto the Pt leads of the front side of A, B and C chips and etched to expose only the sensing electrodes and the contacts.

After microfabrication, all chips were left in acetone overnight to remove photoresist residue. The chips were then washed with ethanol and deionized (DI) water several times before examination with a microscope. Afterwards, unless specifically mentioned, enamelled copper wire (0.15mm OD, was soldered to the contacts of the chips. The solder joints were covered with black epoxy (RS PRO).

A chip (3.6 x 4.3 mm) consisting of four Pt ring electrodes was used for four-electrode conductivity sensing. A gold disc electrode (not used in this project) is on the front side, with two rectangular Pt electrodes on the backside. Chips B, C and D are 2.3 x 4.3 mm. The front side of chip C includes a thin Pt ring electrode for DO sensing, a RuO_x electrode for pH sensing and a larger Pt electrode for a CE. Chip B has a RuO_x electrode and a thin Pt ring electrode on the front side. The single-sided chip D, and the

back side of chips B and C, are shown in Figure 4.1e. They comprise two rectangular Pt electrodes. The difference between the back side of chips B & C and chip A is the separation between the two electrodes. The rectangular Pt electrodes on all four chips could be employed as the ORP sensor or the substrate for RE and Cl⁻ sensor.
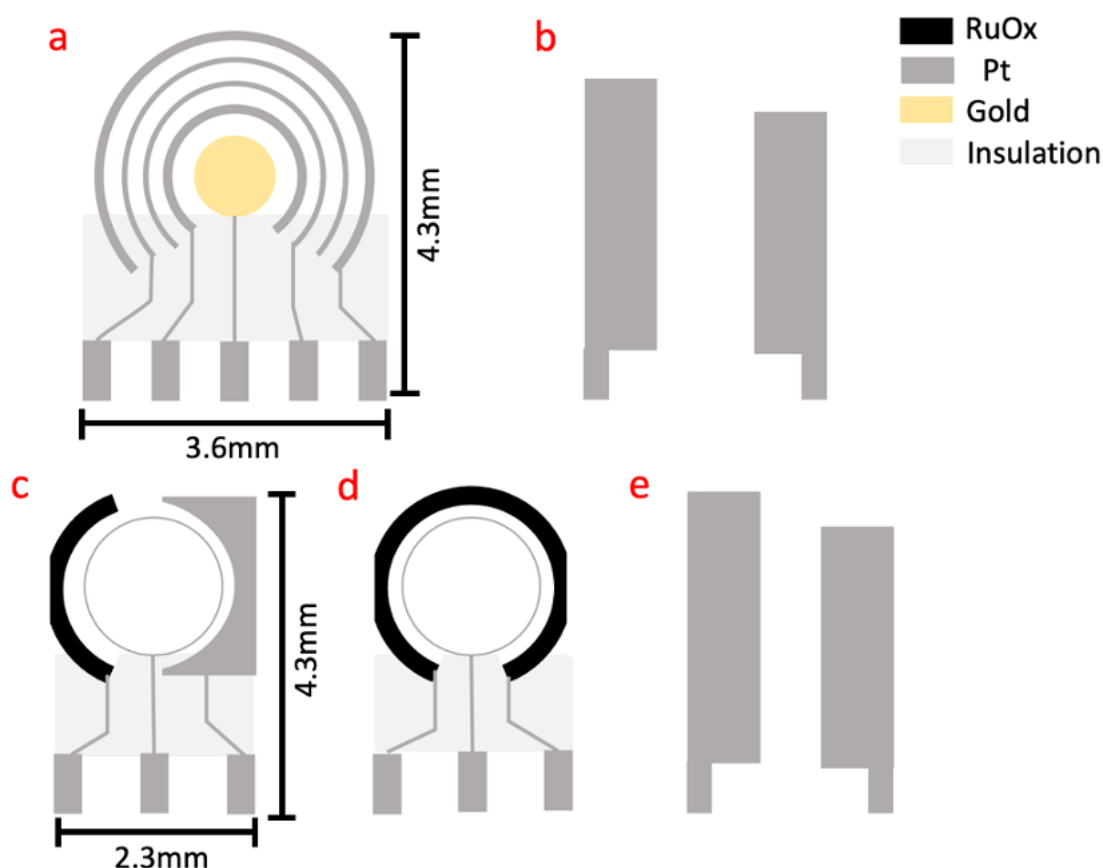
FIGURE 4.1: Configurations of four types of chips (A, B, C and D) used in this project. (a) front side of chip A; (b) back side of chip A; (c) front side of chip C; (d) front side of chip B; (e) back side of chips B and C, also the single-sided chip D.

Since chips A-D could only measure a maximum of 2 parameters at the same time, integrated chips with more versatile functionalities were proposed. Integrated chips were initially designed by Dr. Roel Mingels and improved by the author in terms of the final electrode arrangement for in vitro experiments. Two designs are illustrated in Figure 4.2a & b. Chip E was designed to monitor conductivity, ORP and pH with an on-chip RE while chip F could measure DO, ORP and pH. Chip E and F are larger in size, 7.5 x 7.5 mm. The contacts of chips E and F are wider to facilitate soldering and wire connection. For both designs, one or two spare Pt electrodes were included to enable sensing of other parameters in the future. The wafer was fabricated by Katie Chamberlain in the same way as discussed previously. All electrodes are recessed in an insulator so that anti-fouling membranes could be added.
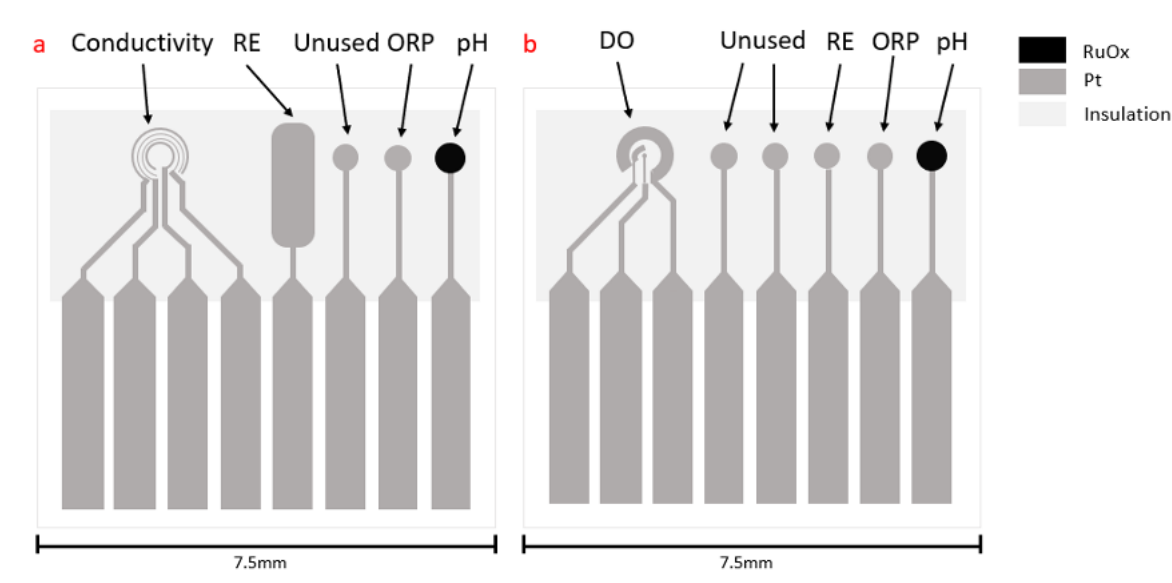
FIGURE 4.2: Configurations of integrated chips (a) E and (b) F, designed for in vitro study.

The capability of each chip configuration and actual sensors used in measurements detailed in later sections are concluded in Table 4.1.

Chip	Sensing capability	Sensors used
A	Conductivity, RE (Cl⁻) & ORP	Conductivity & Cl⁻
B	DO, pH, RE (Cl⁻) & ORP	DO & RE
C	pH, RE (Cl⁻) & ORP	pH, RE & Cl⁻
D	RE (Cl⁻) & ORP	RE & Cl⁻
E	Conductivity, pH, RE (Cl⁻) & ORP	Conductivity & Cl⁻
F	DO, pH, RE (Cl⁻) & ORP	pH & Cl⁻

TABLE 4.1: Summary of the functionality of each chip configuration.

4.2   Reference Electrode (RE)

4.2.1   Fabrication and measurement method

A QRE is a special type of RE. Ideally, any electrode can be regarded as a QRE as long as it possesses a stable potential in the measuring environment under strict conditions, such as no ion concentration variation. A pure Ag/AgCl QRE, which is also a Cl⁻ sensor, can provide a constant potential where the Cl⁻ concentration is constant in the electrolyte. Two types of QREs (Type 1 and 2) were fabricated based on Pt electrodes, on chips D or the back side of chips B and C (Figure 4.1e).

Prior to the deposition of black epoxy insulation, as described in Chapter 4.1, a type 1 QRE was fabricated by screen-printing Ag/AgCl paste (Sigma Aldrich, UK) onto the Pt electrode. The sensor chips were placed in a PDMS mold (Figure 4.3b) fabricated from a polymethyl methacrylate PMMA substrate (Figure 4.3a) by laser cutting. All Pt contacts were covered with tape before Ag/AgCl deposition. The Ag/AgCl paste was brushed onto the chips twice to ensure that the Pt electrodes and Pt edges of the chips were fully covered (Figure 4.3c). Immediately after deposition, the PDMS mold containing chip D was cured in an oven at 60°C for at least 4 hours to evaporate solvents in the paste. Subsequently, the Ag/AgCl layer was polished using fine sandpaper to obtain a uniform coating.

For Type 2 QRE the fabrication consisted of two steps, namely Ag electroplating and electro-chloridisation. The Ag electroplating procedure plated a Ag layer onto the Pt electrode using a commercial Ag plating solution (Spa Plating, UK). This was done by running chronopotentiometry using a PalmSens 4 potentiostat with a current of -10mA/cm^2 for 10 mins against an Ag wire (0.0125mm diameter), giving a bright silver layer on the target electrode. Subsequently, the Ag layer was converted to Ag/AgCl using chronopotentiometry versus a thin Pt sheet in 3M KCl solution with a current of 0.5mA/cm^2 for 800s giving a dark brown Ag/AgCl electrode.

In order to fabricate the Ag/AgCl REs with the fast-cure epoxy membrane (FE-REs), single-sided chips D were used. The design and fabricated RE are shown in Figure 4.4. After the deposition of Ag/AgCl paste and black epoxy insulation (Type 2 QRE), each RE was further protected by a pipette that was backfilled with black epoxy, leaving only the active electrode area exposed. Each sensor chip was immediately inserted into a homemade PDMS mold pre-filled with the salt matrix (Figure 4.4b). The sensor was manually held to maintain a correct position in the mold for at least 5 mins. In this way the thickness of the reference membrane on each side was 0.7-0.9mm. The Ag/AgCl sensor chip was tightly enclosed by the salt matrix after 5 mins and the chip was left to completely cure for 24 hours. The salt matrix was constructed by mixing thinned fast-cure epoxy (Araldite Rapid) with 33w/w% or 50w/w% KCl powder. Fast-cure epoxy was thinned using 10 w/w% acetone.
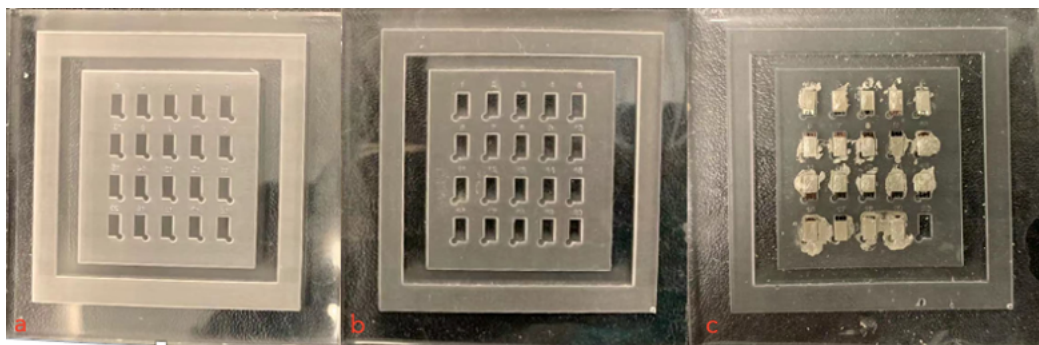
FIGURE 4.3: A PMMA substrate (a) was fabricated by laser cutting. The PDMS mold (b) was cast using the substrate. Chips D were placed inside the hollows and the contacts were covered by tape. (c) Ag/AgCl paste was brushed onto the mold and cured for at least 4 hours in an oven to ensure that the edges of the chips were fully covered except for the contact.

Three Type 1 QREs (Ag/AgCl-P1 - Ag/AgCl-P3) and three Type 2 QREs (Ag/AgCl-E1 - Ag/AgCl-E3) were fabricated. Four FE-REs containing 33w/w% KCl (33%KCl-A – 33%KCl-D) and 50w/w% KCl (50%KCl-A – 50%KCl-D) were also made. A Ag/AgCl wire was used as a control electrode for the FE-REs. Before any measurements, all REs were conditioned in 0.1M KCl overnight to hydrate the REs. The Cl^- sensitivity for all REs was measured using beakers placed in a water bath at 37°C. A stability test was done using the same setup. The potential of each RE was measured using a NI-USB-6211 multifunction I/O device and a commercial DJRE. The sensors and the DJRE were placed into the beaker, ensuring that only the sensor heads were fully immersed. For Cl^- sensitivity tests, a calibration was conducted with 0.01M KCl, 0.1M KCl and 1M KCl solutions. The sensors were rinsed with DI water and wiped dry between each solution. The potentials of the chips were measured every 1s for at least 60mins in each solution. Each data point in the sensitivity plot was the average potential over the last 10mins (600 points) of the measurement. For the long-term stability test, the potentials were collected every 10s and each data point in the long-term stability plot is the average potential for 30mins (180 points). Type 1 QREs were immersed in 0.1M KCl solution for 13 days (Day 0 to Day 13) and measured continuously with the potentiostat. On Day 9 another Cl^- calibration was made to determine the functionality of Type 1 QREs after 9 days. Type 2 QREs were immersed for 2 days while the long-term stability of FE-REs was measured over 7 days.

4.2.2 Results and discussion

The Cl^- sensitivity test for Type 1 QRE is plotted on Day 0 and Day 9 in Figure 4.5a & b, and summarized in Table 4.2. A near-Nernstian sensitivity was achieved at the beginning or after immersion for 9 days, with -55.58mV/dec and -55.30mV/dec respectively. Low variations were observed between the 3 sensors, showing good reproducibility. Since the voltage between QRE and DJRE (filled with 3M KCl) should reach zero with
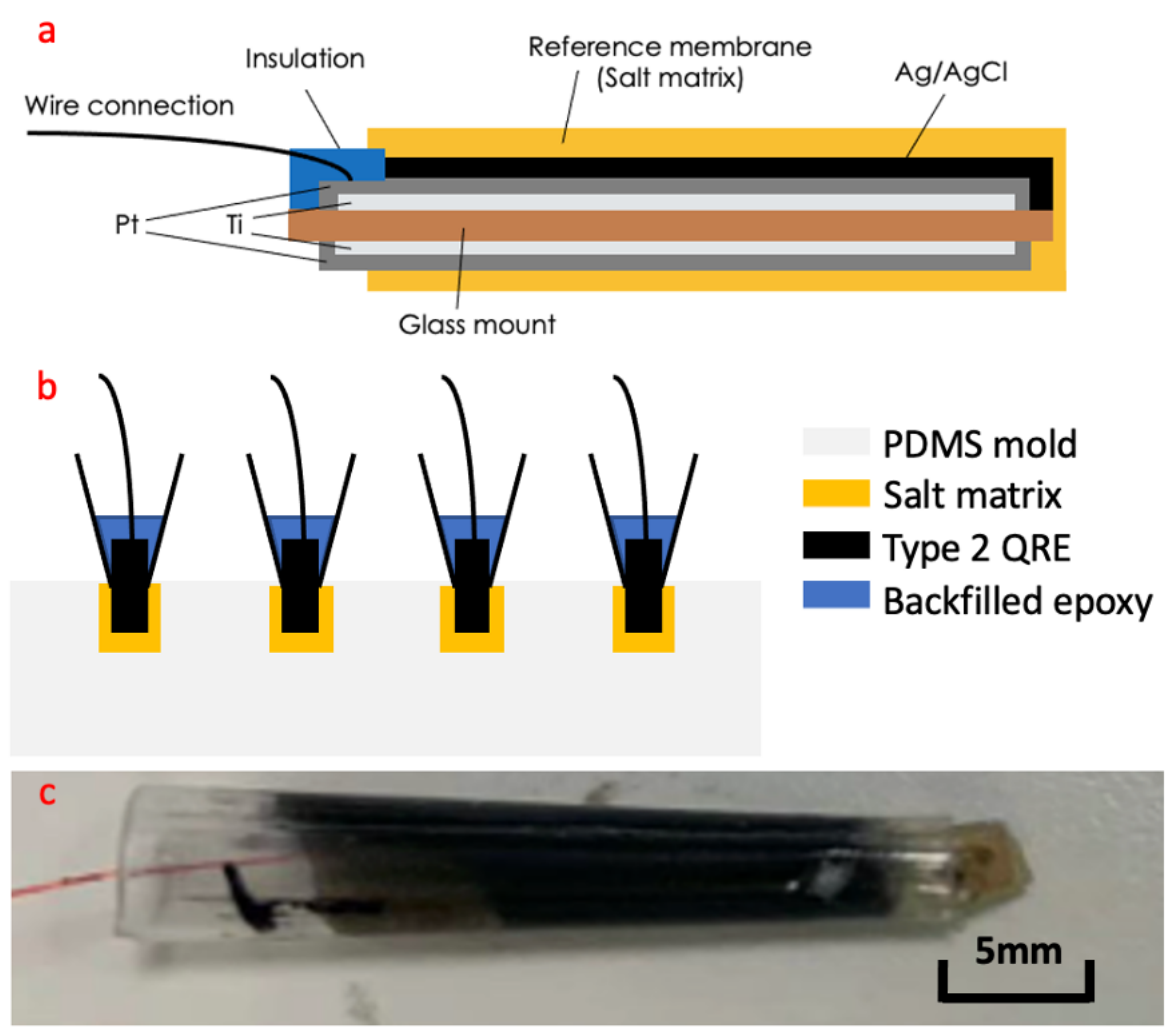
FIGURE 4.4: (a) Design, (b) salt deposition demonstration and (c) photograph of a fabricated RE.

both immersed in 3M KCl solution, a theoretical estimate was made of the intercept (voltage on 1M KCl solution) assuming a Nernstian sensitivity of -61.5mV/dec (equation (4.1)) at 37°C.

$$Intercept = (\log(1) - \log(3)) \times (-61.5)mV = 29.34mV \tag{4.1}$$

Compared to the actual intercepts which ranged between 26.92-27.60mV, a slight discrepancy (<2.5mV) is observed demonstrating a good match. The response time of Type 1 QREs was a maximum of 15 minutes after switching solutions.

The long-term performance of Type 1 QREs was recorded over 13 days as shown in Figure 4.5c. Three QREs exhibited similar response despite tiny voltage differences (<1mV). A total voltage drop of approximately 4mV was found for the first four days due to slight evaporation of water, leading to a higher Cl⁻ concentration within the
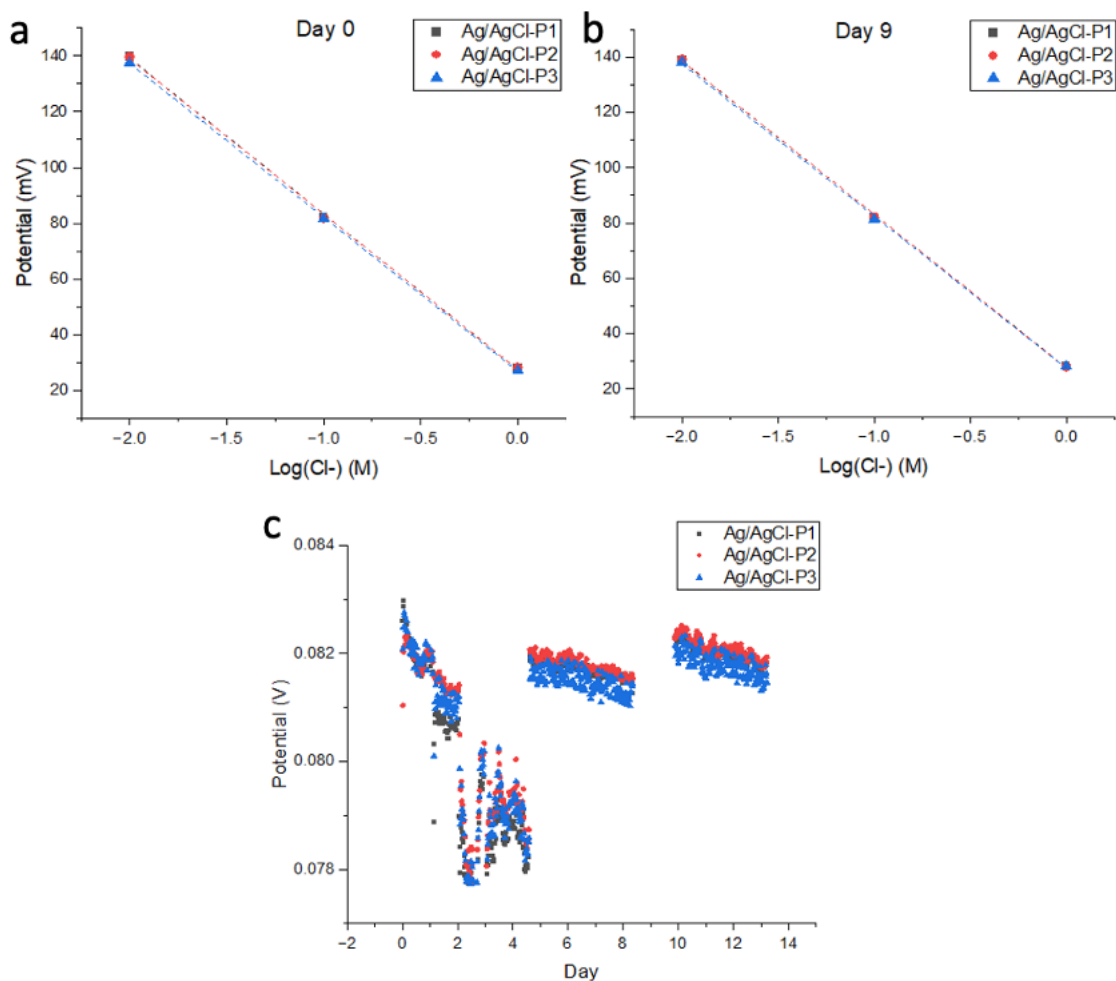
FIGURE 4.5: Results for Type 1 QREs showing (a) Cl⁻ sensitivity test at Day 0, (b) Cl⁻ sensitivity test at Day 9, and (c) long-term stability test over 13 days. Near Nernstian response was seen for all Type 1 QREs with excellent long-term stability.

beaker. The DI water was refilled to the same level as at Day 0 at the start of Day 5, triggering a voltage jump in 3 QREs. Afterwards, the water was constantly replenished to avoid further voltage deviation from evaporation. On Day 9, the QREs were removed for Cl⁻ sensitivity tests, leaving a blank section on the plot. Overall, it was concluded that no obvious potential drift occurred over 13 days for Type 1 QRE. It further proved that with this fabrication method the Ag/AgCl layer was successfully deposited onto the Pt substrate and the Ag/AgCl chips could potentially be used as Cl⁻ sensors for at least 13 days continuous monitoring.

In a similar manner, the Cl⁻ sensitivity of Type 2 QRE was tested, followed by long-term stability measurement over 2 days, as shown in Figure 4.6. The fit results from the sensitivity test are listed in Table 4.3.

Linear responses with $R^2 > 0.999$ were found with an average Cl⁻ sensitivity of -54.72 mV/dec. The intercept values were close to the theoretical calculation (equation (4.1)),

Day	Sample	Intercept (mV)	Sensitivity (mV/dec)	R^2	Mean sensitivity (mV/dec)	STD (mV/dec)
0	Ag/AgCl-P1	27.50	-55.84	0.999	-55.58	0.35
	Ag/AgCl-P2	27.54	-55.71	0.999		
	Ag/AgCl-P3	26.92	-55.18	0.999		
9	Ag/AgCl-P1	27.71	-55.40	0.999	-55.30	0.28
	Ag/AgCl-P2	27.60	-55.52	0.999		
	Ag/AgCl-P3	27.47	-54.99	0.999		

TABLE 4.2: Summary of fitting results during Cl⁻ sensitivity test for Type 1 QREs at Day 0 and 9.

and the response time of Type 2 QRE was less than 30s. During 2 days of measurement, a small drift of approximately 1mV/day was observed, possibly due to water evaporation.
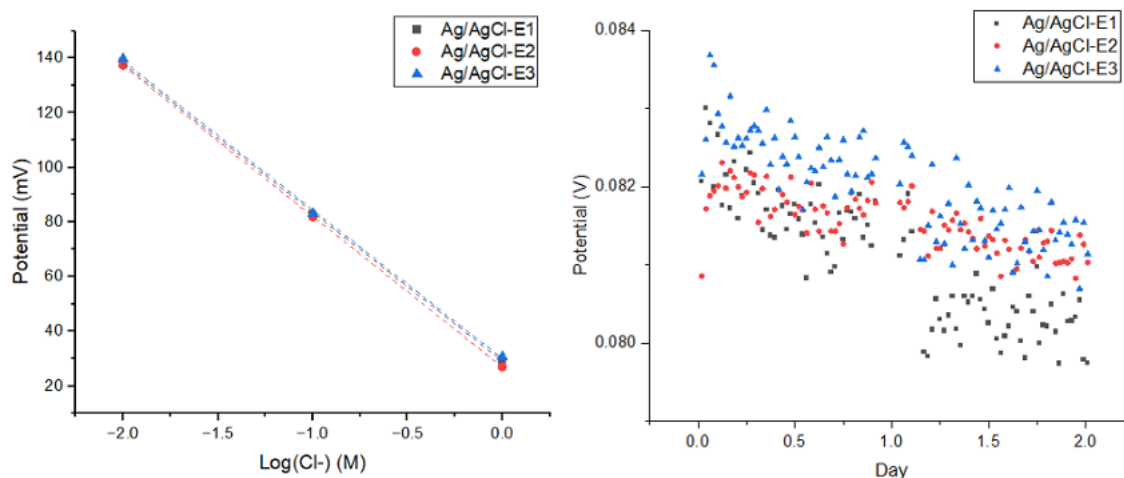
FIGURE 4.6: Measurement of Type 2 QREs including (a) Cl⁻ sensitivity test and (b) long-term stability test over 2 days.

During laboratory tests, both types of QREs showed excellent behaviour with the QREs suitable for in vitro experiments in rumen fluid. Type 1 QRE had a longer response time but better sensitivity and long-term stability. Although the long-term stability measurement was only conducted for 2 days for Type 2 QREs, it was still worthwhile to examine the performance of Type 2 QRE but over a shorter time scale.

Sample	Intercept (mV)	Sensitivity (mV/dec)	R^2	Mean (mV/dec)	STD (mV/dec)
Ag/AgCl-E1	29.04	-54.49	0.999		
Ag/AgCl-E2	26.87	-55.18	0.999	-54.72	0.40
Ag/AgCl-E3	29.93	-54.49	0.999		

TABLE 4.3: Summary of fitting results for Cl⁻ sensitivity test for Type 2 QREs
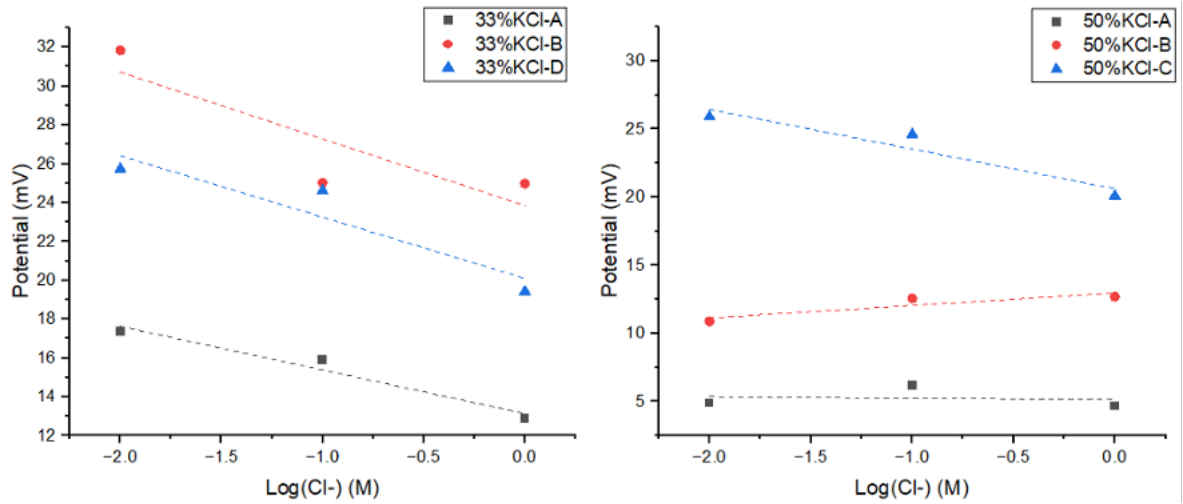
FIGURE 4.7: Cl⁻ sensitivity plots for the epoxy QRE for 33%KCl and 50%KCl at Day 0. Linear fits of the output potential versus the logarithm of Cl⁻ concentration for each RE is illustrated by the dotted line. 33%KCl chip C and 50%KCl chip D suffered insulation failure during hydration and hence did not appear on the sensitivity test.

Sample	Intercept (mV)	Sensitivity (mV/dec)	R^2	Mean (mV/dec)	STD (mV/dec)
33%KCl-A	13.14	-2.24	0.96		
33%KCl-B	23.85	-3.43	0.75	-2.95	0.62
33%KCl-D	20.10	-3.16	0.88		
50%KCl-A	5.14	-0.11	0.02		
50%KCl-B	12.97	0.91	0.81	-0.70	1.98
50%KCl-C	22.63	-2.91	0.91		

TABLE 4.4: Cl⁻ sensitivity results on Day 0. The mean sensitivity for the 50%KCl group (-0.7mV/dec) was lower than the 33%KCl group (-2.95mV/dec) due to the higher amount of Cl⁻ within the epoxy matrix.

The Cl⁻ sensitivity test for the fast-cure epoxy-based REs was performed on Day 0; results in Figure 4.7. Linear fits of the potential versus the logarithm of Cl⁻ concentration

for each RE is shown by the dotted line. Calibration results are summarised in Table 4.4.

At Day 0, the Cl$^-$ sensitivities of both 33%KCl and 50%KCl groups were below 3.5mV/dec. The mean sensitivity for the 50%KCl group (-0.7mV/dec) was lower than the 33%KCl group (-2.95mV/dec) due to the higher amount of Cl$^-$ within the epoxy matrix. Although ideally a RE should have no Cl$^-$ sensitivity, the small sensitivities for both groups on Day 0 were adequate for general sensing applications where the Cl$^-$ concentration change was small.
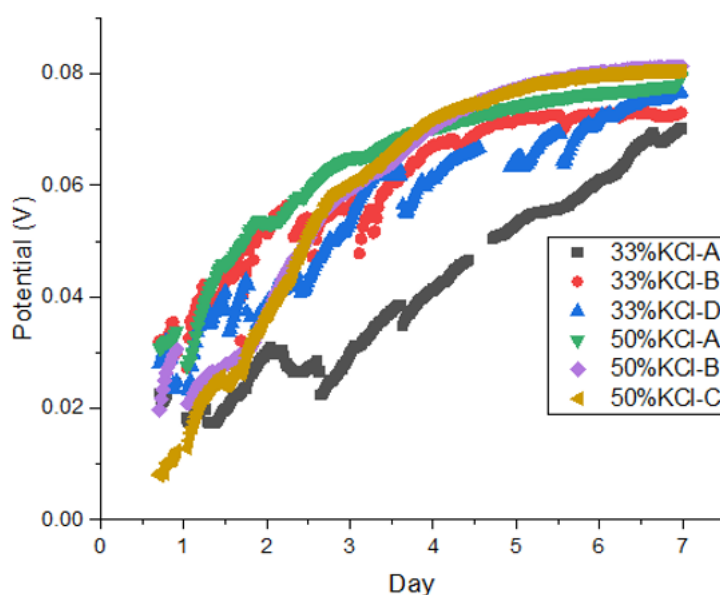
FIGURE 4.8: Long-term stability test for FE-REs and the control group. All FE-REs exhibited a rapid decay before Day 6.

Sample	Intercept (mV)	Drift (mV/day)	R^2	Mean drift (mV/day)	STD (mV/day)
33%KCl-A	9.97	7.72	0.89		
33%KCl-B	29.23	8.97	0.92	9.03	1.35
33%KCl-D	20.51	10.41	0.92		
50%KCl-A	30.05	10.09	0.90		
50%KCl-B	10.04	14.79	0.96	13.94	3.5
50%KCl-C	2.8	16.94	0.95		

TABLE 4.5: Summary of the drift of 33%KCl and 50%KCl groups of REs from Day 0.5 to Day 5. The rapid drift prevented the FE-REs from long-term monitoring.

After immersion for 7 days, both groups showed considerable potential drift, meaning that the FE-REs failed and were not suitable for long-term usage. The data traces of the REs during the long-term stability test are in Figure 4.8. All REs exhibited rapid drift,

especially before Day 6. Linear fits were performed for the drift, summarized in Table 4.5. It was clear that the rapid drift (9.03mV/day for 33%KCl group and 13.94mV/day for 50%KCl group) meant that these FE-REs were unsuitable for long-term monitoring.

The reason for the high drift was that the KCl in the epoxy matrix leaked into the solution due to the porous structure. The 50%KCl group had a quicker leakage and higher drift owing to its higher KCl composition for a solid-state membrane [43]. The Ag/AgCl wire behaved well as the control QRE and had negligible drift.

In summary, although both types of QREs could be considered for rumen monitoring, Type 2 QREs were preferable due to better long-term stability and low drift. FE-REs were not suitable for long-term usage resulted from rapid Cl⁻ leakage and in turn high drift.

4.3 pH sensor

4.3.1 Fabrication and measurement method

Chips C were used for laboratory testing of pH sensors. The chips were insulated as described in Chapter 4.1. For every chip one of the back-side Pt electrodes was converted to Ag/AgCl QRE to serve as an internal RE for pH measurement.

All sensor chips were conditioned in DI water for at least 1 day to hydrate the RuO_x film. pH calibrations were performed at room temperature ($22 \pm 2°C$) in PBS solution. 150mL PBS solution was aliquoted to three beakers (50mL per beaker). The pH of the PBS solution in each beaker was adjusted to 6.5, 7.5 and 8.5 respectively by the addition of 1M hydrochloric acid (HCl) solution or 1M sodium hydroxide (NaOH) solution. Reference pH readings were made with a commercial pH meter (Jenway 3510, UK). 8 sensors were sterilized using ethylene oxide (ETO) by Anderson Caledonia Ltd in order to compare the sensor responses before and after sterilization as a prerequisite for in vivo applications. ETO sterilization uses ethylene oxide to sterilize healthcare devices and kill microorganisms left during production or packaging processes. It is a low-temperature process ($37 - 63°C$).

During pH calibration, the RuO_x electrode acted as the pH sensing electrode measured against the internal RE. OCP measurements were recorded using NI-6211 and LabView with a voltage measurement made every 1s. A maximum of 8 sensors could be measured simultaneously for at least 30 mins. The data was recorded as the average output potential of the last 10mins (600 points) for each solution.
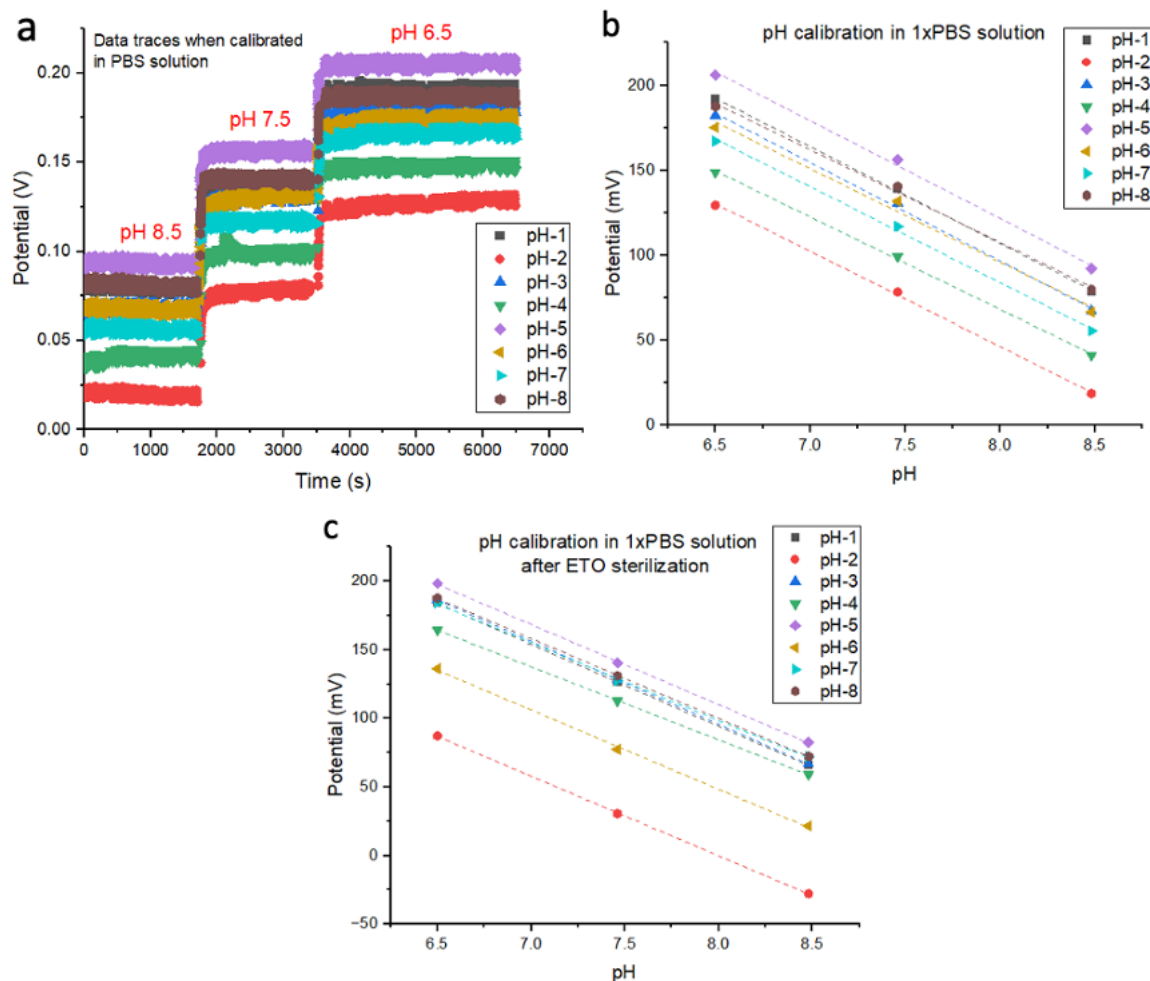
FIGURE 4.9: (a) Data traces for the output voltage of 8 sensors in PBS at pH 6.5, 7.5 and 8.5. The STDs of voltages from the last 10mins in each solution were below 5mV. The plots are before (b) and after (c) ETO sterilization, for a total of 8 pH sensors (pH-1 to pH-8).

4.3.2   Results and discussion

The pH calibration results before and after ETO sterilization, for a total of 8 pH sensors (pH-1 to pH-8) are shown in Figure 4.9b-c. Linear fittings were made with Origin 9.1 for all sensors. Example data traces of output voltages during calibration are shown in Figure 4.9a. The standard deviations (STDs) of voltages from the last 10mins were below 5mV. The pH sensitivities of the sensors before and after ETO sterilization are summarized in Table 4.6 and 4.7.

All 8 sensors showed near-Nernstian responses before (-56.1$\pm$1.3 mV/pH) and after (-57.8$\pm$2 mV/pH) ETO sterilization, but with a variation in offset voltage (<30mV). The pH sensitivities were comparable to other reported RuO_x pH sensors (sensitivities between 55-59mV/pH) [95, 98, 99]. The response time for pH sensors to reach 90% of steady state value after switching to a new pH solution was less than 2 minutes.

Sensor	Intercept (mV)	Sensitivity (mV/pH)	Mean sensitivity (mV/pH)	STD (mV/pH)
pH-1	563.0	-57.0		
pH-2	494.4	-56.0		
pH-3	560.6	-58.0		
pH-4	503.3	-54.4	-56.1	1.3
pH-5	581.6	-57.5		
pH-6	535.4	-54.9		
pH-7	535.2	-56.4		
pH-8	543.6	-54.5		

TABLE 4.6: The sensitivities of the pH sensors based on a linear fitting with R^2>0.999. All 8 pH sensors showed near-Nernstian responses prior to ETO sterilization between pH 6.5 to 8.5 (-56.1±1.3 mV/pH)

Sensor	Intercept (mV)	Sensitivity (mV/pH)	Mean sensitivity (mV/pH)	STD (mV/pH)
pH-1	571.3	-59.6		
pH-2	464.2	-58.0		
pH-3	579.9	-60.5		
pH-4	510.4	-53.3	-57.8	2.0
pH-5	577.5	-58.4		
pH-6	511.2	-57.9		
pH-7	551.7	-56.7		
pH-8	565.8	-58.2		

TABLE 4.7: Sensitivities of the pH sensors with R^2>0.999. All 8 pH sensors showed near-Nernstian responses after ETO sterilization between pH 6.5 to 8.5 (-57.8±2.0 mV/pH).

In conclusion, the pH sensors were suitable for detection over the range of pH 6.5-8.5. It was anticipated that the sensors would show good accuracies as long as a pre-calibration was performed prior to the measurement.

4.4   DO sensor

4.4.1   Fabrication and measurement method

DO measurements were performed using chips C where the ring Pt electrode (WE) and the large Pt electrode (CE) at the front side, together with a fabricated back-side internal QRE, constituted the complete electrochemical DO sensor. The outer and inner radius of the WE were 647µm and 624µm respectively, giving an electrode area of $0.093mm^2$. The area of the CE should be at least 10 times bigger than the area of WE in order to have a low impedance. Three to five successive CVs (-1 to 1V, scan rate: 50mV/s, scan step: 5mV) were run for the WEs of all DO sensors to clean the Pt surface and check the capability of the ring electrode for DO sensing.

The sensors were left in PBS solution for at least 8h before calibration. The calibration procedure was as follows: a commercial optical DO probe (ProODO, YSI, UK) was inserted into a 100mL borosilicate glass bottle containing 50mL PBS and a magnetic flea. The glass bottle was positioned on a magnetic stirrer (Hanna Instrument, UK) to stir the solution at the lowest speed. A maximum of 4 homemade DO sensors were stuck to the probe with waterproof tape to ensure that the DO sensors were very close to the probe. The solution was bubbled with N_2 for at least 30mins until the DO probe reading was less than 0.8mg/L. The glass bottle was then tightly covered with Parafilm except for a small hole to let oxygen gradually dissolve into the solution.

CA measurements were made with PalmSens 3 and 8 multiplexers for 0.2s with an interval of 5ms. A measurement script was set up in PSTrace 5.8 to make a CA measurement for each sensor every 6 mins until the DOC was equal to the atmospheric oxygen concentration (around 8.2mg/L). In addition, the DO probe was programmed to record a reference DO reading immediately when the potentiostat took CA measurements.

4.4.2   Results and discussion

CVs were run for the WEs of all DO sensors to clean the Pt surface by removing oxide or chemical residues and check the capability of the Pt electrode for DO sensing. Typical CVs for the Pt ring DO sensor in PBS for 4 different DOCs are in Figure 4.10. The sensor was able to distinguish a variety of DOC states. Oxygen reduction occurred when sweeping towards -1V and a voltage <0.2V. A plateau was found for oxygen reduction between -0.3V to -0.6V, implying a steady-state response within the range. Thus a voltage of -0.5V was selected as the polarization voltage for the CA measurements. Referring to Figure 3.3, an oxygen reduction peak was commonly depicted on the CV graph. However, the fact that the oxygen reduction peak was not obvious when measuring with developed DO microelectrodes was due to the rapid replenishment of

active species diminishing the diffusion limitation, especially under stirring environment.
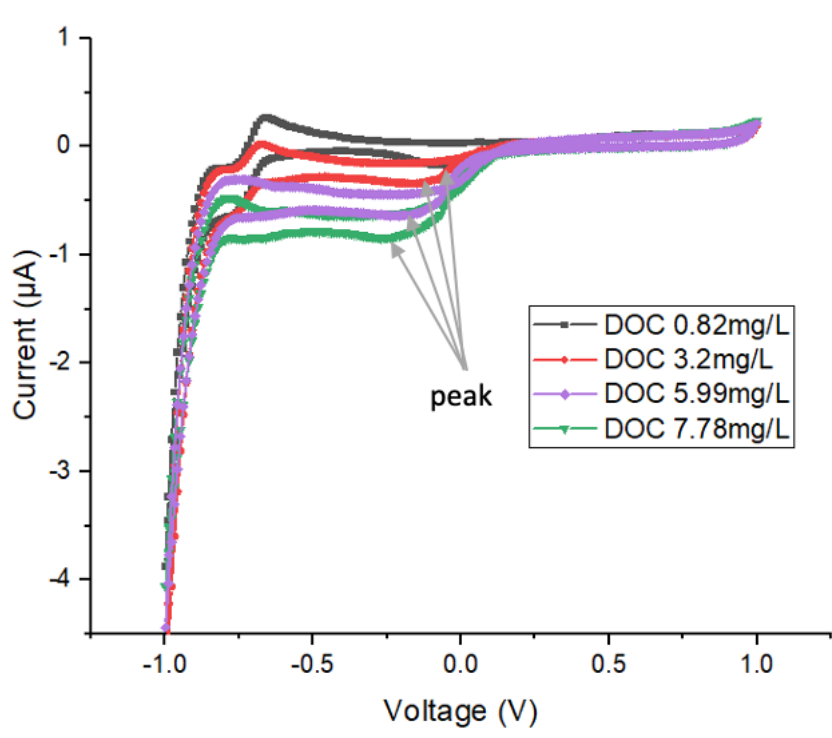
FIGURE 4.10: CVs for the DO sensor in PBS at 4 different DOCs (0.82mg/L, 3.2mg/L, 5.99mg/L and 7.78mg/L). The sensor could measure different DOC through the output current change. A plateau was found for oxygen reduction between -0.3V to -0.6V.

According to the Cottrell equation, the output CA current should be proportional to the DOC. The complete DO analysis process is illustrated in Figure 4-11 using sensor DO-1 in PBS. All CA curves over the entire measurement period are displayed in Figure 4.11a. Five time points (at 15ms, 30ms, 50ms, 75ms and 100ms) were selected for calibration. The output current for all CA measurements at each time point was plotted against the DOC measured by the probe (Figure 4.11b). Linear fittings were made in the region of DOC 1-1.5 mg/L to DOC 7.5-8 mg/L. The linear fit region was selected since deviations appeared at both low DOC (<1mg/L) and high DOC (>8mg/L). The reasons are discussed later in this chapter. The output current in the linear range was converted to the measured DOCs at each time point (Figure 4.11c). Finally, the 5 measured DOCs at the same DO probe reading were averaged to calculate the overall measured DO as shown in Figure 4.11d. The differences between the measured DO and the DO probe for all data points in the linear part were averaged, with the error and the STD of the average giving accuracy of the DO sensor within the linear detection range.

The fitting results for all 8 sensors (DO-1 to DO-8) are summarized in Table 4.8, with $R^2 > 0.99$ for all fits. It was seen that excellent linearities were achieved with a maximum mean error of 0.12mg/L, meaning that the accuracy of the DO sensors was better than ±1.7% over the measurement range of 1-8mg/L. Since a linear response typically
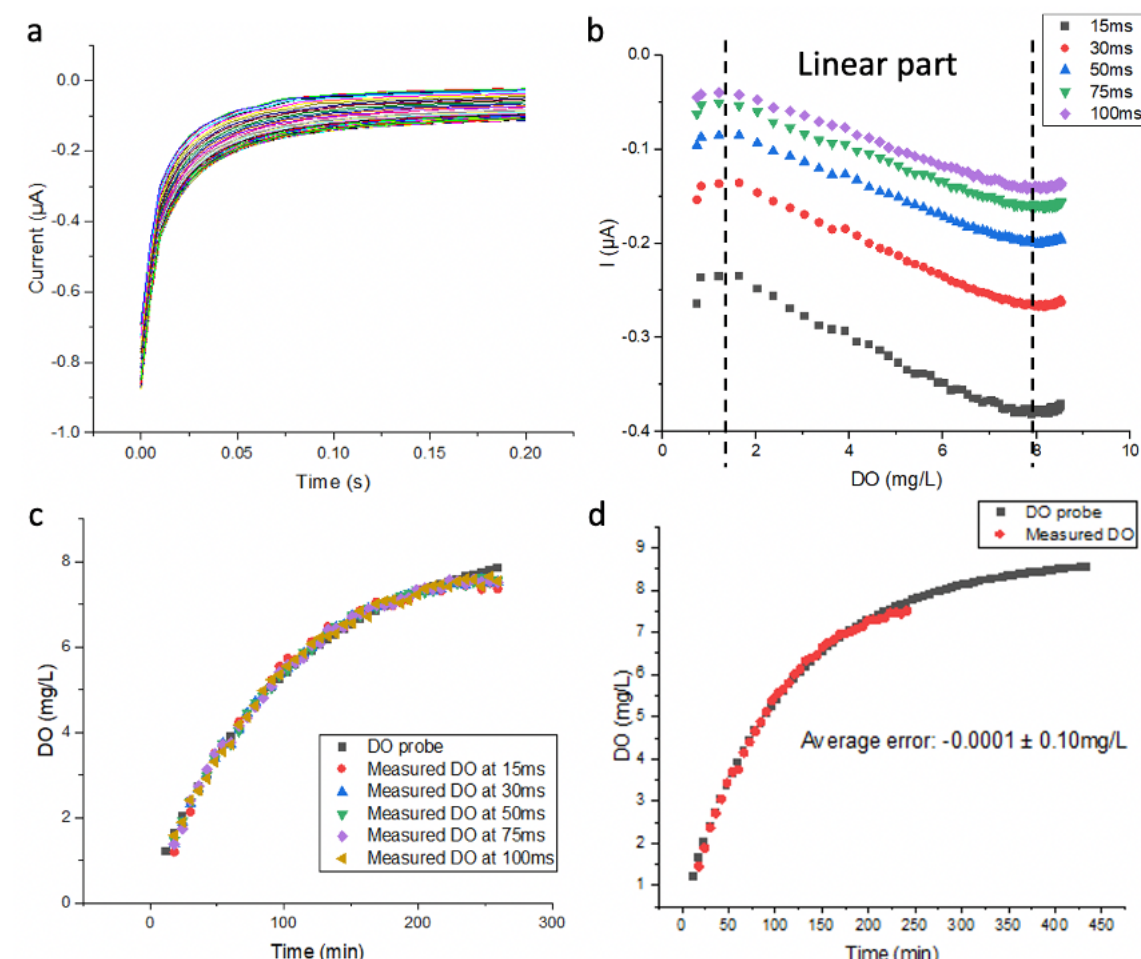
FIGURE 4.11: Analysis process for DO calibration in PBS using sensor DO-1 as an example. (a) All CA curves over the entire measurement period. (b) 5 time points among the 200ms selected, (15ms, 30ms, 50ms, 80ms and 100ms) for calibration. The output current for all CA measurements at each time point was plotted against the DOCs measured by the optical probe. (c) The output current in the linear range was converted to the measured DOCs at each time point based on a linear fit. (d) The 5 measured DOCs at the same DO probe reading were averaged to calculate the overall measured DO.

occurred above 1mg/L, the LOD of the developed DO sensor was 1 mg/L. The deviation for low DOC was attributed to the lack of DO equilibrium within the solution as soon as the N_2 supply was removed, as well as the lower accuracy of the optical DO probe.

Sensor	Time point	Slope (nA/mg/L)	Intercept (nA)	Mean error (mg/L)	Error STD (mg/L)
	15ms	-23.51	-204.77		
	30ms	-21.32	-104.82		
DO-1	50ms	-18.8	-56.54	0.1	0.07
	75ms	-17.42	-28.87		
	100ms	-16.71	-14.97		

	15ms	-18.99	-68.26		
	30ms	-18.57	-36.12		
DO-2	50ms	-18.96	-15.65	0.12	0.07
	75ms	-18.42	-7.39		
	100ms	-17.88	-4.01		
	15ms	-14.63	-103.14		
	30ms	-14.1	-64.75		
DO-3	50ms	-13.99	-40.69	0.08	0.05
	75ms	-13.89	-25.19		
	100ms	-13.55	-17.78		
	15ms	-26.79	-34.62		
	30ms	-25.64	-6.58		
DO-4	50ms	-25.15	7.33	0.06	0.05
	75ms	-24.16	11.38		
	100ms	-23.58	14.29		
	15ms	-22.69	-93.61		
	30ms	-22.63	-47.82		
DO-5	50ms	-22.76	-23.03	0.12	0.08
	75ms	-22.69	-9.87		
	100ms	-22.25	-4.93		
	15ms	-15.63	-136.86		
	30ms	-16.45	-77.46		
DO-6	50ms	-17.37	-47.57	0.08	0.07
	75ms	-18.44	-29.32		
	100ms	-19.09	-20.37		
	15ms	-13.25	-82.54		
	30ms	-12.74	-47.48		
DO-7	50ms	-13.65	-22.06	0.11	0.09
	75ms	-13.57	-10.83		
	100ms	-13.41	-6.19		
	15ms	-91.21	-20.43		
	30ms	-87.29	24.97		
DO-8	50ms	-83.69	46.12	0.06	0.04
	75ms	-80.11	55.2		
	100ms	-77.19	58.71		

TABLE 4.8: Fit results for all 8 DO sensors (DO-1 to DO-8), R^2>0.99.

A decrease in current when the DOC was near saturation was measured for every sensor. This effect might be due to the equilibration time of the DO electrode and the surrounding solution. (Figure 4.11b).

The same effect was reported by Stine et al. for a DO sensor used for bioprocess monitoring and the effect could be reduced by applying a linear fitting for the current drift [155].
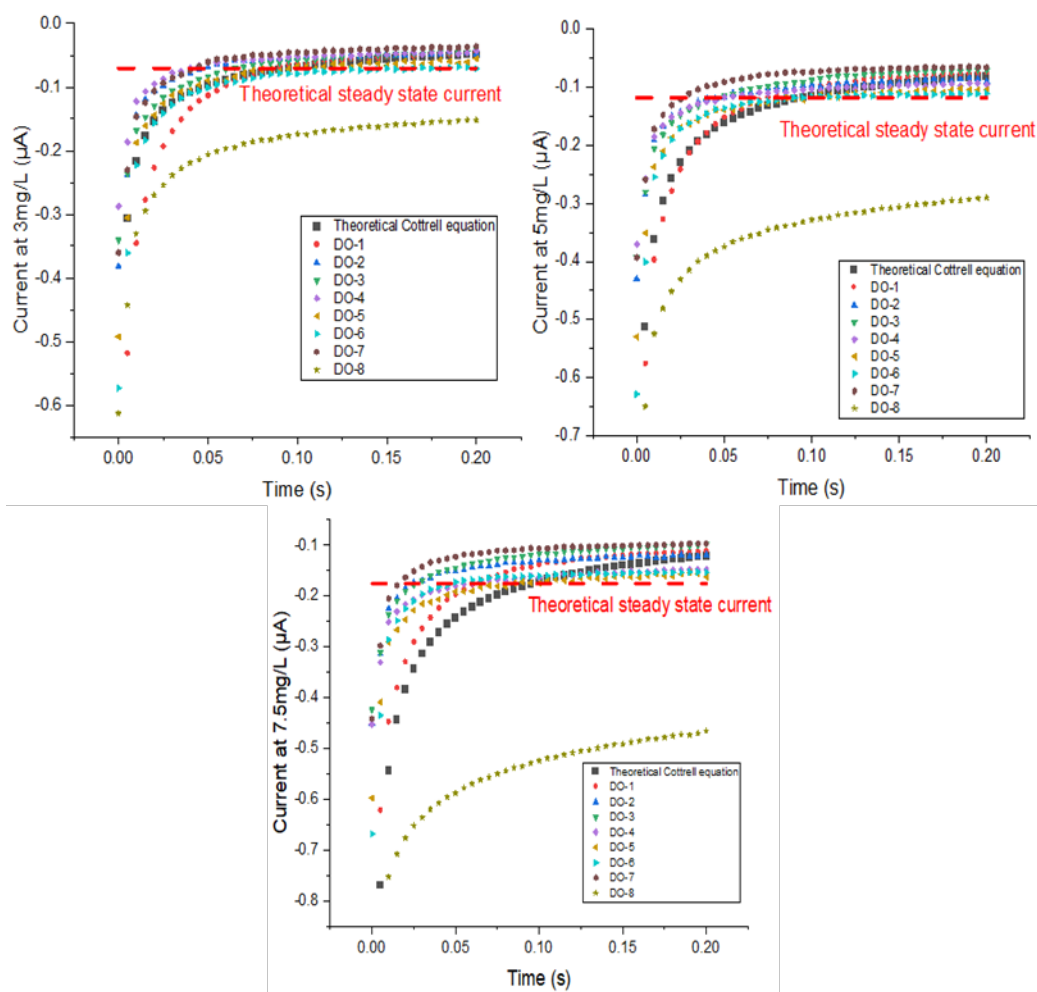
FIGURE 4.12: Theoretical behaviour of the DO sensors at three DOCs (3mg/L, 5mg/L and 7.5mg/L). The transient response was estimated based on the Cottrell Equation. The theoretical steady state current for the DO sensor was calculated through the formula developed for the ring electrode.

The theoretical behaviour of the DO sensors at three DOCs was plotted against the actual responses of 8 sensors in Figure 4.12 at 3mg/L, 5mg/L and 7.5mg/L. The transient response was estimated based on the Cottrell equation (3.13) where A=9.29*10^{-8} m^2, D=2.1*10^{-9} m^2/s. In reality, n=2 is a good approximation for the DO reduction on the electrode surface [104]. Although it was concluded that at extremely small t the diffusion profile for the ring electrode could be estimated by the Cottrell equation for a planar electrode since the edge effect is negligible [156], the measured current was around 50% of the calculated current in the transient region based on the Cottrell equation (3.13). The correlation between the two diffusion profiles is more complicated since t is not considerably small during the measurement. Stirring could also contribute to

the deviation. Therefore, a factor of 2 was utilized in the sensors to match the theoretical Cottrell equation shown in Figure 4.12 and to provide a better estimation.

The theoretical steady-state current for the ring electrode DO sensor was reported by Zoski as in equation (4.2) [157].

$$i_{ss} = nFDC_o l_o \tag{4.2}$$

where:

$$l_o = \frac{\pi^2 (b+c)}{\ln\left[\frac{16(b+c)}{c-b}\right]}, \frac{c}{b} < 1.25 \tag{4.3}$$

and c is the outer radius of the ring electrode and b is the inner radius of the ring electrode.

After calculation the theoretical steady-state current was found to be -0.18 µA at 7.5 mg/L, -0.12 µA at 5mg/L and -0.07 µA at 3mg/L. All sensors except for DO-8 showed similar currents to the theoretical estimation. The lower collected currents for DO-1 to DO-7 (compared with theoretical value) can be explained by the smaller effective area of the WEs since the surfaces were not purely clean and had unremovable insulation residues. DO-8 suffered delamination of the insulation layer, and although it still showed good calibration results (Table 4.8) the sensor was not suitable for further use as the active Pt area was much bigger than anticipated.

In conclusion, 8 DO sensors could be used for DO detection between 1-8 mg/L with excellent accuracy (1.7%) and a good match to theory. Nevertheless, the DOC in rumen fluid is much lower than the LOD of 1mg/L. The high LOD of DO sensor is due to the small current generated across the microelectrode because noise dominates the CA output at smaller DOC. Therefore, these microfabricated DO sensors were unlikely to be suitable for DO monitoring in the rumen.

4.5 Conductivity sensor

4.5.1 Fabrication and measurement

The four-electrode conductivity sensors used the ring electrodes on chips A (A1-A5), while two-electrode conductivity sensors were based on the two Pt electrodes of chips D. The measurement circuitry for the 4-electrode conductivity sensor is shown in Figure 4.13a. A trans-impedance amplifier was used through the bipolar operational amplifier (op-amp) AD822AN (Analog Devices, UK). The op-amp was powered by two 12V A23 batteries to provide dual supplies of ±12V. A commercial signal generator (Agilent 33250A, UK) delivered ±0.5V, 10kHz square wave signal to the trans-impedance amplifier. The 4.7µF capacitor was used to remove the DC offset. At a frequency of 10kHz, the capacitor had negligible influence on the current and thus the conductivity

cell, leading to a theoretical square wave output current of ±0.5mA ($I = \frac{V}{R} = \frac{\pm 0.5}{1000} A = \pm 0.5mA$).

The 100MΩ resistor was selected so that the leakage resistance was much bigger than the input resistance (1kΩ) and the solution resistance. The trans-impedance amplifier was first tested with a resistor. For the four-electrode conductivity sensor (Figure 4.13a), the AC current flowed between the inner ring electrode and the outer ring electrode. The circuitry demonstration for a four-electrode sensor is shown Figure 4.13b. The differential voltage across the middle two ring electrodes was measured by the NI-6211. For the two-electrode sensor, the same circuitry was used, but the two electrodes were connected for current injection from the trans-impedance amplifier as well as the voltage detection through the NI-6211 device (Figure 4.13c).
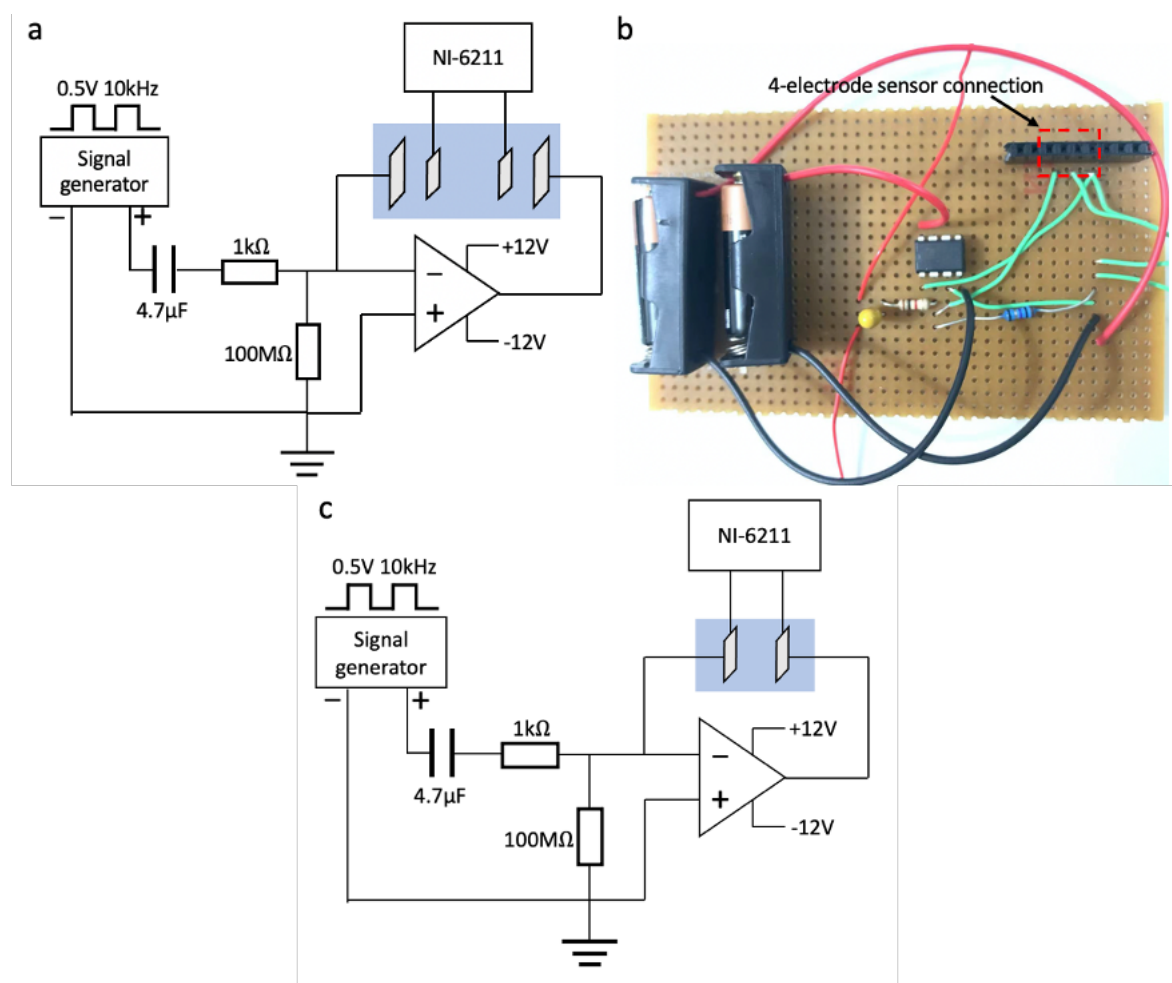
FIGURE 4.13: Conductivity measurement circuitry (a) and PCB (b) for a 4-electrode conductivity sensor. A trans-impedance amplifier was implemented with a bipolar op-amp AD822AN. A commercial signal generator produced a square wave voltage of ±0.5V at 10kHz, and a current of ±0.5mA was expected across the conductivity cell. (c) Conductivity measurement circuit for a 2-electrode conductivity sensor.

The NI-6211 sampled the output voltage from the conductivity cell at a sample rate of 100kHz. Four readings on consecutive positive half cycles of the voltage were averaged

to give an output voltage for each conductivity calibration solution. Each measurement lasted approximately 1s. Conductivity calibration solutions for the sensors were prepared by mixing 1413µS/cm, 5000µS/cm, 12880µS/cm and 80000µS/cm standard conductivity calibration solutions (Hanna Instrument, UK) to give 6 different conductivities across 1-50mS/cm. The reference conductivity of each calibration solution was recorded with a commercial conductivity meter (LAQUAtwin EC-22, HORIBA, UK) at $22 \pm 2°C$.

4.5.2 Results and discussion

Typical output voltage waveforms at different conductivities for four-electrode (a) and two-electrode (b) conductivity sensors are shown in Figure 4.14. Large variations in the output voltage were found for the two-electrode conductivity sensor due to the C_{dl} at the electrode-electrolyte surface, leading to large uncertainties and bad linearities for between the signal output and solution resistivity. Therefore, this method was not used. The four-electrode conductivity sensor was acceptable although it was reported that the removal of polarization effect for four-electrode sensors was not complete [131].
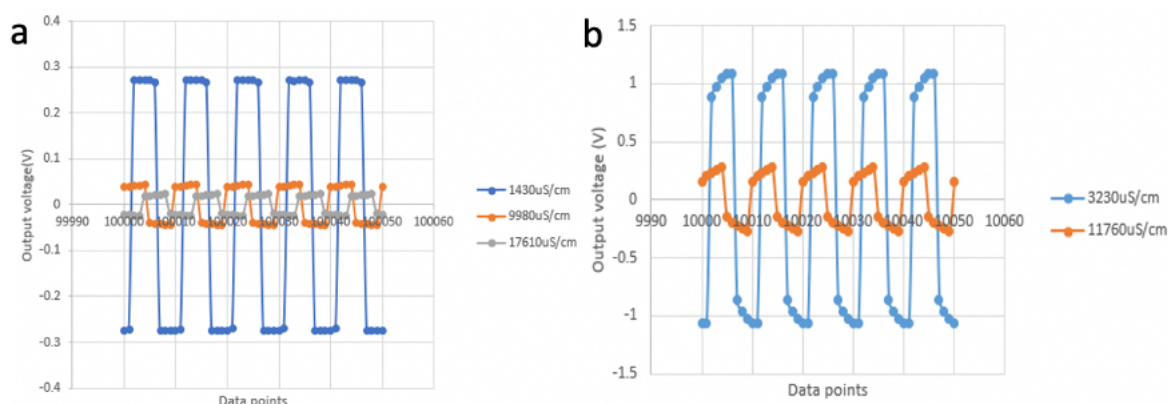
FIGURE 4.14: Typical output voltage waveforms for different solution conductivities for four-electrode (a) and two-electrode (b) sensors. Large variations in the voltage output in a single square wave cycle were found for the two-electrode conductivity sensor due to the C_{dl} at the electrode-electrolyte surface.

The trans-impedance amplifier circuit was calibrated with resistors from 100-8200Ω, which sufficiently covered the targeted solution resistance. The linear fitting slope indicated a current of 0.477mA through the loop. The slight difference between the actual current and the calculated current (0.5mA) arose from the tolerance of the input resistor and the output voltage from the signal generator.

Since A5 suffered insulation failure, 4 separate four-electrode conductivity sensors (A1-A4) were calibrated in 6 different solutions. Figure 4.15a shows a linear correlation
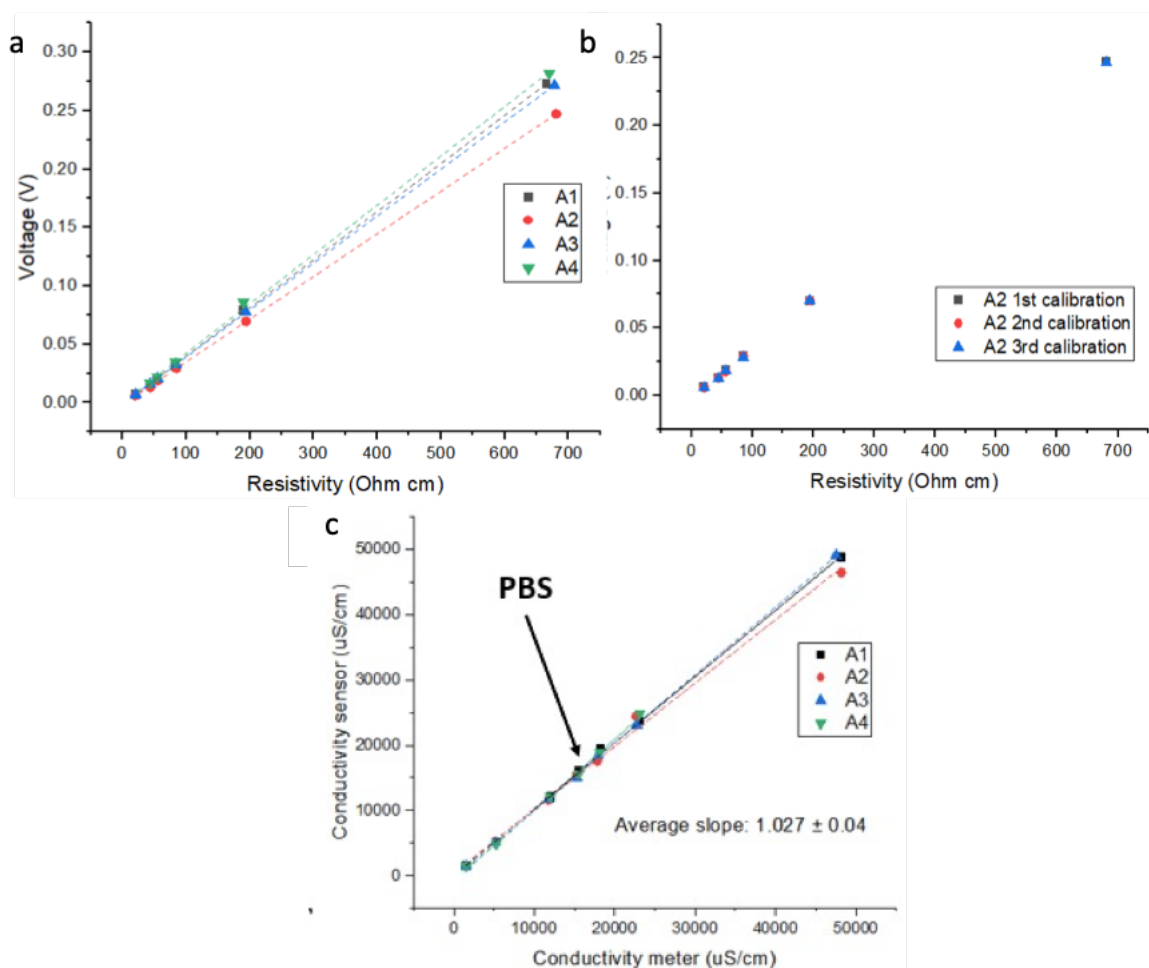
FIGURE 4.15: a) Plots of voltage vs solution resistivity for 4 sensors A1-A4. (b) Repeatability tests for sensor A2 on 3 consecutive days. Pearson correlation coefficient r>0.9999 for results from any two days. (c) Fits of measurements in PBS; the measured conductivities plotted against the conductivity meter readings for 8 solutions.

(R^2>0.999 for all fittings) between the resistivity of the solution and the output voltage. The 4 sensors were then used to measure a PBS solution with the measured conductivities plotted against the conductivity meter readings for PBS and 6 calibration solutions (Figure 4.15c). The average slope of 1.027 for the 4 sensors indicates a good match between the measured conductivity and the reference conductivity.

Sensor	Conductivity meter (μS/cm)	Resistivity (Ω · cm)	Output voltage (V)	Measured conductivity (μS/cm)	Error (μS/cm)
	1501.83	665.85	0.273	1504.55	2.72
	5266.80	189.87	0.079	5115.14	-151.66
A1	12038.40	83.07	0.032	12234.57	196.17
	18255.60	54.78	0.020	19100.26	844.66
	23166.00	43.17	0.016	23547.29	381.29
	48213.00	20.74	0.007	49419.29	1206.29

	1468.46	680.99	0.246	1469.99	1.53
	5149.76	194.18	0.070	5067.54	-82.22
A2	11770.88	84.96	0.029	11742.11	-28.77
	17849.92	56.02	0.018	17885.32	35.40
	22651.20	44.15	0.013	24447.50	1796.30
	48206.40	20.74	0.006	46458.36	-1748.04
	1474.52	678.18	0.273	1477.16	2.63
	5171.04	193.38	0.079	5036.71	-134.33
A3	11819.52	84.61	0.032	11863.59	44.07
	17923.68	55.79	0.020	18516.72	593.04
	22744.80	43.97	0.015	23284.76	539.96
	47530.80	21.04	0.006	49650.01	2119.21
	1492.73	669.91	0.283	1499.16	6.43
	5254.56	190.31	0.085	4922.00	-332.56
A4	11965.44	83.57	0.033	12404.65	439.21
	18144.96	55.11	0.021	18960.64	815.68
	23124.00	43.25	0.016	24509.02	1385.02
	48117.60	20.78	0.007	53993.15	5875.55

TABLE 4.9: Summary of the performance of sensor A1-A4.

A summary of the performance for the four sensors is given in Table 4.9 and Table 4.10. Larger deviations were found at high conductivities (>18mS/cm) due to the reduced accuracy of the commercial conductivity meter above 20mS/cm (from ±2% to ±5%).

Sensor	Intercept (mV)	Sensitivity $(mV/(\Omega \cdot cm))$	Mean error (%)	Uncertainty (%)	Cell constant (cm^{-1})
A1	-1.71	0.413	1.3	1.1	0.87
A2	-2.1	0.365	0.5	2.4	0.77
A3	-1.97	0.405	1.3	1.8	0.84
A4	-1.32	0.426	1.7	3.1	0.89

TABLE 4.10: Summary of the performance of sensors A1-A4 in terms of cell constant and measurement accuracy.

The table indicates accuracies ranging from ±0.5% to ±2.7% for the 4 sensors. Repeatability tests for A1-A3 over 3 consecutive days were made and example results for A2 were plotted in Figure 4.15b. For all 3 sensors, excellent reproducibility was confirmed (Pearson correlation coefficient r>0.9999). The cell constant of the sensors was calculated from the measured conductivity and the ideal conductivity with a value of

0.84 ± 0.045 cm^{-1}. The variations in cell constant among sensors arose from the discrepancies in active electrode area affected by the insulation process.

In summary, the conductivity sensor was a good candidate for rumen conductivity monitoring within the specified range with comparable performance to commercial meter.

4.6   ORP sensor

4.6.1   Fabrication and measurement method

ORP sensors could be made from any of the Pt electrodes. Chip A was selected. Eight chips were used (ORP-1 to ORP-8) and measured in two ORP calibration solutions. Prior to calibration, the Pt electrodes were cleaned with 3-5 CVs (window -1V to +1V) in PBS and left in DI water overnight. The sensors were then calibrated in the calibration solutions and the ORP was measured in PBS. against a commercial DJRE. For the 220mV calibration solution, the measurement lasted 8mins. In the 468mV calibration solution, the measurement was for 2mins to avoid insulation failure due to the extremely low pH (<0.1) of the solution.

4.6.2   Results and discussion

The output potentials of four different solutions for ORP-1 to ORP-8 were shown in Figure 4.16a-d, and summarized in Table 4.11. From the calibration results, the ORP sensors showed expected potentials immediately after immersion, with deviations <8mV, meaning that they were suitable for ORP detection.

Sensor	ORP in 220mV calibration solution (mV)	ORP in 468mV calibration solution (mV)	ORP in PBS (mV)
ORP-1	227.6	463.0	206.5
ORP-2	228.1	463.2	210.2
ORP-3	227.7	463.3	196.7
ORP-4	227.6	463.3	215.3
ORP-5	228.3	463.3	211.0
ORP-6	227.4	463.3	209.3
ORP-7	227.5	462.2	211.8
ORP-8	227.5	460.7	222.8

TABLE 4.11: ORP voltage from ORP-1 to ORP-8 for three different solutions. Voltage deviations were <8mV in 220mV and 468mV calibration solutions.
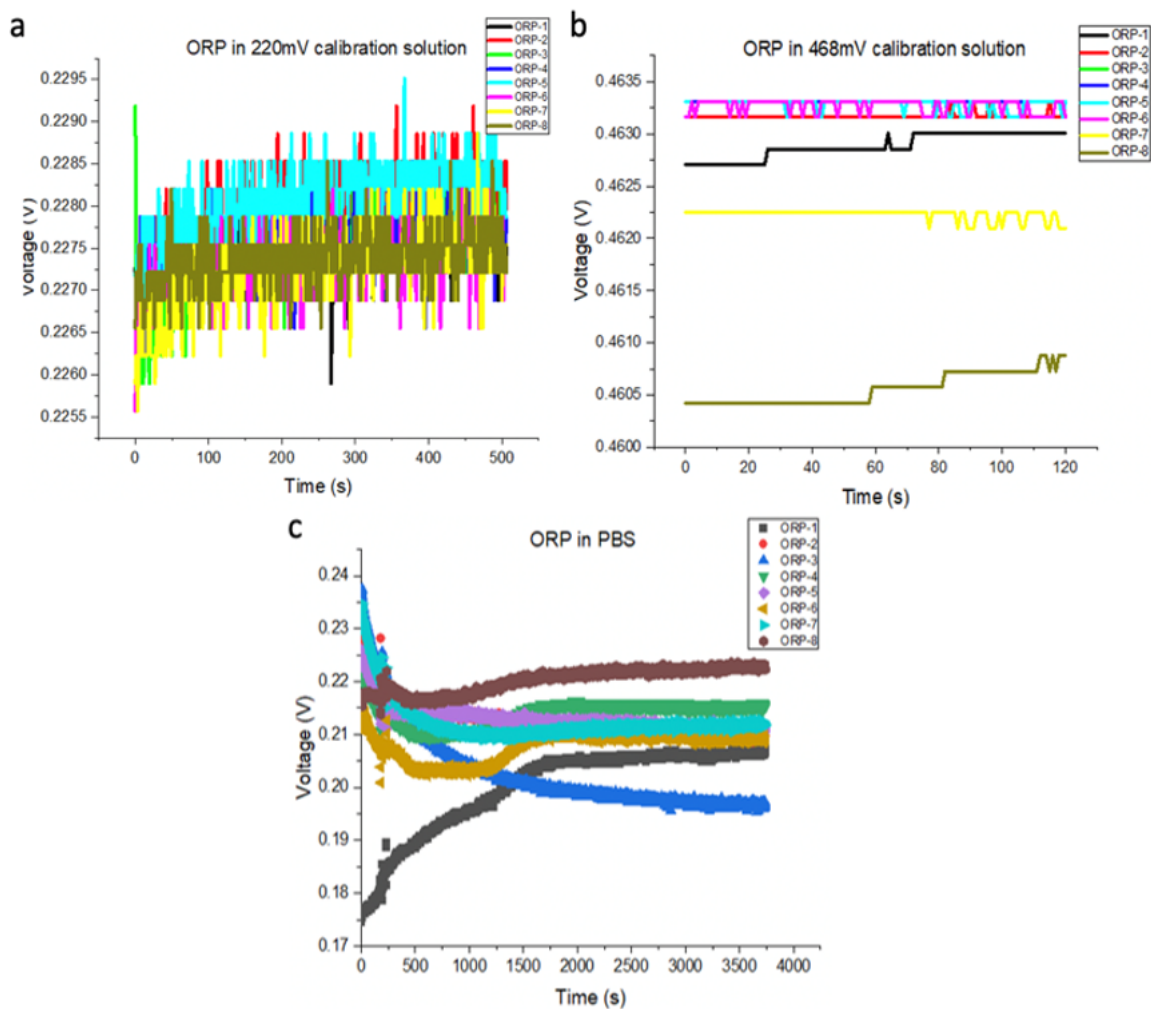
FIGURE 4.16: Data traces for eight ORP sensors (ORP-1 to ORP-8) in (a) 220mV calibration solution, (b) 468mV calibration solution, and (c) PBS. The ORP sensors had expected potentials immediately after immersion with deviations <8mV.

In PBS the sensors took 40mins to stabilize, yielding an ORP of 210.4±6.9mV. The sensors were feasible for rumen measurements with typical range -100mV to -200mV against SHE as long as the electrodes were allowed to spend some time to reach the equilibrium.

Chapter 5

In vitro study

In vitro studies were made with three samples of rumen fluids, including two samples during a field visit to RAFT Solutions Ltd, Ripon and one frozen rumen sample stored in the laboratory. The results from the in vitro studies are summarized and analyzed in this chapter.

5.1 Overview

In order to better understand the functionality of the sensors, a field visit was taken to RAFT Solutions Ltd. The study aimed to measure Cl^- concentration, conductivity, pH, ORP and DOC in rumen fluid. All parameters were also measured using commercial benchtop equipment.

Two types of rumen contents namely RC-1 and RC-2 were used. RC-1 is a batch of rumen contents freshly delivered from a local abattoir at 11 am on the second day of the visit. RC-2 is the fresh rumen samples collected from one of the cows at RAFT on the third day of the visit. Apart from the separate cows from which the rumen contents were collected, the main difference between RC-1 and RC-2 was that the protozoa within RC-1 were dead, while the protozoa within RC-2 were active and abundant for the first 6 hours.

After the site visit, data were obtained in a laboratory environment from frozen rumen contents (RC-3). The rumen contents were defrosted and heated to room temperature prior to use. The protozoa in this sample were dead and did not affect the experimental results.

For all three types of samples, the rumen fluid was filtered through a muslin cloth bag into 50ml falcon tubes, with 25-30ml fluid in each falcon tube. Spot measurements were performed for pH, Cl^- and conductivity sensors, whilst ORP sensors were measured

continuously in each rumen fluid. The time at which the first measurement was made in each type of rumen fluid was designated as 0h.

5.2   Preparation

During the site visit, 2 types of chips were used, 8 x A chips (A6-A13) (Figure 5.1a) and 15 x B chips (B1-B15) (Figure 5.1d), labelled A6-A13 and B1-B15. Conductivity was measured with chips A while pH and ORP were measured using the front-side RuO_x electrode and one of the back-side Pt electrodes on B chips. The Cl^- sensors were fabricated using two different methods: Ag/AgCl paste deposition on the back-side of chips A7-13 (Type 1 QRE, P1-P7) or Pt to AgCl conversion on the back-side of chips B2-6 (Type 2 QRE. E1-E5).
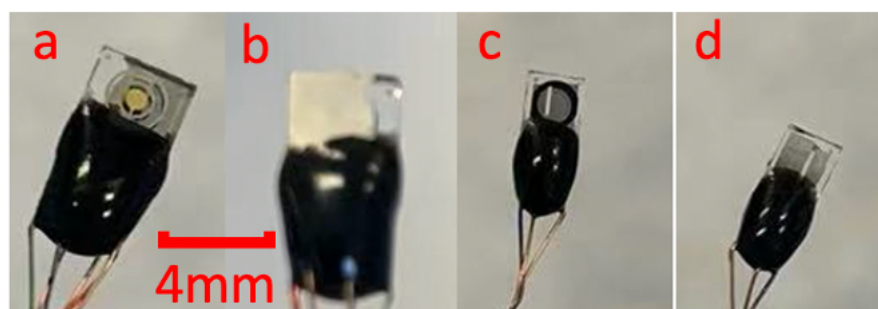
FIGURE 5.1: Pictures of the chips used during the field visit. (a) front-side of chip A including 4 ring electrodes for conductivity sensing and a gold central electrode (not used); (b) back-side of chip A after Ag/AgCl paste deposition; (c) front-side of chip B with a RuO_x pH sensor and a Pt ring electrode (not used); (d) back-side of chip B with 2 Pt electrodes.

Integrated chips (E and F) and chips A were used to measure RC-3. For some chips E, 3D printed chip holders (Figure 5.2a) were used for the black epoxy insulation. ORP was measured with chips F. The conductivity measurement was divided into two parts. Spot measurements were conducted using a four-electrode conductivity sensor on chip E while the long-term stability test in RC-3 was done with three chips A.
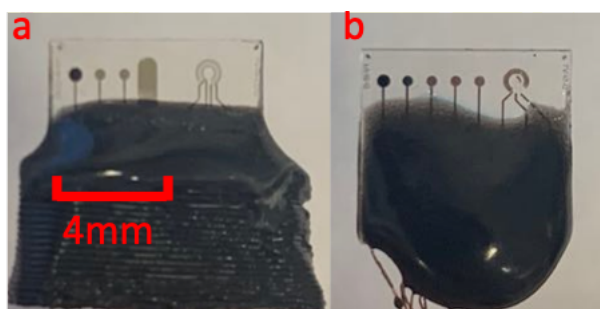
FIGURE 5.2: Photograph of (a) chips E and (b) chips F used to measure RC-3.

5.3 QRE (Cl⁻ sensor)

All three types of QRE were calibrated before the visit using 0.01M to 1M KCl solution. As expected, near-Nernstian responses were seen for all QREs as shown in Figure 5.3a-c. The same setup was used as detailed in Chapter 4.2.1.
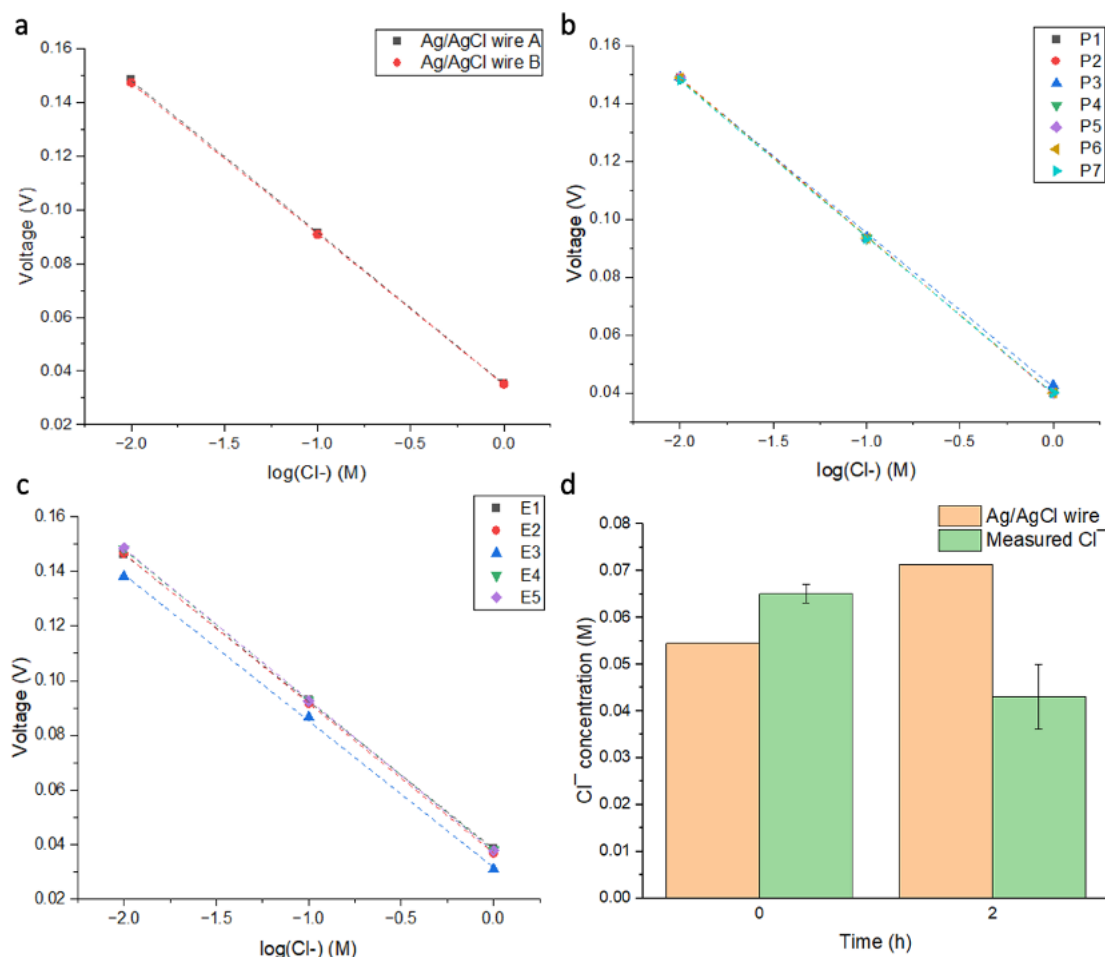
FIGURE 5.3: Cl⁻ calibration plots for three types of QREs: (a) 2x Ag/AgCl wires (Type 3 QREs), (b) 7 x Type 1 QREs and (c) 5 x Type 2 QREs. (d) Spot measurements for 3 x Type 1 QREs were made in RC-1 at 0h and 2h and compared to a Ag/AgCl wire.

Type	Sensor	Intercept (mV)	Sensitivity (mV/dec)	R^2
	P1	39.5	-54.48	0.999
	P2	39.45	-54.65	0.999
	P3	41.96	-53.2	0.999
1	P4	39.8	-54.24	0.999
	P5	39.59	-54.45	0.999
	P6	39.64	-54.41	0.999
	P7	39.77	-54	0.999

	E1	38.52	-53.86	0.999
	E2	36.95	-54.77	0.999
2	E3	31.69	-53.57	0.999
	E4	37.89	-55.03	0.999
	E5	37.57	-55.36	0.999
3	A	35.08	-56.51	0.999
	B	34.93	-56.16	0.999

TABLE 5.1: Calibration results for both type of Cl⁻ sensors. The sensors were immersed for at least 40mins in each calibration solution.

In vitro experiments were conducted in RC-1 using all three types of QREs. Spot measurements were taken at 0h and 2h with each measurement lasting 20 minutes. Unfortunately, type 2 QREs suffered Ag/AgCl degradation after immersion into the rumen fluid, while Type 1 had good sensitivities at 0h. Ag/AgCl degradation for Type 2 QRE or the Ag/AgCl wire was noted when the colour of the AgCl layer turned white (from dark brown) and a rapid decrease in output voltage was seen. This phenomenon was not observed during lab calibration.

Three Type 1 QRE (Cl⁻ sensors) gave an average of 0.065M for RC-1 with small discrepancy of 0.01M when referenced to the Ag/AgCl wire. The Cl⁻ concentrations in Molar were acquired based on the conversion of output voltage through linear fits from calibration results (Table 5.1). After 2h the precision of Type 2 QREs wire was low because the Ag/AgCl layer became fragile in rumen fluid. The chloride layer came off, exposing the Pt edges to the rumen fluid. Degradation of the Ag/AgCl wires was also observed at 2h, meaning that the QRE were no longer stable.

The outcome of these experiments implied that all three types of QREs were not able to withstand the rumen environment due to poor adhesion and degradation of the AgCl.

5.4   pH measurement

5.4.1   Measurement technique

15 x RuOx electrodes were used on chips B1-B15 and calibrated in a laboratory environment (23°C) in 4 different pH buffer solutions 5, 6, 7 and 8 (Reagecon). Since hysteresis and drift effect were common issues for electrochemical pH sensors [76], a pre-calibration was made before the in vitro study. Three sensors with the highest sensitivities (B1, B5, B11) were selected for 3 spot measurements in RC-1 at 0h, 2h and 19h. Each spot measurement took at least 30 minutes at ambient temperature (16 ± 2°C).

Continuous pH monitoring was done between 3h and 18h using 3 sensors to examine the long-term stability of the pH sensors in a rumen environment. To mimic the daily variation in rumen pH, tests were conducted after 19h. The sensors were continuously immersed in RC-1 to which acid was added to reduce the solution pH.

A DJRE was used to provide a reference potential for pH measurement. The pH outputs for each sensor were obtained by linear fitting and the average measured pH among 3 sensors was recorded as the measured pH. A commercial pH meter was also used to measure the reference pH value of RC-1. The pH measurement was not conducted in RC-2 since there were no adequate time sensors for pre-calibration. Moreover, unfortunately, the pH electrodes on chips E and F suffered poor adhesion and insulation during fabrication, precluding their usage in RC-3.

5.4.2 Results and discussion

Figure 5.4 shows calibration data giving -55.14mV/pH to -56.62mV/pH (Table 5.2).
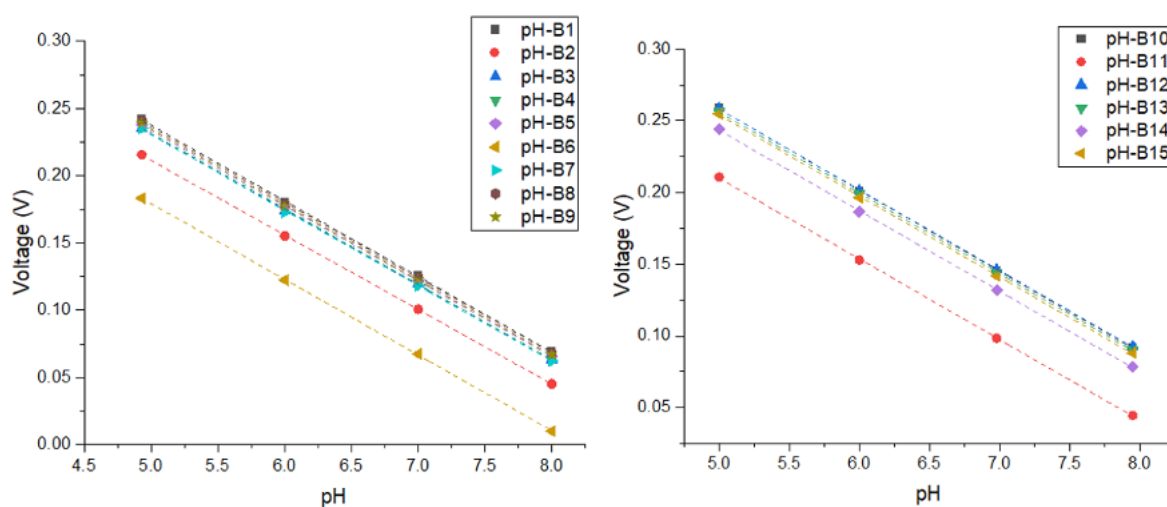
FIGURE 5.4: Calibration of 15 x pH sensors prepared for the field visit.

Sensor	Intercept (mV)	Sensitivity (mV/pH)	R^2
pH-B1	518.85	-56.24	0.999
pH-B2	488.61	-55.44	0.999
pH-B3	509.87	-55.85	0.999
pH-B4	512.63	-56.18	0.999
pH-B5	513.16	-55.93	0.999
pH-B6	460.76	-56.3	0.999
pH-B7	511.09	-56.14	0.999
pH-B8	516.75	-56.08	0.999

pH-B9	515.04	-56.07	0.999
pH-B10	541.43	-56.62	0.999
pH-B11	491.55	-56.29	0.999
pH-B12	539.6	-56.27	0.999
pH-B13	538.02	-56.39	0.999
pH-B14	524.39	-56.17	0.999
pH-B15	536.52	-56.48	0.999

TABLE 5.2: Calibration data for 15 x pH sensors.

The pre-calibration results are plotted in Figure 5.5, summarised in Table 5.3. A small hysteresis (<10mV) in intercept was seen for each sensor along with a decrease in sensitivity which is probably due to the lower ambient temperature (15°C). Although the temperature effect given by the Nernst equation is minor, an average sensitivity drop of $0.388 mV/pH°C^{-1}$ was seen for RuO_x pH sensors [158].
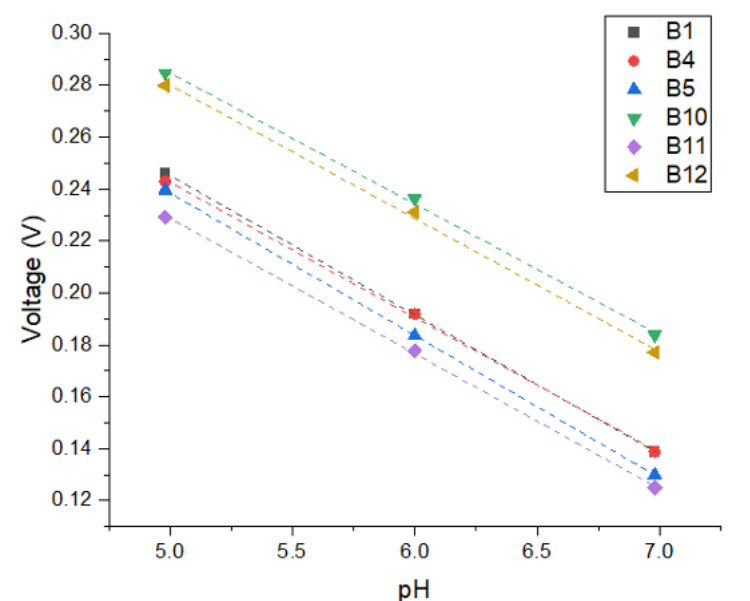
FIGURE 5.5: Pre-calibration data for 6 x pH sensors. Lower sensitivities were seen for pH sensors because of the low ambient temperature.

Sensor	Intercept (mV)	Sensitivity (mV/pH)	R^2
pH-B1	513.7	-53.7	0.999
pH-B4	502.6	-52.0	0.999
pH-B5	512.7	-54.9	0.999
pH-B10	536.7	-50.4	0.999
pH-B11	489.3	-52.1	0.999

| pH-B12 | 536.8 | -51.4 | 0.999 |

TABLE 5.3: Summary data for 6 x pH sensors measured during pre-calibration.

The pH value for each spot measurement was compared to the pH meter reading, see Figure 5.6a. A good match was found between the sensor reading and the pH meter reading. The pH of RC-1 was relatively steady for the first 19 hours with a small fluctuation around pH 7.6. The pH of RC-1 was higher than the normal rumen pH range (5.5-7), explained by the general higher pH output when measuring in vitro, with a maximum deviation of 0.65pH from existing studies [37]. It was assumed that the higher pH for in vitro experiment was attributed to a much lower concentration of dissolved CO_2 in RC-1 due to air exposure [13]. Over the measurement period, the pH declined initially down to 7.36, followed by an increase for 10 hours to 7.62. As the commercial pH probe was not capable of logging pH reading remotely and independently, and the continuous pH measurement was conducted overnight on that day without data entry to the reference pH value, potential errors could arise from the ambient temperature change and subsequently the sensitivity change of homemade pH sensors.

Time (h)	pH meter	B1	B5	B11	Measured pH	STD
0	7.62	7.48	7.46	7.52	7.49	0.03
2	7.67	7.60	7.57	7.66	7.61	0.05
19	7.55	7.33	7.42	7.59	7.45	0.14

TABLE 5.4: Comparison of results during spot measurements.

The pH variation test was used to fully justify the long-term stability of pH sensors in vitro after 18 hours of immersion, as well as the ability to track possible daily rumen change when measuring in vivo. The pH data from RC-1 are summarised in Figure 5.7a. Obvious voltage increases were seen after the titration with a response time of 10-15 minutes to reach the stabilized voltage. It was shown that similar accuracies (0.1pH) were achieved during the pH variation test as in the spot measurements. This experiment proved that the pH sensors were able to perform real-time accurate measurements in accordance with pH change within rumen environment without the biofouling effect. Compared with the existing rumen system (Table 2.1), the pH was successfully detected with similar accuracy on a miniaturize sensor chip with a long-term stability of at least 20 hours. Within this period the effect of feed on rumen pH can be investigated when measuring in vivo, as well as the efficient health monitoring.
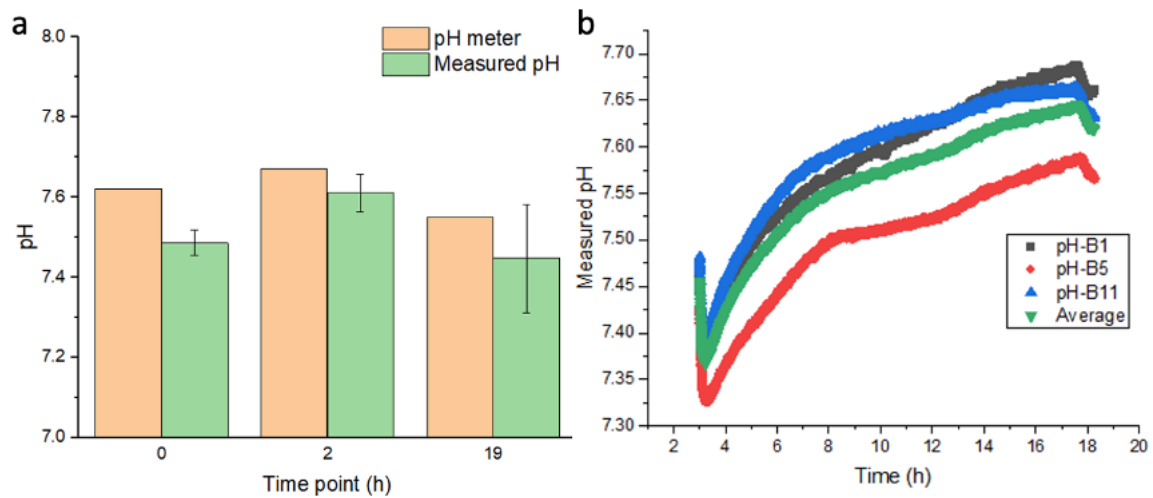
FIGURE 5.6: (a) Results from the sensor and commercial pH meter for 3 spot measurements. A good match was found between the sensors and the meter with an accuracy of 0.15pH. (b) Long-term pH monitoring of RC-1 with 3 sensors.
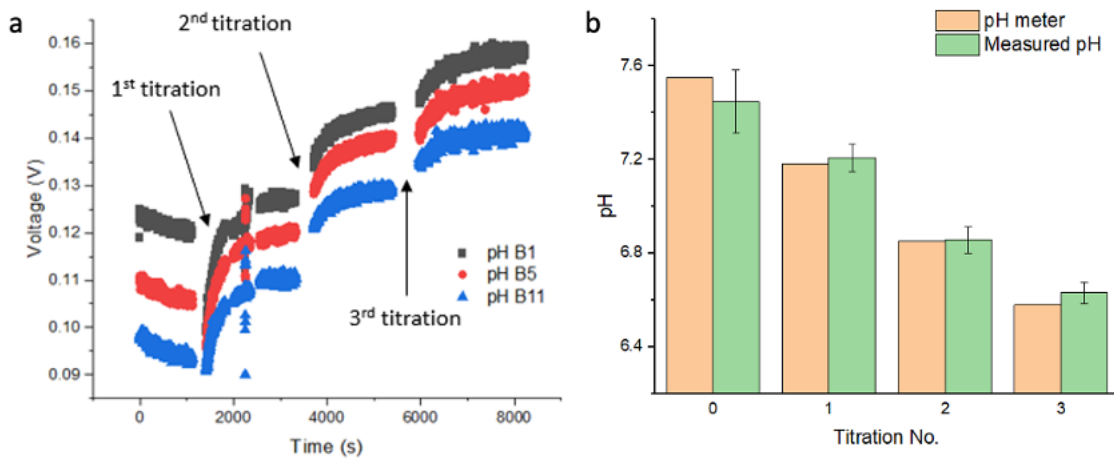
FIGURE 5.7: (a) Data traces for 3 sensors during pH variation test. (b) Comparison of pH sensor outputs and pH meter readings during pH variation test in RC-1.

Titration No.	pH meter	B1	B5	B11	Measured pH	STD
0	7.55	7.33	7.42	7.59	7.45	0.14
1	7.18	7.20	7.15	7.27	7.21	0.06
2	6.85	6.86	6.80	6.91	6.86	0.06
3	6.58	6.62	6.59	6.68	6.63	0.05

TABLE 5.5: Comparison of results during pH variation test.

5.5   ORP measurement

5.5.1   Measurement technique

15 ORP sensors were calibrated in the laboratory prior to the field visit. Since ORP requires a longer response time, biofouling might be a problem [147]. ORP was measured for 15 hours in RC-1 with 3 sensors and 23 hours in RC-2 with 4 sensors. For RC-3, 6 calibrated ORP sensors were prepared with 4 sensors used to measure rumen ORP over 4 days.

For ORP measurements calibration solutions of 86mV, 263mV (Fisher Scientific, UK) and 468mV (Mettler Toledo, UK) were used. The quinhydrone 86mV (pH 7) and 263mV (pH 4) calibration solutions were influenced by the temperature and the RE used. It was discovered in [159] that the standard ORP of 86mV or 263mV were measured against Ag/AgCl RE with saturated KCl solution. Under laboratory conditions (22.5°C), the quinhydrone calibration solutions should show 79mV and 255mV against a RE filled with 3M KCl. Measurement of ORP in RC-1 started at 3h because the sensors were used for pH measurements. Measurement of RC-2 was done immediately after the collection of rumen fluid. In both cases, the Pt surface of the sensors was cleaned and dried before the experiment.

For RC-3, the Pt electrodes on chip F were used to measure the ORP. Three different calibration solutions (124mV, 220mV and 468mV) were used to calibrate the sensors.

5.5.2   Results and discussion

For RC-1 and RC-2, 15 x Pt electrodes were used to measure ORP. The calibration results are in Table 5.6; large deviations in the ORP sensors were seen for the quinhydrone calibration solutions compared with the 220mV calibration solution, possibly due to the high uncertainty (±30mV) of the new standard solutions. Since the quinhydrone calibration solutions had been open for a week before calibration, a potential drift of the calibration solution may have occurred. ORP-B6 and ORP-B9 did not have an acceptable ORP in the 255mV standard solution.

Sensor	Output (mV) in standard calibration solution		
	79mV	255mV	468mV
ORP-B1	50.9	212.7	484.7
ORP-B2	100.1	231.5	484.5
ORP-B3	46.8	213.7	484.8
ORP-B4	67.8	214.1	484.7
ORP-B5	77.7	221.8	484.7

ORP-B6	72.6	125.8	484.7
ORP-B7	59.4	218.6	484.8
ORP-B8	52.1	213.6	484.8
ORP-B9	83.9	92.3	484.8
ORP-B10	75.3	242.8	492.0
ORP-B11	97.9	245.0	492.1
ORP-B12	72.2	241.3	491.9
ORP-B13	97.7	244.9	492.0
ORP-B14	85.9	238.9	492.0
ORP-B15	101.9	246.7	492.1

TABLE 5.6: Calibration data of ORP sensors for the field visit. The sensors were immersed in 79mV & 255mV calibration solutions for 1 hour and 468mV calibration solution for 10 minutes.

By eliminating ORP-B6 and ORP-B9, the performance of the ORP sensors was considered acceptable (Figure 5.8) with an average deviation of 25mV for the 255mV standard solution, 5mV for the 79mV standard solution and 20mV for the 468mV standard solution.

Results in RC-1 and RC-2 are in Figure 5.9 showing it could take up to 10 hours for the ORP to reach a stable value in rumen fluid. An average ORP of -0.309±0.042V was measured during the steady-state response for the three sensors in RC-1, while the average ORP for the four sensors in RC-2 was -0.333±0.030V. A measurement gap was observed between 3h to 4h in RC-2 owing to a technical issue with the measurement laptop. After compensation for the SHE at 20°C (+0.21V), the ORP values were -0.099V in RC-1 and -0.123V in RC-2, similar to the reported rumen ORP for the sheep (ranging from -302 to -340mV vs Ag/AgCl RE) [160], and dairy cows of -115mV versus SHE [161].

The long response time could be partially explained by a combination of biofouling and oxygen leakage into the solution. It has been reported that air contamination can change the characteristic of the rumen environment, interfering with the ORP measurement [143]. Oxygen may have been responsible for the decrease of ORP in RC-2 as this is consumed by the active protozoa [162]. This finding matched data for rumen fluid of sheep [162]. The decrease in ORP was expected since the pH of RC-1 consistently increased between 3h-17h. The high variation in the ORP sensors was a common issue as there is no standard ORP calibration solution in the negative range [21]. Compared to the average ORP (-178.1mV) [21], the measured ORP in RC-1 or RC-2 was lower. This was expected as in vitro experiments generally had lower ORP due to contamination of the rumen environment, especially for hand-collected rumen fluid samples [21].
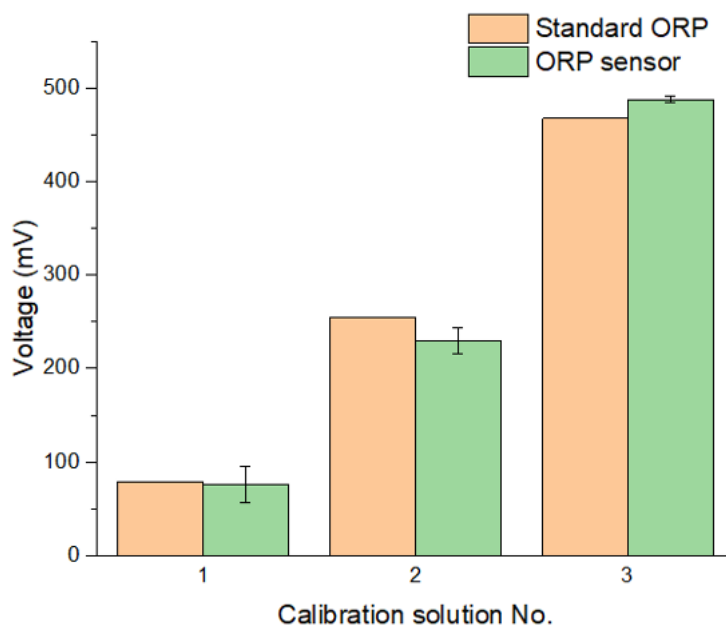
FIGURE 5.8: Calibration results of ORP sensors with standard calibration solutions.
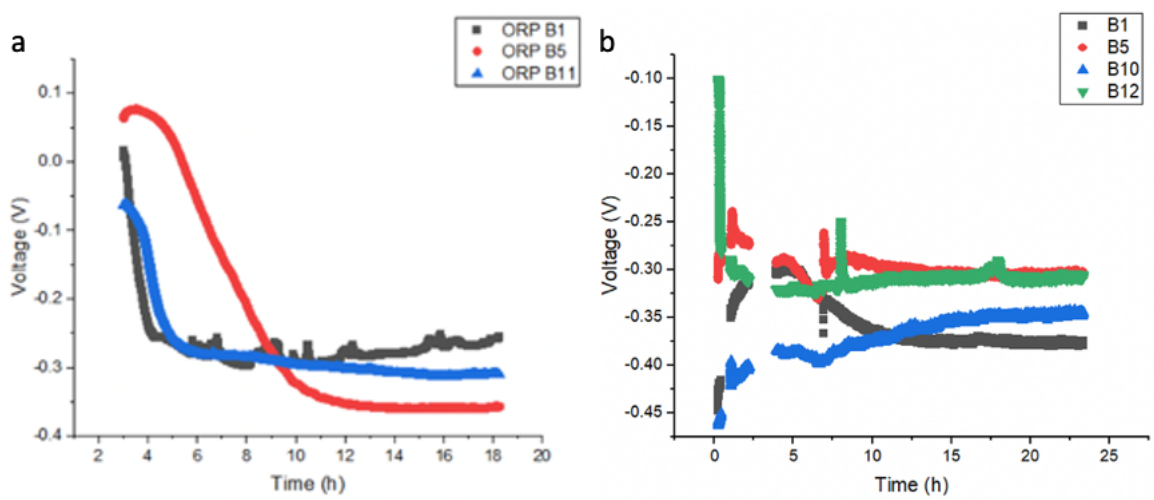
FIGURE 5.9: Long-term ORP results for (a) 16 hours in RC-1 and (b) 23 hours in RC-2.

Sensor	Output (mV) in standard calibration solution		
	124mV	220mV	468mV
ORP-F1	122.70	208.57	420.25
ORP-F2	125.36	213.13	437.97
ORP-F3	125.45	209.64	464.50
ORP-F4	125.34	212.97	464.80
ORP-F5	125.45	209.85	464.99
ORP-F6	125.39	212.06	464.77
ORP-F7	124.93	212.49	446.33
ORP-F8	125.32	212.10	464.90

ORP-F9	125.47	209.57	465.06
Mean	125.40	211.03	464.84
Std	0.06	1.51	0.20

TABLE 5.7: Calibration results of 9 x ORP sensors prepared for in vitro measurement in RC-3.

Calibration results for 9 sensors on chip F (ORP-F1 to ORP-F9) are listed in Table 5.7.
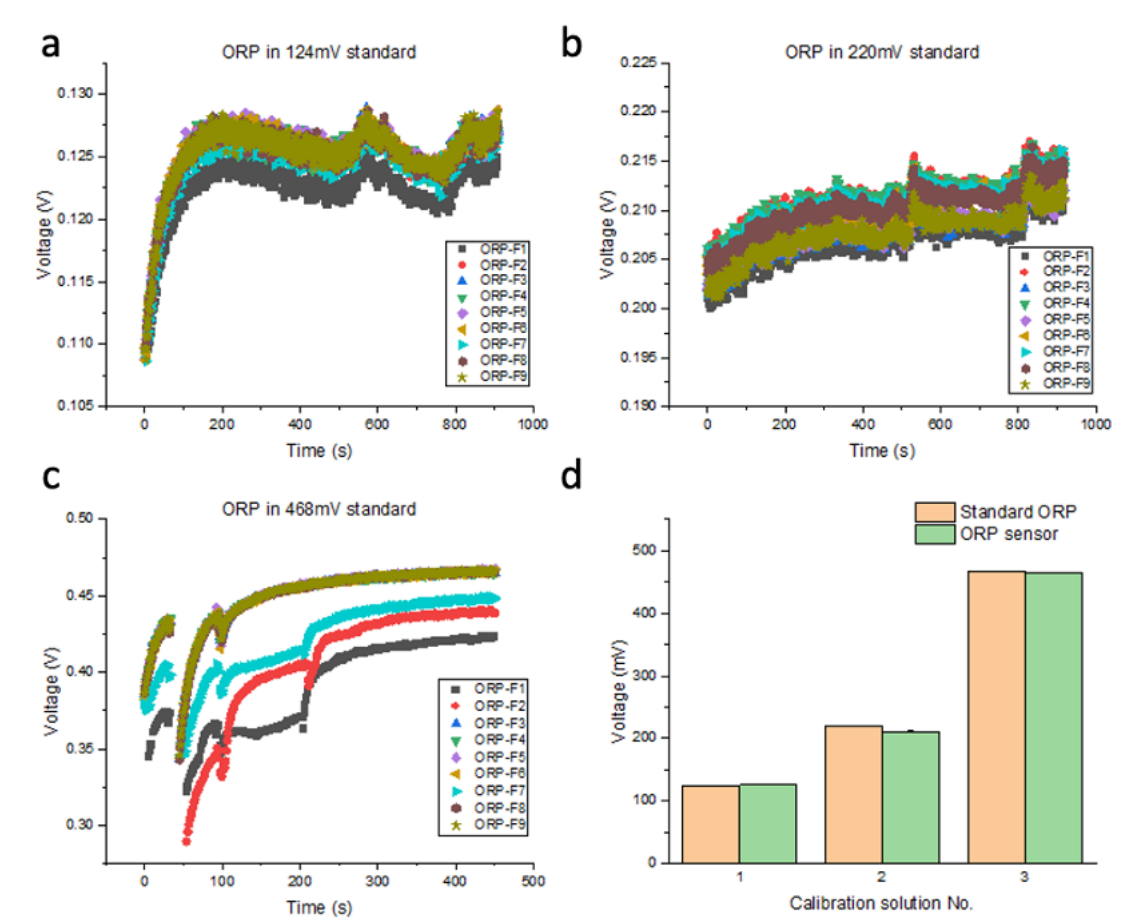
FIGURE 5.10: Calibration plots for 9 x ORP sensors in (a) 124mV, (b) 220mV and (c) 468mV standard calibration solution. (d) Comparison of calibration results from ORP sensors and the standard potential.

It was noted that ORP-F1, ORP-F2 and ORP-F7 did not show proper response in the 468mV calibration solution. Therefore, these 3 sensors were excluded. All other 6 sensors had excellent fit to the standard calibration potential with a maximum error of 10mV. The uncertainties across 6 sensors were also low (1.51mV max.).

To fully examine the long-term stability of the ORP sensors, 4 sensors were continuously measured in 220mV calibration solution (Figure 5.11). Low fluctuations (<10mV) were found for 2 days with low deviation (<20mV) from the reference potential.

Continuous ORP recording was conducted in RC-3 for 4 days, see Figure 5.12. Similar to the behaviour as seen in RC-1 and RC-2, generally decreasing trends were observed for all four sensors, but longer for 2-3 days. In the steady state, an ultimate average ORP of -0.07±0.01V versus SHE was measured, which is higher than the results for RC-1 and RC-2. Since there are no comparable long-term studies implemented in rumen fluid from available literature, the complete reason accounting for such behaviour needs further investigation in the future.
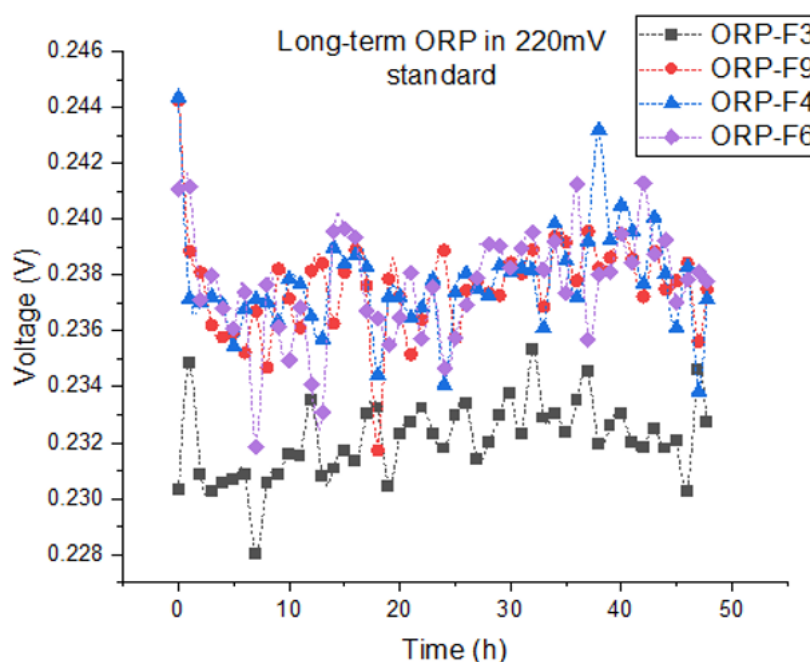
FIGURE 5.11: Long-term performance of ORP sensors in 220mV standard calibration solution. All four sensors showed low deviation (<20mV) against the reference potential over 2 days.
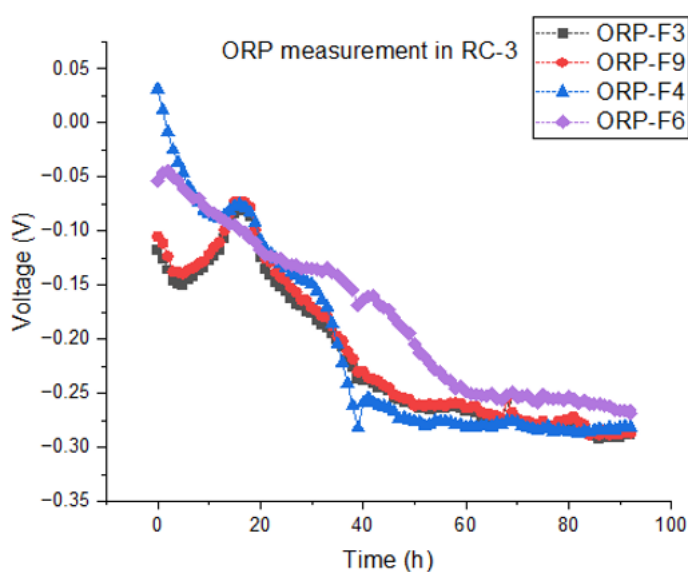
FIGURE 5.12: Long-term ORP measurement results in RC-3 over 4 days.

5.6   Conductivity measurement

5.6.1   Measurement technique

Before the field visit, conductivity sensors (A6-A13) were calibrated under the same measurement setup ($\pm$0.5V square wave input) as in Chapter 4.5.1 to measure RC-1 and RC-2. However, when measuring RC-3, the amplitude of the square wave decreased to $\pm$0.3V for all sensors (A6, A10, A11 and E1-E3) because a higher cell constant was used for chips E1-E3, based on the geometry of the conductivity sensors. A lower voltage prevented electrode contamination (oxide formation or hydrogen generation [163]) when calibrating in low conductivity solution (e.g., 1.5mS/cm).

The conductivity of RC-1, RC-2 and RC-3 was measured. Spot measurements were made for RC-1 (3 sensors) at 0h, 2h and 19h. Likewise, 4 sensors were used to record the conductivity of RC-2 at 0h, 3h and 6h. 3 conductivity sensors on chips E were used to measure the conductivity of RC-3 at 0h, 2h, 4h and 6h. During each measurement, the sensors were dipped into the rumen fluid for 2 minutes before taking any readings. The sensors were placed as close to each other as possible to avoid uneven conductivity distribution within the sample. Long-term conductivity measurement was performed in RC-3 for 7 days and measured every 24 hours. All measurements were compared with the reference reading from the commercial conductivity meter.

The method for conductivity data analysis was improved to achieve better accuracy for in vitro studies. For an output similar to one of the waveforms in Figure 4.13a, instead of directly averaging the middle three points in the positive half wave, the offset variance was removed by subtracting the average of points in the negative half wave from the average of positive half wave, followed by the division by 2 to calculate the output without offset noise.

5.6.2   Results and discussion

As shown in Figure Figure 5.13a, 7 sensors (A6-A12) were calibrated across the range of 1300-20000μS/cm. A crack was observed on the ring electrodes of A13 and this was discarded. Good accuracies (0.8%-2.0%) with low uncertainties were found after calibration (Table 5.8).

Good accuracies were observed in RC-1 using sensors A7-A9, summarized in Table 5-9. Measurement error was restricted within 325µS/cm (3.7%) (Table 5.9). The homemade conductivity sensors were capable of tracking changes in the rumen fluid with good accuracy similar to the commercial meter (Figure 5.13b).
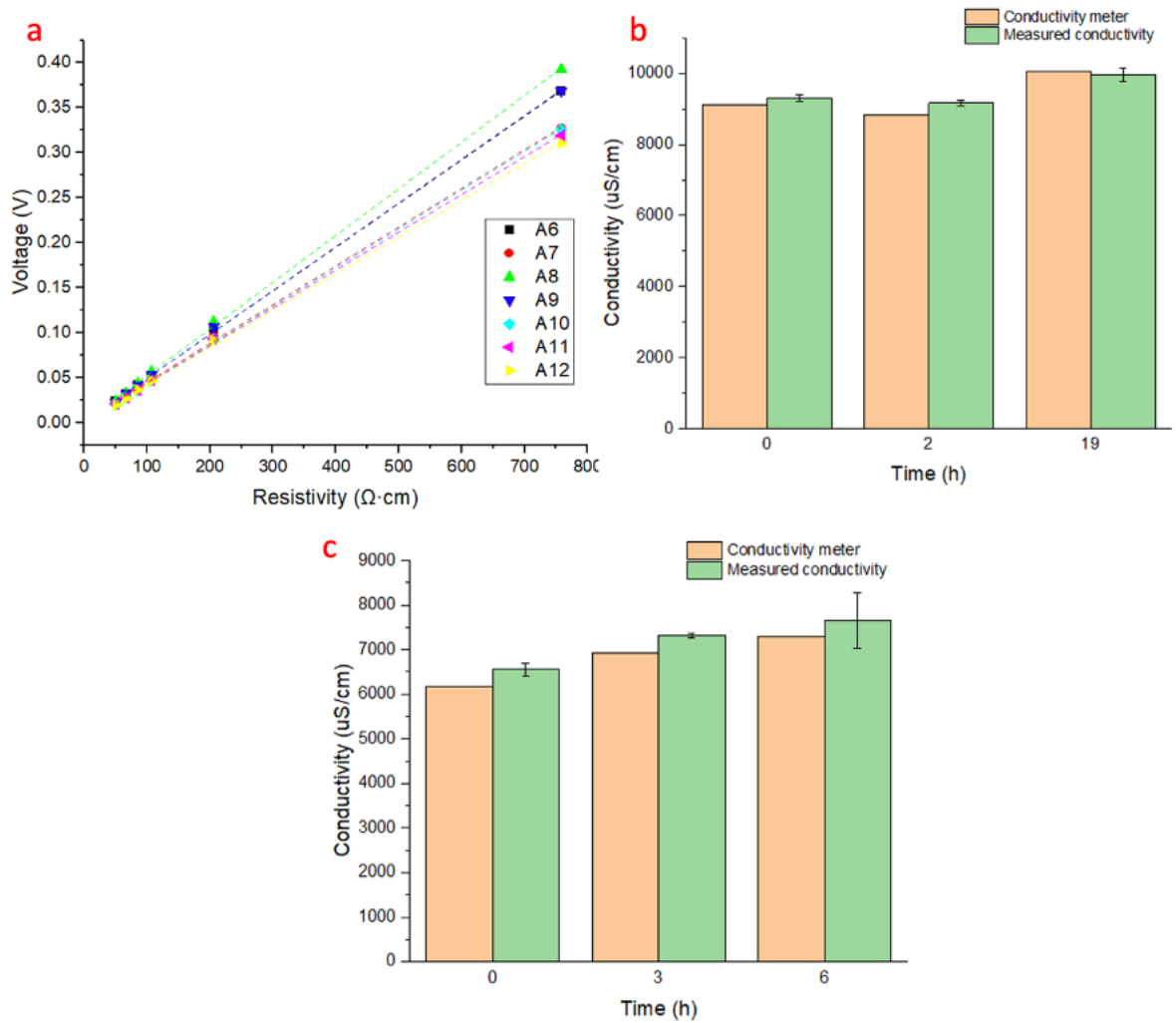
FIGURE 5.13: Sensor calibration and in vitro measurement. (a) Calibration results of 8 sensors (A6-A13) prepared for the field visit. A crack was observed on the ring electrodes of A13 and this was discarded. (b) Spot measurement results in RC-1 with 3 sensors. (c) Spot measurement results for RC-2 with 4 sensors.

Sensor	Intercept (mV)	Sensitivity (mV/($\Omega \cdot$ cm))	Accuracy (%)	Uncertainty (%)	Cell constant (cm^{-1})
A6	-2.13	0.51	0.8	1.1	1.02
A7	-3.54	0.49	2.0	0.8	0.90
A8	-4.63	0.57	1.4	0.4	1.09
A9	-4.2	0.54	1.5	0.7	1.02
A10	-3.55	0.47	1.3	0.6	0.90
A11	-3.33	0.47	1.6	1.4	0.88
A12	-3.33	0.46	2.0	0.9	0.86

TABLE 5.8: Summary of performance of A6-A12.

Time (h)	Conductivity meter (µS/cm)	A7 (µS/cm)	A8 (µS/cm)	A9 (µS/cm)	Measured conductivity (µS/cm)	Error (µS/cm)	STD (µS/cm)
0	9125.0	9366.8	9200.5	9320.3	9295.9	170.9	85.8
2	8837.2	9155.1	9087.7	9246.2	9163.0	325.8	79.6
19	10067.4	10166.6	9896.1	9825.1	9962.6	-104.8	180.2

TABLE 5.9: Spot measurement results with 3 sensors in RC-1.

Time (h)	Conductivity meter (µS/cm)	A7 (µS/cm)	A8 (µS/cm)	A9 (µS/cm)	A10 (µS/cm)	Measured conductivity (µS/cm)	Error (µS/cm)	STD (µS/cm)
0	6174.7	6562.0	6419.9	6505.2	6749.8	6559.2	384.5	139.8
3	6924.7	7327.8	7381.7	7258.4	7302.9	7317.7	393.0	51.4
6	7301.1	8144.1	7907.9	7783.5	6742.7	7644.6	354.5	619.5

TABLE 5.10: Spot measurement results with 4 sensors In RC-2.

Larger deviations from the conductivity readings (Figure 5.13c) were found when measuring in RC-2 compared with RC-1. However, the maximum error was still acceptable; 393µS/cm at 3h (Table 5.10). The deterioration of the accuracy in RC-2 could be due to the proximity effect when active protozoa swam randomly in the rumen fluid. The field around the electrodes was altered because of the moving conductor (protozoa), leading to measurement uncertainties. Rapid ambient temperature changes ($\pm 3°C$) were observed for RC-2, potentially leading to greater fluctuations. The conductivity of RC-1 (9125µS/cm) was much higher than the conductivity of RC-2 (6174.7µS/cm). As there are very limited reports on the conductivity of rumen fluid, the conductivity from the spot measurements could serve as a basis for future conductivity monitoring of rumen fluid.

With the integrated chip E, spot measurements in RC-3 were performed with 3 sensors E1-E3. The calibration results are in Figure 5.14a, summarized in Table 5.11. The cell constant of chip E (2.83cm^{-1}) was higher than chip A (0.93cm^{-1}), leading to the greater sensitivity slopes for E1-E3. Higher uncertainties were found for chip E, albeit with a low mean error during calibration.

Sensor	Intercept (mV)	Sensitivity (mV/($\Omega \cdot$ cm))	Mean error (%)	Uncertainty (%)	Cell constant (cm^{-1})
E1	-15.03	0.82	-2.0	5.0	2.80
E2	-24.45	0.84	1.0	10.0	2.84

E3	-15.13	0.84	-1.0	5.0	2.84
A6	-1.95	0.32	2.0	2.0	0.96
A10	-2.96	0.31	2.0	2.0	0.93
A11	-3.71	0.31	3.0	7.0	0.89

TABLE 5.11: Summary of calibration results for all conductivity sensors used in RC-3.

Time (h)	Conductivity meter (µS/cm)	E1 (µS/cm)	E2 (µS/cm)	E3 (µS/cm)	Measured conductivity (µS/cm)	Error (µS/cm)	STD (µS/cm)
0	9888.8	9812.3	10348.9	9626.3	9929.1	40.3	375.2
2	9740.2	10124.4	10383.8	9841.4	10116.5	376.4	271.3
4	9825.6	10086.8	10349.6	9747.6	10061.3	235.7	301.8
6	9963.6	10319.3	10217.2	10544.3	10360.3	396.7	167.3

TABLE 5.12: Summary of spot measurement using E1-E3.

Spot measurement results are shown in Table 5.12. The conductivity of RC-3 was close to RC-1 with a difference of less than 1mS/cm. By examining the conductivity of all 3 samples of rumen fluid, it shows that the protozoa make the conductivity lower.

Time (h)	Conductivity meter (µS/cm)	A6 (µS/cm)	A10 (µS/cm)	A11 (µS/cm)	Measured conductivity (µS/cm)	Error (µS/cm)	STD (µS/cm)
0	9964.0	10036.7	10200.7	10282.4	10173.3	209.3	125.1
24	9834.0	9284.0	9761.1	10299.4	9781.5	-52.5	508.0
72	10019.3	9892.1	10474.7	10140.3	10169.0	149.7	292.4
96	10126.6	9773.4	9915.6	10273.7	9987.5	-139.1	257.8
120	10530.0	10309.2	10061.9	10370.9	10247.3	-282.7	163.5
168	9688.6	9991.8	9273.3	10143.4	9802.9	114.3	464.9

TABLE 5.13: Summary of long-term measurement for 3 conductivity sensors in RC-3.

To investigate the long-term sensor performance, 3 sensors (A6, A10, A11) were immersed in RC-3 for 7 days. Calibration data for the 3 sensors are in Figure 5.15a-c. The long-term results in RC-3 are summarized in Table 5.13. The conductivity sensors survived the 7-day period based on daily measurements. No significant deterioration was found due to biofouling. Variation among sensors was dependent on the position in the RC-3 as sediments can lead to different conductivities between the upper side and lower side of the fluid.
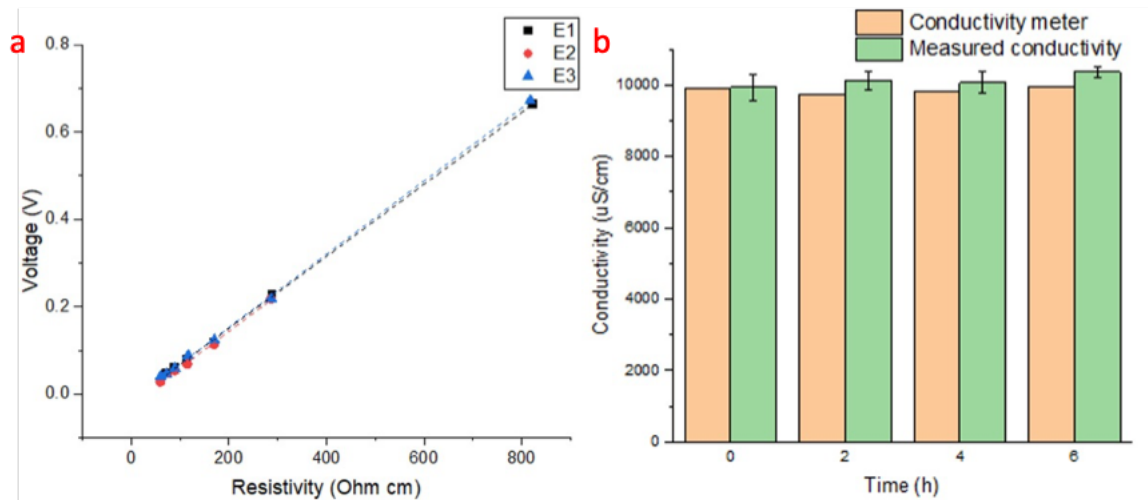
FIGURE 5.14: (a) Calibration results for E1-E3. (b) Spot measurement using E1-E3 in RC-3.
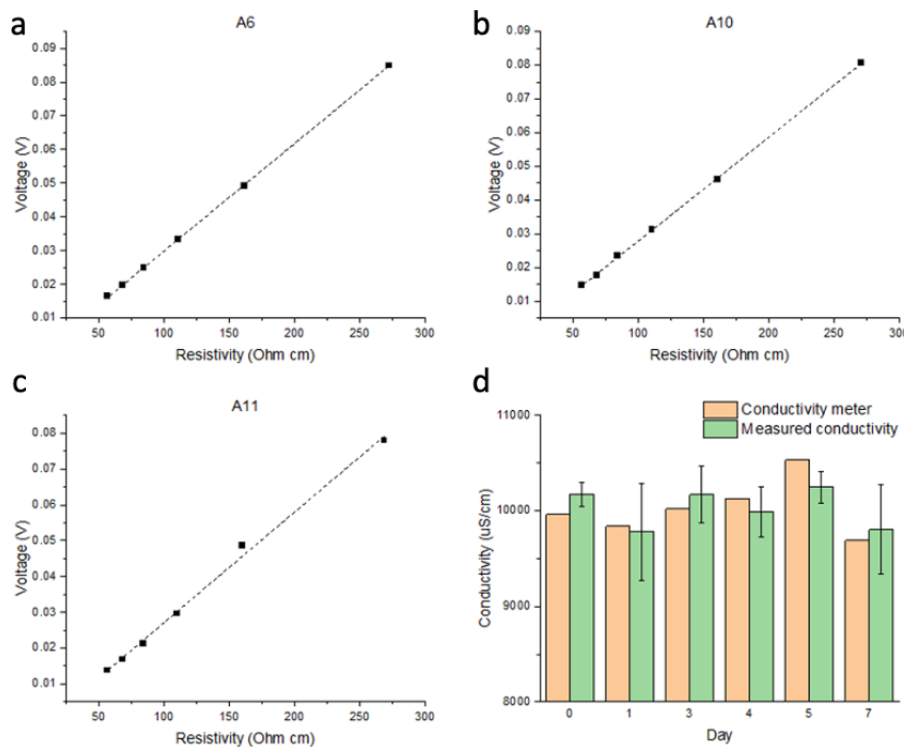
FIGURE 5.15: Calibration results for long-term measurement in RC-3 (a) A6, (b) A10 and (c) A11. (d) Long-term measurements of RC-3 over 7 days.

Therefore, the conductivity sensors had a good performance during in vitro studies with minimal biofouling. This prototype could be further investigated for conducting in vivo experiments for rumen monitoring.

Chapter 6

Conclusions

6.1 Conclusion

This project discusses the need for and development of a novel multi-parameter platform for rumen monitoring. Rumen monitoring is crucial for the alleviation of the global environmental issue and provides one of the most effective ways to evaluate the health of livestock. Important parameters within rumen include pH, ORP, conductivity and DO, enabling the study of metabolism and composition within rumen, as well as promoting feed efficiency and farm management. Prevailing methods require bulky sizes and lengthy procedures. Miniature rumen monitoring platforms only incorporate one or two sensors. It is therefore of great importance to develop different sensors with the aim of real-time measurement in the rumen environment.

In this thesis, RE including QRE and FE-RE, conductivity sensor, pH sensor, ORP sensor and DO sensor were developed based on six types of miniaturized chips (chip A-F). Two types of QREs, which were also Cl^- sensors, were fabricated based on chips B and D, showing near-Nernstian sensitivity for Cl^-. In 0.1M KCl solution, Type 1 QRE was stable for 13 days with negligible drift while Type 2 QRE was stable at least for 2 days. Fast-cure epoxy-based REs were fabricated through Ag/AgCl paste deposition and membrane deposition by mixing 33w/w% or 50w/w% KCl with thinned fast-cure epoxy in a homemade PDMS mould. These REs, especially those containing 50w/w% KCl, exhibited low Cl^- sensitivity (-0.7mV/dec) on the first day. However, the rapid drift over 7-day immersion prevented the REs from long-term monitoring.

The pH sensor was constructed by sputtered RuO_x electrode on the chip. In the range of pH 6.5-8.5, it showed good sensitivity before (-56.1mV/pH) and after (-57.8mV/pH) ETO sterilisation, making the pH sensor promising for sensing when immediate pre-calibration is not feasible. Pt ring electrodes were used for DO sensing with on-chip QRE and CE. The sensor measured the DOC between 1-8mg/L in PBS with decent

accuracy (±1.7%) and theoretical conformity. However, given the LOD of 1mg/L, the detection range of the DO sensor was not suitable for further use in rumen monitoring as an anaerobic condition is typically found in the rumen. The LOD of DO sensor could be further reduced at the expense of larger electrode area or longer response time.

Promising calibration results were achieved for 4-electrode Pt conductivity sensors. Comparable results and accuracy with a commercial conductivity meter were detected in the conductivity range of 1.5-23mS/cm. The high-end limit of detection could be further extended to 49mS/cm for some sensors. Good reproducibility was also observed on 3 consecutive days in the calibration solutions.

ORP sensors delivered reliable voltage outputs in 220mV and 468mV calibration solutions with a maximum deviation of 8mV. The measured ORP in PBS solution was 210.4mV with a longer stabilization time of up to 40mins.

Ex vivo studies for measuring Cl^-, conductivity, pH and ORP have been completed in three rumen samples. The rumen contents were filtered through muslin cloth to extract the rumen fluid which was then aliquoted into falcon tubes for either spot or continuous measurement. For RC-1 and RC-2, an aggregate of 12 conductivity sensors, 13 ORP sensors, 15 pH sensors and 11 Cl^- sensors of two types were microfabricated and calibrated for the ex vivo study. As for RC-3, integrated chips E and F were used to measure conductivity and ORP. Further, the long-term performance of conductivity sensors in the rumen environment was justified in RC-3 with sensors prepared through chips A.

In RC-1, initial Cl^- concentration was between 0.04-0.054M. Whereas, Type 1 QREs suffered decreases in sensitivities due to the loss of the Ag/AgCl layer at the edges of the chips while Type 2 QREs and the Ag/AgCl wires suffered rapid Ag/AgCl degradation in fresh rumen fluid. Spot measurements for pH sensors confirmed the readings from the commercial meters with a deviation <0.14. It was seen from continuous pH detection over 15 hours that the pH declined initially down to 7.36 from 7.47, followed by an increase for 10 hours to 7.62. The sensors were also capable of tracking the manual pH variations within the rumen fluid with excellent accuracy (0.1 pH). ORP sensors did not show stable ORP for at least 10 hours. Average ORPs of -0.099V and -0.123V were collected for RC-1 and RC-2. After continuous measurement for four days in RC-3, an average ORP of -0.07V was achieved. A continuous decrease was found for most sensors before stabilizing because of the long response time in a biofouling environment and oxygen leakage into the solution.

Excellent performance was observed in terms of conductivity sensing. In all three samples, low deviations were detected regardless of the chip configuration. In RC-1 and RC-3 the error was constrained within 3.7% while in RC-2 larger errors were captured as a result of the rapid temperature change and proximity effect due to active protozoa.

Further, the conductivity sensors were capable of delivering accurate measurements after a week, demonstrating minimal influence from the biofouling effect.

To summarize, the developed sensors were able to make accurate measurements in laboratory calibration, as well as in vitro studies of pH, ORP and conductivity. With further investigation and integration, the sensor platform will be a good candidate for in vivo rumen monitoring. The pH and ORP sensors developed with good accuracies are expected to widely contribute to animal health monitoring by distinguishing diseases such as SARA and evaluating the effect of feed. Meanwhile, the nutritional elements and ion activities during the fermentation process will be thoroughly studied through conductivity sensing. By all measures, this project provides a solid basis for rumen monitoring and thus alleviation of GHG emissions.

6.2 Future work

The future work can be divided into two parts – on the sensor side or the system side.

On the sensor side, as the basic functionalities of the sensors have been proven and tested, further improvements are necessary for the intention of higher accuracy and in vivo monitoring. A list of potential improvements is shown below:

- REs with better mechanical stability and long-term stability should be developed. A double junction design could be implemented for the fast-cure epoxy-based RE. Or different polymer membranes (e.g. PVB, PVC) could be attempted.

- Methods should be developed to minimize the influence of biofouling. For instance, an anti-biofouling membrane may be deposited on the electrode surface. Moreover, automated cleaning procedures (e.g. chlorine generation) could be developed to clean the electrodes after each measurement.

- A more sophisticated measurement circuitry towards better accuracy could be developed for the conductivity sensor by a better circuit design using more op-amps and feedback loops.

- DO sensors need a better detection range. Since an electrochemical DO sensor has difficulty measuring at low DOC, a new detection method can be introduced targeting rumen monitoring such as optical sensing protocol.

On the system side, different sensors have been used for the ex vivo study in rumen fluid samples. Whereas to construct a system for real-time measurement, more effects are required on different perspectives listed below:

- The REs and pH sensors did not work properly in integrated chips E and F. New batches of integrated chips should be fabricated with care and thoroughly tested in order to have an integrated chip capable of measuring pH, ORP and conductivity simultaneously.

- Experimental setup for in vitro studies could be improved to minimize the influence of oxygen leakage. For example, a peristaltic pump could be utilized to extract the fresh rumen fluid from the cow for ex vivo measurement instead of manually filtering the rumen fluid.

- Since the signal stimulation, voltage and current measurements have been accomplished by the commercial signal generators and potentiostats. The system would be more flexible and portable for implantation if an electronic platform can be developed on a PCB to interface with the sensors and record the output.

- The power consumption of the entire system should be taken into account for in vivo experiments. Also, proper encapsulation and housing with bio-compatible material should be designed to validate the system.

References

[1] A. Poliquit, "Climate change impacts on livestock production systems: A review," *Annals of Tropical Research*, vol. 189, pp. 148–189, 2014.

[2] S. William W. Kellogg Robert, *Climate change and society: Consequences of increasing atmospheric carbon dioxide*. Routledge, 2018.

[3] P. Gerber, H. Steinfeld, B. Henderson, A. Mottet, C. Opio, J. Dijkman, A. Falcucci, G. Tempio, and FAO, *Tackling climate change through livestock – A global assessment of emissions and mitigation opportunities*. Food and Agriculture Organization of the United Nations (FAO), 2013.

[4] R. J. Wallace, T. J. Snelling, C. A. McCartney, I. Tapio, and F. Strozzi, "Application of meta-omics techniques to understand greenhouse gas emissions originating from ruminal metabolism," *Genetics Selection Evolution*, vol. 49, pp. 1–11, 2017.

[5] S. Schwarzer, R. Witt, and Z. Zommers, "Growing greenhouse gas emissions due to meat production." `https://na.unep.net/geas/archive/pdfs/GEAS_Oct2012_meatproduction.pdf`, 2012. Accessed: 2020-09-30.

[6] S. A. Huws, C. J. Creevey, L. B. Oyama, I. Mizrahi, S. E. Denman, M. Popova, R. Muñoz-Tamayo, E. Forano, S. M. Waters, M. Hess, I. Tapio, H. Smidt, S. J. Krizsan, D. R. Yáñez-Ruiz, A. Belanche, L. Guan, R. J. Gruninger, T. A. McAllister, C. J. Newbold, R. Roehe, R. J. Dewhurst, T. J. Snelling, M. Watson, G. Suen, E. H. Hart, A. H. Kingston-Smith, N. D. Scollan, R. M. D. Prado, E. J. Pilau, H. C. Mantovani, G. T. Attwood, J. E. Edwards, N. R. McEwan, S. Morrisson, O. L. Mayorga, C. Elliott, and D. P. Morgavi, "Addressing global ruminant agricultural challenges through understanding the rumen microbiome: Past, present, and future," *Frontiers in Microbiology*, vol. 9, pp. 1–33, 2018.

[7] E. O'Hara, A. L. Neves, Y. Song, and L. L. Guan, "The role of the gut microbiome in cattle production and health: Driver or passenger?," *Annual Review of Animal Biosciences*, vol. 8, pp. 199–220, 2020.

[8] V. M. Artegoitia, A. P. Foote, R. M. Lewis, and H. C. Freetly, "Rumen fluid metabolomics analysis associated with feed efficiency on crossbred steers," *Scientific Reports*, vol. 7, 2017.

[9] J. B. Russell, "Rumen," *Encyclopedia of Microbiology*, pp. 163–174, 2009.

[10] C. J. Newbold, G. D. la Fuente, A. Belanche, E. Ramos-Morales, and N. R. McEwan, "The role of ciliate protozoa in the rumen," *Frontiers in Microbiology*, vol. 6, pp. 1–14, 2015.

[11] E. S. Kolver and M. J. D. Veth, "Prediction of ruminal ph from pasture-based diets," *Journal of Dairy Science*, vol. 85, 2002.

[12] M. Terré, L. Castells, F. Fàbregas, and A. Bach, "Short communication: Comparison of ph, volatile fatty acids, and microbiome of rumen samples from preweaned calves obtained via cannula or stomach tube," *Journal of Dairy Science*, vol. 96, 2013.

[13] J. A. Laporte-Uribe, "The role of dissolved carbon dioxide in both the decline in rumen ph and nutritional diseases in ruminants," *Animal Feed Science and Technology*, vol. 219, pp. 268–279, 2016.

[14] J. C. Plaizier, D. O. Krause, G. N. Gozho, and B. W. McBride, "Subacute ruminal acidosis in dairy cows: The physiological causes, incidence and consequences," *Veterinary Journal*, 2008.

[15] J. A. Basarab, K. A. Beauchemin, V. S. Baron, K. H. Ominski, L. L. Guan, S. P. Miller, and J. J. Crowley, "Reducing ghg emissions through genetic improvement for feed efficiency: effects on economically important traits and enteric methane production.," *Animal : an international journal of animal bioscience*, 2013.

[16] R. Cooper, T. J. Klopfenstein, R. Stock, C. Parrott, D. Herold, R. . Cooper, T. J. . Klopfenstein, R. . Stock, C. . Parrott, H. Dan, . Effect, T. Klopfenstein, and D. Herold', "Effect of rumensin and feed intake variation on ruminal ph," *Nebraska Beef Cattle Reports*, p. 430, 1997.

[17] O. Husson, "Redox potential (eh) and ph as drivers of soil/plant/microorganism systems: A transdisciplinary overview pointing to integrative opportunities for agronomy," *Plant and Soil*, vol. 362, pp. 389–417, 2013.

[18] E. Pinloche, N. McEwan, J. P. Marden, C. Bayourthe, E. Auclair, and C. J. Newbold, "The effects of a probiotic yeast on the bacterial diversity and population structure in the rumen of cattle," *PLoS ONE*, vol. 8, 2013.

[19] E. M. Ungerfeld, "Metabolic hydrogen flows in rumen fermentation: Principles and possibilities of interventions," *Frontiers in Microbiology*, vol. 11, 2020.

[20] H. V. Scheller and P. Ulvskov, "Hemicelluloses," *Annual Review of Plant Biology*, vol. 61, pp. 263–289, 2010.

[21] Y. Huang, J. P. Marden, C. Julien, and C. Bayourthe, "Redox potential: An intrinsic parameter of the rumen environment," *Journal of Animal Physiology and Animal Nutrition*, vol. 102, pp. 393–402, 4 2018.

[22] J. Dijkstra, S. V. Gastelen, K. Dieho, K. Nichols, and A. Bannink, "Review: Rumen sensors: Data and interpretation for key rumen metabolic processes," *Animal*, vol. 14, pp. S176–S186, 2020.

[23] E. Humer, J. R. Aschenbach, V. Neubauer, I. Kröger, R. Khiaosa-ard, W. Baumgartner, and Q. Zebeli, "Signals for identifying cows at risk of subacute ruminal acidosis in dairy veterinary practice," *Journal of Animal Physiology and Animal Nutrition*, vol. 102, pp. 380–392, 2018.

[24] R. Antanaitis, V. Žilaitis, A. Kučinskas, V. Juozaitiene, and K. Leonauskaite, "Changes in cow activity, milk yield, and milk conductivity before clinical diagnosis of ketosis, and acidosis," *Veterinarija ir Zootechnika*, vol. 70, pp. 3–9, 2015.

[25] A. C. Warner and B. D. Stacy, "Solutes in the rumen of the sheep," *Quarterly Journal of Experimental Physiology and Cognate Medical Sciences*, vol. 50, pp. 169–184, 1965.

[26] W. Peñafiel and D. Ticona, "Elementos nutricionales en la producción de fertilizante biol con diferentes tipos de insumos y cantidades de contenido ruminal de bovino - matadero municipal de la paz," *Revista de Investigación e Innovación Agropecuaria y de Recursos Naturales*, vol. 2, 2015.

[27] M. Futagawa, M. Ishida, M. Ishida, and K. Sawada, "Study of a wireless multimodal sensing system integrated with an electrical conductivity sensor and a temperature sensor for the health control of cows," *IEEJ Transactions on Electrical and Electronic Engineering*, vol. 6, pp. 93–96, 2011.

[28] R. I. Scott, N. Yarlett, K. Hillman, A. G. Williams, D. Lloyd, and T. N. Williams, "The presence of oxygen in rumen liquor and its effects on methanogenesis," *Journal of Applied Bacteriology*, vol. 55, 1983.

[29] J. R. Knapp, G. L. Laur, P. A. Vadas, W. P. Weiss, and J. M. Tricarico, "Invited review: Enteric methane in dairy cattle production: Quantifying the opportunities and impact of reducing emissions," *Journal of Dairy Science*, 2014.

[30] M. Clark and D. Tilman, "Comparative analysis of environmental impacts of agricultural production systems, agricultural input efficiency, and food choice," *Environmental Research Letters*, vol. 12, 2017.

[31] E. F. Garrett, M. N. Pereira, K. V. Nordlund, L. E. Armentano, W. J. Goodger, and G. R. Oetzel, "Diagnostic methods for the detection of subacute ruminal acidosis in dairy cows," *Journal of Dairy Science*, vol. 82, 1999.

[32] T. Geishauser, N. Linhart, A. Neidl, and A. Reimann, "Factors associated with ruminal ph at herd level," *Journal of Dairy Science*, vol. 95, 2012.

[33] P. J. Kononoff, A. J. Heinrichs, and H. A. Lehman, "The effect of corn silage particle size on eating behavior, chewing activities, and rumen fermentation in lactating dairy cows," *Journal of Dairy Science*, vol. 86, 2003.

[34] G. B. Penner, K. A. Beauchemin, and T. Mutsvangwa, "An evaluation of the accuracy and precision of a stand-alone submersible continuous ruminal ph measurement system," *Journal of Dairy Science*, vol. 89, 2006.

[35] C. Qin, D. Bu, P. Sun, X. Zhao, P. Zhang, and J. Wang, "Effects of corn straw or mixed forage diet on rumen fermentation parameters of lactating cows using a wireless data logger," *Animal Science Journal*, vol. 88, 2017.

[36] K. Dieho, J. Dijkstra, J. T. Schonewille, and A. Bannink, "Changes in ruminal volatile fatty acid production and absorption rate during the dry period and early lactation as affected by rate of increase of concentrate allowance," *Journal of Dairy Science*, vol. 99, pp. 5370–5384, 2016.

[37] C. S. Han, U. Kaur, H. Bai, B. R. dos Reis, R. White, R. A. Nawrocki, R. M. Voyles, M. G. Kang, and S. Priya, "Invited review: Sensor technologies for real-time monitoring of the rumen environment," *Journal of Dairy Science*, vol. 105, pp. 6379–6404, 2022.

[38] E. Humer, K. Ghareeb, H. Harder, E. Mickdam, A. Khol-Parisini, and Q. Zebeli, "Peripartal changes in reticuloruminal ph and temperature in dairy cows differing in the susceptibility to subacute rumen acidosis," *Journal of Dairy Science*, vol. 98, pp. 8788–8799, 2015.

[39] J. P. Marden, C. Bayourthe, F. Enjalbert, and R. Moncoulon, "A new device for measuring kinetics of ruminal ph and redox potential in dairy cattle," *Journal of Dairy Science*, vol. 88, 2005.

[40] B. T. Seaton, D. F. Hill, S. L. Cowen, and M. L. Heien, "Mitigating the effects of electrode biofouling-induced impedance for improved long-term electrochemical measurements in vivo," *Analytical Chemistry*, vol. 92, 2020.

[41] T. Feng, W. Ji, Q. Tang, H. Wei, S. Zhang, J. Mao, Y. Zhang, L. Mao, and M. Zhang, "Low-fouling nanoporous conductive polymer-coated microelectrode for in vivo monitoring of dopamine in the rat brain," *Analytical Chemistry*, vol. 91, 2019.

[42] D. Chan, J. C. Chien, E. Axpe, L. Blankemeier, S. W. Baker, S. Swaminathan, V. A. Piunova, D. Y. Zubarev, C. L. Maikawa, A. K. Grosskopf, J. L. Mann, H. T. Soh, and E. A. Appel, "Combinatorial polyacrylamide hydrogels for preventing biofouling on implantable biosensors," *bioRxiv*, 2020.

[43] M. Sophocleous and J. K. Atkinson, "A review of screen-printed silver/silver chloride (ag/agcl) reference electrodes potentially suitable for environmental potentiometric sensors," *Sensors and Actuators, A: Physical*, vol. 267, pp. 106–120, 2017.

[44] U. Guth, F. Gerlach, M. Decker, W. Oelßner, and W. Vonau, "Solid-state reference electrodes for potentiometric sensors," *Journal of Solid State Electrochemistry*, vol. 13, pp. 27–39, 2009.

[45] M. W. Shinwari, D. Zhitomirsky, I. A. Deen, P. R. Selvaganapathy, M. J. Deen, and D. Landheer, "Microfabricated reference electrodes and their biosensing applications," *Sensors*, vol. 10, pp. 1679–1715, 2010.

[46] F. Scholz, "Electroanalytical methods: Guide to experiments and applications," *Electroanalytical Methods: Guide to Experiments and Applications*, pp. 1–359, 2010.

[47] A. Simonis, H. Lüth, J. Wang, and M. J. Schöning, "Strategies of miniaturised reference electrodes integrated in a silicon based "one chip" ph sensor," *Sensors*, vol. 3, pp. 330–339, 2003.

[48] J. Ha, S. M. Martin, Y. Jeon, J. Y. In, R. B. Brown, H. Nam, and S. C. Geun, "A polymeric junction membrane for solid-state reference electrodes," *Analytica Chimica Acta*, vol. 549, pp. 59–66, 2005.

[49] W. Y. Liao and T. C. Chou, "Fabrication of a planar-form screen-printed solid electrolyte modified ag/agcl reference electrode for application in a potentiometric biosensor," *Analytical Chemistry*, vol. 78, pp. 4219–4223, 2006.

[50] I. Y. Huang, R. S. Huang, and L. H. Lo, "Improvement of integrated ag/agcl thin-film electrodes by kcl-gel coating for isfet applications," *Sensors and Actuators, B: Chemical*, vol. 94, pp. 53–64, 2003.

[51] S. M. Bidoki, D. M. Lewis, M. Clark, A. Vakorov, P. A. Millner, and D. McGorman, "Ink-jet fabrication of electronic components," *Journal of Micromechanics and Microengineering*, vol. 17, pp. 967–974, 2007.

[52] C. Dumschat, M. Borchardt, C. Diekmann, K. Cammann, and M. Knoll, "Potentiometric test strip," *Sensors and Actuators: B. Chemical*, vol. 24, pp. 279–281, 1995.

[53] A. W. Cranny and J. K. Atkinson, "Thick film silver-silver chloride reference electrodes," *Measurement Science and Technology*, vol. 9, pp. 1557–1565, 1998.

[54] A. Lewenstam, B. Bartoszewicz, J. Migdalski, and A. Kochan, "Solid contact reference electrode with a pvc-based composite electroactive element fabricated by 3d printing," *Electrochemistry Communications*, vol. 109, p. 106613, 2019.

[55] Łukasz Tymecki, E. Zwierkowska, and R. Koncki, "Screen-printed reference electrodes for potentiometric measurements," *Analytica Chimica Acta*, vol. 526, pp. 3–11, 2004.

[56] J. K. Atkinson, M. Glanc, P. Boltryk, M. Sophocleous, and E. Garcia-Breijo, "An investigation into the effect of fabrication parameter variation on the characteristics of screen-printed thick-film silver/silver chloride reference electrodes," *Microelectronics International*, vol. 28, pp. 49–52, 2011.

[57] M. Sophocleous, M. Glanc-Gostkiewicz, J. K. Atkinson, and E. Garcia-Breijo, "An experimental analysis of thick-film solid-state reference electrodes," *Proceedings of IEEE Sensors*, pp. 12–15, 2012.

[58] R. Mamińska, A. Dybko, and W. Wróblewski, "All-solid-state miniaturised planar reference electrodes based on ionic liquids," *Sensors and Actuators, B: Chemical*, vol. 115, pp. 552–557, 2006.

[59] Z. Mousavi, K. Granholm, T. Sokalski, and A. Lewenstam, "An analytical quality solid-state composite reference electrode," *Analyst*, vol. 138, pp. 5216–5220, 2013.

[60] T. Guinovart, G. A. Crespo, F. X. Rius, and F. J. Andrade, "A reference electrode based on polyvinyl butyral (pvb) polymer for decentralized chemical measurements," *Analytica Chimica Acta*, vol. 821, pp. 72–80, 2014.

[61] Q. Li, W. Tang, Y. Su, Y. Huang, S. Peng, B. Zhuo, S. Qiu, L. Ding, Y. Li, and X. Guo, "Stable thin-film reference electrode on plastic substrate for all-solid-state ion-sensitive field-effect transistor sensing system," *IEEE Electron Device Letters*, vol. 38, pp. 1469–1472, 2017.

[62] A. Moya, R. Pol, A. Martínez-Cuadrado, R. Villa, G. Gabriel, and M. Baeza, "Stable full-inkjet-printed solid-state ag/agcl reference electrode," *Analytical Chemistry*, vol. 91, pp. 15539–15546, 2019.

[63] D. Stoica, P. J. Brewer, R. J. Brown, and P. Fisicaro, "Influence of fabrication procedure on the electrochemical performance of ag/agcl reference electrodes," *Electrochimica Acta*, vol. 56, pp. 10009–10015, 2011.

[64] B. J. Polk, A. Stelzenmuller, G. Mijares, W. MacCrehan, and M. Gaitan, "Ag/agcl microelectrodes with improved stability for microfluidics," *Sensors and Actuators, B: Chemical*, vol. 114, pp. 239–247, 2006.

[65] A. Kisiel, H. Marcisz, A. Michalska, and K. Maksymiuk, "All-solid-state reference electrodes based on conducting polymers," *Analyst*, vol. 130, pp. 1655–1662, 2005.

[66] F. X. Rius-Ruiz, A. Kisiel, A. Michalska, K. Maksymiuk, J. Riu, and F. X. Rius, "Solid-state reference electrodes based on carbon nanotubes and polyacrylate membranes," *Analytical and Bioanalytical Chemistry*, vol. 399, pp. 3613–3622, 2011.

[67] J. Hu, A. Stein, and P. Bühlmann, "Rational design of all-solid-state ion-selective electrodes and reference electrodes," *TrAC - Trends in Analytical Chemistry*, vol. 76, pp. 102–114, 2016.

[68] D. Cicmil, S. Anastasova, A. Kavanagh, D. Diamond, U. Mattinen, J. Bobacka, A. Lewenstam, and A. Radu, "Ionic liquid-based, liquid-junction-free reference electrode," *Electroanalysis*, vol. 23, pp. 1881–1890, 2011.

[69] A. Kisiel, K. Kijewska, M. Mazur, K. Maksymiuk, and A. Michalska, "Polypyrrole microcapsules in all-solid-state reference electrodes," *Electroanalysis*, vol. 24, pp. 165–172, 2012.

[70] H. Xu, Y. Pan, Y. Wang, G. Li, Y. Chen, and Y. Ye, "An all-solid-state screen-printed carbon paste reference electrode based on poly(3,4-ethylenedioxythiophene) as solid contact transducer," *Measurement Science and Technology*, vol. 23, 2012.

[71] M. S. Lesney, "A basic history of acid - from aristotle to arnold," *Today's Chemist at Work*, 2003.

[72] W. Vonau and U. Guth, "ph monitoring: A review," *Journal of Solid State Electrochemistry*, vol. 10, pp. 746–752, 2006.

[73] D. Wencel, T. Abel, and C. McDonagh, "Optical chemical ph sensors," *Analytical Chemistry*, vol. 86, 2014.

[74] A. J. Marshall, J. Blyth, C. A. Davidson, and C. R. Lowe, "ph-sensitive holographic sensors," *Analytical Chemistry*, vol. 75, 2003.

[75] S. W. Bishnoi, C. J. Rozell, C. S. Levin, M. K. Gheith, B. R. Johnson, D. H. Johnson, and N. J. Halas, "All-optical nanoscale ph meter," *Nano Letters*, vol. 6, 2006.

[76] M. T. Ghoneim, A. Nguyen, N. Dereje, J. Huang, G. C. Moore, P. J. Murzynowski, and C. Dagdeviren, "Recent progress in electrochemical ph-sensing materials and configurations for biomedical applications," *Chemical Reviews*, vol. 119, 2019.

[77] P. T. Kerridge, "The use of the glass electrode in biochemistry," *Biochemical Journal*, vol. 19, 1925.

[78] Chris Cushman, "Parts of a pH probe." https://www.ysi.com/ysi-blog/water-blogged-blog/2019/02/anatomy-of-ph-electrodes?mkt_tok=eyJpIjoiWVdGbE5HRXlZVFZsWVRjeSIsInQiOiJLakJXRnVkS1lnVm1ISk1JbVZ4aVMycmhHdzZWZ1p3 3D%3D, 2019. Accessed: 2021-07-08.

[79] T. Lindfors, S. Ervelä, and A. Ivaska, "Polyaniline as ph-sensitive component in plasticized pvc membranes," *Journal of Electroanalytical Chemistry*, vol. 560, 2003.

[80] T. Guinovart, G. Valdés-Ramírez, J. R. Windmiller, F. J. Andrade, and J. Wang, "Bandage-based wearable potentiometric sensor for monitoring wound ph," *Electroanalysis*, vol. 26, 2014.

[81] J. H. Yoon, S. B. Hong, S. O. Yun, S. J. Lee, T. J. Lee, K. G. Lee, and B. G. Choi, "High performance flexible ph sensor based on polyaniline nanopillar array electrode," *Journal of Colloid and Interface Science*, vol. 490, pp. 53–58, 2017.

[82] K. Santiago and B. AJ, "Electrochemically synthesized polymer-based ph sensors," *Philipp J Sci*, vol. 128, p. 120–126, 1999.

[83] O. Korostynska, K. Arshak, E. Gill, and A. Arshak, "Review on state-of-the-art in polymer based ph sensors," *Sensors*, vol. 7, 2007.

[84] L. Manjakkal, D. Szwagierczak, and R. Dahiya, "Metal oxides based electrochemical ph sensors: Current progress and future perspectives," *Progress in Materials Science*, vol. 109, 2020.

[85] J. A. Mihell and J. K. Atkinson, "Planar thick-film ph electrodes based on ruthenium dioxide hydrate," *Sensors and Actuators, B: Chemical*, vol. 48, 1998.

[86] T. Katsube, I. Lauks, and J. N. Zemel, "ph-sensitive sputtered iridium oxide films," *Sensors and Actuators*, vol. 2, pp. 399–410, 1981.

[87] K. Kreider, "Iridium oxide thin-film stability in high-temperature corrosive solutions," *Sensors and Actuators: B. Chemical*, vol. 5, 1991.

[88] K. Nishio and T. Tsuchiya, "Electrochromic thin films prepared by sol-gel process," *Solar Energy Materials and Solar Cells*, vol. 68, 2001.

[89] M. Wang, S. Yao, and M. Madou, "A long-term stable iridium oxide ph electrode," *Sensors and Actuators, B: Chemical*, vol. 81, pp. 313–315, 2002.

[90] K. Yamanaka, "Anodically electrodeposited iridium oxide films (aeirof) from alkaline solutions for electrochromic display devices," *Japanese Journal of Applied Physics*, vol. 28, 1989.

[91] S. A. Marzouk, S. Ufer, R. P. Buck, T. A. Johnson, L. A. Dunlap, and W. E. Cascio, "Electrodeposited iridium oxide ph electrode for measurement of extracellular myocardial acidosis during acute ischemia," *Analytical Chemistry*, vol. 70, 1998.

[92] H. J. Chung, M. S. Sulkin, J. S. Kim, C. Goudeseune, H. Y. Chao, J. W. Song, S. Y. Yang, Y. Y. Hsu, R. Ghaffari, I. R. Efimov, and J. A. Rogers, "Stretchable, multiplexed ph sensors with demonstrations on rabbit and human hearts undergoing ischemia," *Advanced Healthcare Materials*, vol. 3, 2014.

[93] W. D. Huang, H. Cao, S. Deb, M. Chiao, and J. C. Chiao, "A flexible ph sensor based on the iridium oxide sensing film," *Sensors and Actuators, A: Physical*, vol. 169, pp. 1–11, 2011.

[94] Y. H. Liao and J. C. Chou, "Preparation and characteristics of ruthenium dioxide for ph array sensors with real-time measurement system," *Sensors and Actuators, B: Chemical*, vol. 128, pp. 603–612, 2008.

[95] W. Lonsdale, M. Wajrak, and K. Alameh, "Manufacture and application of ruo2 solid-state metal-oxide ph sensor to common beverages," *Talanta*, vol. 180, pp. 277–281, 2018.

[96] R. Martínez-Máñez, J. Soto, E. García-Breijo, L. Gil, J. Ibáñez, and E. Gadea, "A multisensor in thick-film technology for water quality control," *Sensors and Actuators, A: Physical*, vol. 120, pp. 589–595, 2005.

[97] L. Manjakkal, K. Cvejin, J. Kulawik, K. Zaraska, and D. Szwagierczak, "A comparative study of potentiometric and conductimetric thick film ph sensors made of ruo2 pastes," *Sensor Letters*, vol. 12, 2014.

[98] L. Manjakkal, K. Cvejin, J. Kulawik, K. Zaraska, and D. Szwagierczak, "A low-cost ph sensor based on ruo¡sub¿2¡/sub¿ resistor material," *Nano Hybrids*, vol. 5, 2013.

[99] R. H. Mingels, S. Kalsi, Y. Cheong, and H. Morgan, "Iridium and ruthenium oxide miniature ph sensors: Long-term performance," *Sensors and Actuators, B: Chemical*, vol. 297, p. 126779, 2019.

[100] S. M. Al-Hilli, R. T. Al-Mofarji, and M. Willander, "Zinc oxide nanorod for intracellular ph sensing," *Applied Physics Letters*, vol. 89, pp. 87–90, 2006.

[101] E. Tanumihardja, W. Olthuis, and A. van den Berg, "Ruthenium oxide ph sensing for organs-on-chip studies," *Proceedings*, vol. 2, p. 709, 2018.

[102] C. A. Li, K. N. Han, X. H. Pham, and G. H. Seong, "A single-walled carbon nanotube thin film-based ph-sensing microfluidic chip," *Analyst*, vol. 139, pp. 2011–2015, 2014.

[103] Y. Qin, H. J. Kwon, A. Subrahmanyam, M. M. Howlader, P. R. Selvaganapathy, A. Adronov, and M. J. Deen, "Inkjet-printed bifunctional carbon nanotubes for ph sensing," *Materials Letters*, vol. 176, pp. 68–70, 2016.

[104] F. van Rossem, J. G. Bomer, H. L. de Boer, Y. Abbas, E. de Weerd, A. van den Berg, and S. L. Gac, "Sensing oxygen at the millisecond time-scale using an ultra-microelectrode array (umea)," *Sensors and Actuators, B: Chemical*, vol. 238, pp. 1008–1016, 2017.

[105] J. H. Carpenter, "The accuracy of the winkler method for dissolved oxygen analysis," *Limnology and Oceanography*, vol. 10, pp. 135–140, 1965.

[106] G. Knowles and G. F. Lowden, "Methods for detecting the end-point in the titration of iodine with thiosulphate," *The Analyst*, vol. 78, pp. 159–164, 1953.

[107] Z. Zhang, Z. Chen, F. Cheng, Y. Zhang, and L. Chen, "Iodine-mediated etching of gold nanorods for plasmonic sensing of dissolved oxygen and salt iodine," *Analyst*, vol. 141, pp. 2955–2961, 2016.

[108] Z. Qiao, Z. Wang, C. Zhang, S. Yuan, Y. Zhu, and J. Wang, "Pvam–pip/ps composite membrane with high performance for co2/n2 separation," *AIChE Journal*, vol. 59, pp. 215–228, 2012.

[109] Q. Wang, J. M. Zhang, and S. Li, "Minreview: Recent advances in the development of gaseous and dissolved oxygen sensors," *Instrumentation Science and Technology*, vol. 47, pp. 19–50, 2019.

[110] J. Park, J. H. Chang, M. Choi, J. J. Pak, D. Y. Lee, and Y. K. Pak, "Microfabirated clark-type sensor for measuing dissolved oxygen," *Proceedings of IEEE Sensors*, pp. 1412–1415, 2007.

[111] K. Takahashi, "Catheter type long-life miniature oxygen sensor," *Japanese Journal of Medical Electronics and Biological Engineering*, vol. 39, pp. 37–41, 2001.

[112] I. Shitanda, S. Mori, and M. Itagaki, "Screen-printed dissolved oxygen sensor based on cerium oxide-supported silver catalyst and polydimethylsiloxane film," *Analytical Sciences*, vol. 27, pp. 1049–1052, 2011.

[113] L. Nei and R. G. Compton, "An improved clark-type galvanic sensor for dissolved oxygen," *Sensors and Actuators, B: Chemical*, vol. 30, pp. 83–87, 1996.

[114] L. Hsu, P. R. Selvaganapathy, J. Brash, Q. Fang, C. Q. Xu, M. J. Deen, and H. Chen, "Development of a low-cost hemin-based dissolved oxygen sensor with anti-biofouling coating for water monitoring," *IEEE Sensors Journal*, vol. 14, pp. 3400–3407, 2014.

[115] A. J. Hsueh, S. Park, T. Satoh, T. Shimizu, K. Koiwai, M. Nakashima, Y. Morimoto, M. Kinoshita, and H. Suzuki, "Microdevice with an integrated clark-type oxygen electrode for the measurement of the respiratory activity of cells," *Analytical Chemistry*, vol. 93, pp. 5577–5585, 2021.

[116] L. Rivas, S. Dulay, S. Miserere, L. Pla, S. B. Marin, J. Parra, E. Eixarch, E. Gratacós, M. Illa, M. Mir, and J. Samitier, "Micro-needle implantable electrochemical oxygen sensor: ex-vivo and in-vivo studies," *Biosensors and Bioelectronics*, vol. 153, 2020.

[117] N. J. Finnerty and F. B. Bolger, "In vitro development and in vivo application of a platinum-based electrochemical device for continuous measurements of peripheral tissue oxygen," *Bioelectrochemistry*, vol. 119, pp. 124–135, 2018.

[118] J. R. Marland, M. E. Gray, D. J. Argyle, I. Underwood, A. F. Murray, and M. A. Potter, "Post-operative monitoring of intestinal tissue oxygenation using an implantable microfabricated oxygen sensor," *Micromachines*, vol. 12, 2021.

[119] J. R. Marland, M. E. Gray, C. Dunare, E. O. Blair, A. Tsiamis, P. Sullivan, E. González-Fernández, S. N. Greenhalgh, R. Gregson, R. E. Clutton, M. M. Parys, A. Dyson, M. Singer, I. H. Kunkler, M. A. Potter, S. Mitra, J. G. Terry, S. Smith, A. R. Mount, I. Underwood, A. J. Walton, D. J. Argyle, and A. F. Murray, "Real-time measurement of tumour hypoxia using an implantable microfabricated oxygen sensor," *Sensing and Bio-Sensing Research*, vol. 30, p. 100375, 2020.

[120] W.-C. Lin, K. Brondum, C. Monroe, and M. Burns, "Multifunctional water sensors for ph, orp, and conductivity using only microfabricated platinum electrodes," *Sensors*, vol. 17, p. 1655, 7 2017.

[121] M. Yamin, W. I. B. W. Ismail, M. S. B. M. Kassim, S. B. A. Aziz, R. Shamshiri, F. N. Akbar, and M. Ibrahim, "Development and calibration of orp sensor for the estimation of macronutrients in the soil of oil palm plantation," *Pakistan Journal of Agricultural Sciences*, vol. 57, pp. 1363–1369, 2020.

[122] S. Putney, A. H. Theiss, N. K. Rajan, E. Deak, C. Buie, Y. Ngo, H. Shah, V. Yuan, E. Botbol-Ponte, A. Hoyos-Urias, O. Knopfmacher, C. A. Hogan, N. Banaei, and M. S. Herget, "Novel electronic biosensor for automated inoculum preparation to accelerate antimicrobial susceptibility testing," *Scientific Reports*, vol. 11, 2021.

[123] P. L. Bishop and T. Yu, "A microelectrode study of redox potential change in biofilms," *Water Science and Technology*, vol. 39, pp. 179–185, 1999.

[124] J. M. Steininger and C. Pareja, "Orp sensor response in chlorinated water," *NSPI Symposium Series*, vol. I, pp. 1–9, 1996.

[125] J. H. Lee, A. Jang, P. R. Bhadri, R. R. Myers, W. Timmons, F. R. Beyette, P. L. Bishop, and I. Papautsky, "Fabrication of microelectrode arrays for in situ sensing of oxidation reduction potentials," *Sensors and Actuators, B: Chemical*, vol. 115, pp. 220–226, 2006.

[126] K. Striggow and R. Dankert, "The exact theory of inductive conductivity sensors for oceanographic application," *IEEE Journal of Oceanic Engineering*, vol. 10, pp. 175–179, 1985.

[127] S. P. Natarajan, J. Huffman, T. M. Weller, and D. P. Fries, "Contact-less toroidal fluid conductivity sensor based on rf detection," *Proceedings of IEEE Sensors*, vol. 1, pp. 304–307, 2004.

[128] G. Jones and S. M. Christian, "The measurement of the conductance of electrolytes. vi. galvanic polarization by alternating current," *Journal of the American Chemical Society*, vol. 57, 1935.

[129] Z. Moroń, "Investigations of van der pauw method applied for measuring electrical conductivity of electrolyte solutions: Measurement of electrolytic conductivity," *Measurement: Journal of the International Measurement Confederation*, vol. 33, 2003.

[130] B. Zhang, Z. Lin, X. Zhang, X. Yu, J. Wei, and X. Wang, "System for absolute measurement of electrolytic conductivity in aqueous solutions based on van der pauw's theory," *Measurement Science and Technology*, vol. 25, 2014.

[131] C. Thirstrup and L. Deleebeeck, "Review on electrolytic conductivity sensors," *IEEE Transactions on Instrumentation and Measurement*, vol. 70, pp. 1–22, 2021.

[132] C. S. Rustomji, J. Mac, C. Choi, T. K. Kim, D. Choi, Y. S. Meng, and S. Jin, "Thin-film electrochemical sensor electrode for rapid evaluation of electrolytic conductivity, cyclic voltammetry, and temperature measurements," *Journal of Applied Electrochemistry*, vol. 46, pp. 59–67, 2016.

[133] B. Timmer, W. Sparreboom, W. Olthuis, P. Bergveld, and A. V. den Berg, "Optimization of an electrolyte conductivity detector for measuring low ion concentrations," *Lab on a Chip*, vol. 2, pp. 121–124, 2002.

[134] Y. L. Tan and C. E. Chong, "Resistivity measurement of a small-volume sample using two planar disc electrodes and a new geometric factor," *IEEE Sensors Journal*, vol. 8, pp. 516–521, 2008.

[135] G. J. A. M. Brom-Verheijden, M. H. Goedbloed, and M. A. G. Zevenbergen, "A microfabricated 4-electrode conductivity sensor with enhanced range," *MDPI proceedings*, p. 797, 2018.

[136] M. Lampila, "Preliminary studies on the variations of ph and volatile fatty acid concentration of the rumen contents of the cow," *Agricultural and Food Science*, vol. 27, pp. 143–153, 1955.

[137] T. Duffield, J. C. Plaizier, A. Fairfield, R. Bagg, G. Vessie, P. Dick, J. Wilson, J. Aramini, and B. McBride, "Comparison of techniques for measurement of rumen ph in lactating dairy cows," *Journal of Dairy Science*, vol. 87, pp. 59–66, 2004.

[138] T. Mottram, "Automatic monitoring of the health and metabolic status of dairy cows," *Livestock Production Science*, vol. 48, pp. 209–217, 1997.

[139] S. Sato, H. Mizuguchi, K. Ito, K. Ikuta, A. Kimura, and K. Okada, "Technical note: Development and testing of a radio transmission ph measurement system

for continuous monitoring of ruminal ph in cows," *Preventive Veterinary Medicine*, vol. 103, pp. 274–279, 2012.

[140] A. Castro-Costa, A. A. Salama, X. Moll, J. Aguiló, and G. Caja, "Using wireless rumen sensors for evaluating the effects of diet and ambient temperature in non-lactating dairy goats," *Journal of Dairy Science*, vol. 98, pp. 4646–4658, 2015.

[141] L. Zhang, J. Lu, H. Okada, H. Nogami, T. Itoh, and S. Arai, "Low-power highly sensitive ph sensor with μdots protective structures for monitoring rumen in cows in real-time," *IEEE Sensors Journal*, vol. 17, pp. 7281–7289, 2017.

[142] C. Julien, J.-P. Marden, A. Troegeler-Meynadier, and C. Bayourthe, "Methodology article: Can ruminal reducing power assessed in batch cultures be comparable to in vivo measurements?," *Journal of Analytical Sciences, Methods and Instrumentation*, vol. 04, pp. 80–86, 2014.

[143] M. Richter, L. Křížová, and J. Třináctý, "The effect of individuality of animal on diurnal pattern of ph and redox potential in the rumen of dry cows," *Czech Journal of Animal Science*, vol. 55, pp. 401–407, 2010.

[144] A. Amiri, H. Zare-Zardini, M. Shanbedi, S. N. Kazi, A. Taheri-Kafrani, B. T. Chew, and A. Zarrabi, "Microbial toxicity of different functional groups-treated carbon nanotubes," *Surface Chemistry of Nanobiomaterials*, pp. 33–70, 2016.

[145] Z. Lewandowski and H. Beyenal, *Fundamentals of Biofilm Research*. CRC Press, dec 2013.

[146] A. N. Raditya and D. O'Hare, "Review—electrochemical sensor biofouling in environmental sensor networks: Characterisation, remediation and lessons from biomedical devices," *Journal of The Electrochemical Society*, vol. 167, 2020.

[147] S. Baltsavias, W. V. Treuren, M. Weber, J. Charthad, S. Baker, J. L. Sonnenburg, and A. Arbabian, "In vivo wireless sensors for gut microbiome redox monitoring," *IEEE Transactions on Biomedical Engineering*, vol. 9294, pp. 1–11, 2019.

[148] B. T. Seaton and M. L. Heien, "Biocompatible reference electrodes to enhance chronic electrochemical signal fidelity in vivo," *Analytical and Bioanalytical Chemistry*, vol. 413, pp. 6689–6701, 2021.

[149] X. Huang, *IN-SITU CONDUCTIVITY, TEMPERATURE, AND DISSOLVED OXYGEN (CT-DO) SENSOR SYSTEM FOR MARINE MEASUREMENT*. PhD thesis, University of Southampton, 2011.

[150] "Electrical double-layer formation part 1 (nanotechnology)." http://what-when-how.com/nanoscience-and-nanotechnology/electrical-double-layer-formation-part-1-nanotechnology/. Accessed: 2020-09-05.

[151] M. Koudelka, "Performance characteristics of a planar 'clark-type' oxygen sensor," *Sensors and Actuators*, vol. 9, pp. 249–258, 1986.

[152] A. M. Bond and S. W. Feldberg, "Analysis of simulated reversible cyclic voltammetric responses for a charged redox species in the absence of added electrolyte," *Journal of Physical Chemistry B*, vol. 102, 1998.

[153] E. M. Hudak, *ELECTROCHEMICAL EVALUATION OF PLATINUM AND DIAMOND ELECTRODES FOR NEURAL STIMULATION.* PhD thesis, Case Western Reserve University, 2011.

[154] R. Mingels, *Development of a multi-parameter in vivo sensing platform for intrauterine studies and subfertility diagnostics.* PhD thesis, University of Southampton, 2018.

[155] J. M. Stine, L. A. Beardslee, R. M. Sathyam, W. E. Bentley, and R. Ghodssi, "Electrochemical dissolved oxygen sensor-integrated platform for wireless in situ bioprocess monitoring," *Sensors and Actuators, B: Chemical*, vol. 320, 10 2020.

[156] C. Amatore, A. Oleinick, and I. Svir, "Simulation of diffusion at microring electrodes through conformal mapping," *Journal of Electroanalytical Chemistry*, vol. 564, pp. 245–260, 3 2004.

[157] C. G. Zoski, "Ultramicroelectrodes: Design, fabrication, and characterization," *Electroanalysis*, vol. 14, pp. 1041–1051, 8 2002.

[158] A. Sardarinejad, D. K. Maurya, M. Khaled, and K. Alameh, "Temperature effects on the performance of ruo2 thin-film ph sensor," *Sensors and Actuators, A: Physical*, vol. 233, pp. 414–421, 2015.

[159] YOKOGAWA, "ph/orp buffer calibration solutions." https://www.yokogawa.com/uk/solutions/products-and-services/measurement/analyzers/liquid-analyzers/ph-sensors/ph-orp-calibration-solutions/#Downloads__MSDS-SDS, 2022. Accessed: 2022-04-01.

[160] F. Mathieu, J. P. Jouany, J. Sénaud, J. Bohatier, G. Bertin, and M. Mercier, "The effect of saccharomyces cerevisiae and aspergillus oryzae on fermentations in the rumen of faunated and defaunated sheep; protozoal and probiotic interactions," *Reproduction Nutrition Development*, vol. 36, pp. 271–287, 1996.

[161] J. P. Marden, C. Julien, V. Monteils, E. Auclair, R. Moncoulon, and C. Bayourthe, "How does live yeast differ from sodium bicarbonate to stabilize ruminal ph in high-yielding dairy cows?," *Journal of Dairy Science*, vol. 91, pp. 3528–3535, 2008.

[162] N. Yarlett, R. I. Scott, A. G. Williams, and D. Lloyd, "A note on the effects of oxygen on hydrogen production by the rumen protozoon dasytricha ruminantium schuberg," *Journal of Applied Bacteriology*, vol. 55, pp. 359–361, 1983.

[163] M. J. Eckl, Y. Mattausch, C. K. Jung, S. Kirsch, L. Schmidt, G. Huebner, J. E. Mueller, L. A. Kibler, and T. Jacob, "The influence of platinum surface oxidation on the performance of a polymer electrolyte membrane fuel cell—probing changes of catalytically active surface sites on a polycrystalline platinum electrode for the oxygen reduction reaction," *Electrochemical Science Advances*, vol. 2, pp. 1–13, 2022.